

An Attempt to Quantify Errors in the Experimental Modal Analysis Process

by

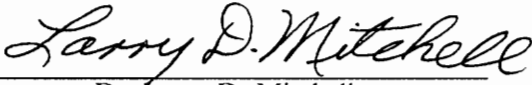
Kannan Marudachalam

Thesis submitted to the Faculty of the
Virginia Polytechnic Institute and State University
in partial fulfillment of the requirements for the degree of
Master of Science
in
Mechanical Engineering

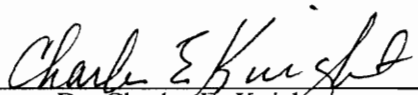
APPROVED:



Dr. Alfred L. Wicks, Chairman



Dr. Larry D. Mitchell



Dr. Charles E. Knight

September, 1992
Blacksburg, Virginia

C.2

LU
5655
V855
1992
M3728
C.2

An Attempt to Quantify Errors in the Experimental Modal Analysis Process

by

Kannan Marudachalam

Dr. Alfred L. Wicks, Chairman

Mechanical Engineering

(ABSTRACT)

Experimental modal analysis (EMA) techniques have become a popular method of studying the dynamic characteristics of structures. A survey of literature available reveals that experimental modal models resulting from EMA may suffer from inaccuracy due to a host of reasons. Every stage of EMA could be a potential source of errors - from suspension of the test structures, transduction to parameter estimation phase. Though time-domain methods are actively being investigated by many researchers and are in use, fast Fourier transform (FFT) methods, due to their speed and ease of implementation, are the most widely used in experimental modal analysis work.

This work attempts to quantify errors that result from a typical modal test. Using a simple beam with free-free boundary conditions simulated, three different modal tests are performed. Each test differs from the other chiefly in the excitation method and FRF estimator used. Using finite element models as the reference, correlation between finite element and experimental models are performed. The ability of the EMA process to accurately estimate the modal parameters is established on the basis of level of correlation obtained for natural frequencies and mode shapes. Linear regression models are used to correlate test and analysis natural frequencies. The modal assurance criterion (MAC) is used to establish the accuracy of mode vectors from the modal tests. The errors are further quantified spatially (on a location-by-location basis) for natural frequencies and mode shapes resulting from the EMA process. Finally, conclusions are made regarding the accuracy of modal parameters obtained via FFT-based EMA techniques.

Acknowledgements

This work has been an unduly long-drawn affair. It was a rude awakening for me, if I may say so, in coming to face the realities of solving engineering problems. Finally I have learnt, I hope, to draw the line between science and engineering.

During this entire period, the forbearance and encouragement shown by my advisor, Dr. Wicks, is acknowledged here with great appreciation. I thank him gratefully for all his advice, guidance and support in this research. He has been more than an advisor, helping me promptly at times of need, with a warm and cheerful smile.

I take this opportunity to thank professors Dr. Knight and Dr. Mitchell, for serving on my thesis committee. Dr. Mitchell's effort in conscientiously proof-reading and commenting on my thesis was most useful, and is recorded here with much thankfulness. Dr. Knight's suggestions and comments on certain Chapters of this thesis were valuable.

Finally, I would like to thank Dr. Man-Cheol Han for all that help with his curve-fitting routine.

Table of Contents

Introduction	1
1.1 Problem Statement	2
1.2 Brief Description of Tasks	5
1.3 Organization of Thesis	8
1.4 Summary of Results and Conclusions	11
Literature Review	16
2.1 Errors in the Experimental Modal Analysis Process	17
Analytical Techniques	30
3.1 Bending of Straight Beams	31
3.1.1 The Euler-Bernoulli Beam Theory	32
3.1.2 The Timoshenko Beam Theory	38
3.1.3 Working Forms of the Equations of Motion of a Beam	40
3.1.3.a Small motions with axial forces	41
3.1.3.b Small motions without axial forces	42
3.1.4 Euler-Bernoulli (vs) Timoshenko beam theory	42

3.2 The Free Vibration Problem	46
3.2.1 The Eigenvalue Problem	47
3.2.2 Natural Frequencies and Mode Shapes	48
3.2.4 Analytical Modeling of the Test Structure	53
3.3 Techniques for Correlation of Experimental and Analytical Structural Dynamic Models	57
3.3.1 Correlation of Modal Models	58
3.3.1.a Natural Frequencies	58
3.3.1.b Mode Shapes	59
3.3.2 Methods for Correlating Mode Shapes	60
3.3.2.a Visual Inspection	60
3.3.2.b Orthogonality Check Method	60
3.3.2.c Modal Assurance Criterion (MAC)	61
The Finite Element Model	64
4.1 The Finite Element Equations	66
4.1.1 The Governing Equations of Motion	66
4.1.2 Formulation of the Euler-Bernoulli Beam Element	67
4.1.3 Formulation of the Timoshenko Beam Element	74
4.2 Computer Implementation	80
4.2.1 The Free Vibration Problem	80
4.2.2 Solution Methodology Used in This Work	81
4.3 Modeling	83
4.3.1 Inertias of Transducers	84
4.3.2 Body Force Due to Gravity Load	85
4.3.3 Sample Results and Discussion	87
The Experimental Model	96
5.1 Theoretical Concepts in Modal Analysis	97

5.1.1 Single-Degree-of-Freedom Systems	97
5.1.2 Multiple-Degree-of-Freedom Systems	100
5.1.2.a Undamped multiple-degree-of-freedom systems	100
5.1.2.b Damped multiple-degree-of-freedom systems	104
5.1.3 Alternative Approaches to Derive the FRF	108
5.1.3.a FRF from arbitrary excitation	108
5.1.3.a FRF from random excitation	109
5.2 The Sources and Nature of Errors in the EMA Process	112
5.2.1 Transduction Methods and Test Configurations	113
5.2.2 Signal Processing of Excitation and Response Measurements	113
5.2.2.a Implications of leakage and windowing on the quality of modal model	115
5.2.3 FRF Estimation	116
5.2.3.a A General Input/Output Model of a Linear System	116
5.2.4 Modal Parameter Estimation	122
5.2.4.a Single-degree-of-freedom analysis methods	124
5.2.4.b Multiple-degree-of-freedom analysis methods	125
5.3 Modal Tests Performed and Procedures Used	127
5.3.1 TEST 1	128
5.3.2 TEST 2	129
5.3.3 TEST 3	130
5.3.4 Modal Parameter Estimation Procedures	131
Results and Discussion	140
6.1 Results from Finite Element Analyses	141
6.1.1 Finite Element Models and Results - TEST 1	145
6.1.2 Finite Element Models and Results - TEST 2	150
6.1.3 Finite Element Models and Results - TEST 3	152
6.2 Results from Experimental Modal Analyses	153

6.2.1 Results from TEST 1	153
6.2.2 Results from TEST 2	155
6.2.3 Results from TEST 3	156
6.3 Comparison and Discussion of Results	157
6.3.1 Correlation Between Test and Analysis Models - TEST 1	157
6.3.2 Correlation Between Test and Analysis Models - TEST 2	167
6.3.3 Correlation Between Test and Analysis Models - TEST 3	173
6.4.4 Investigation/Reconciliation of Poor Correlation Observed for the First Mode	179
6.5 Summary of Results	182
Conclusions	187
References	189
Appendix A. Nomenclature	193
Vita	197

List of Illustrations

Figure 3.1. Kinematics of deformation in the (a) Euler-Bernoulli beam theory (b) Timoshenko beam theory	33
Figure 3.2. (a) Beam in loaded configuration (b) Forces and moments acting on an elemental length of the beam	37
Figure 3.3. Influence of (a) Rotatory inertia (b) Shear deformation on the natural frequencies of a simply supported beam	44
Figure 3.4. Combined effects of rotatory inertia and shear deformation on the natural frequencies of a simply supported beam	45
Figure 3.5. First four natural modes of a free-free bar in bending vibration	51
Figure 3.6. Test configuration and the corresponding physical model	54
Figure 3.7. A two-degree-of-freedom model for estimating the rigid-body modes of the test structure	56
Figure 4.1. Degrees of freedom in (a) Euler-Bernoulli beam element (b) Timoshenko beam element	69
Figure 4.2. A typical element in the mesh shown in local coordinates for (a) Euler-Bernoulli beam element (b) Timoshenko beam element	71
Figure 4.3. Test configuration and two mathematical models	92
Figure 4.4. Influence of gravity force on the first mode of a vertically suspended beam	94
Figure 4.5. Influence of gravity force on the second mode of a vertically suspended beam	95
Figure 5.1. A general input/output model of a linear system	118
Figure 5.2. Test configuration used in TEST 1	134
Figure 5.3. Test configuration used in TEST 2	136
Figure 5.4. Test configuration used in TEST 3	138
Figure 6.1. Figure illustrating the simulation of moving the accelerometer mass in the FE model	146

Figure 6.2. Tenth mode of BEAM 1 (TEST 1) showing the effect of inertia-loading by the roving accelerometer and fixed force transducer	149
Figure 6.3. Eighth mode of BEAM 2 (TEST 2) showing the effect of inertia-loading by the fixed accelerometer	151
Figure 6.4. TEST 1 - Correlation between FEA and EMA natural frequencies from translational data	163
Figure 6.5. TEST 1 - Correlation, between FEA and EMA, of variation in natural frequencies due to changing accelerometer locations	164
Figure 6.6. TEST 1 - Modal assurance criterion (MAC) between FEA and EMA mode vectors for translational data	165
Figure 6.7. TEST 1 - Modal assurance criterion (MAC) between FEA and EMA mode vectors for rotational data	166
Figure 6.8. TEST 2 - Correlation between FEA and EMA natural frequencies from translational data	170
Figure 6.9. TEST 2 - Modal assurance criterion (MAC) between FEA and EMA mode vectors for translational data	171
Figure 6.10. TEST 2 - Modal assurance criterion (MAC) between FEA and EMA mode vectors for translational data, shown for modes 2 through 8	172
Figure 6.11. TEST 3 - Modal assurance criterion (MAC), between EMA and FEA mode vectors for (a) Model 1 and (b) Model 2	175
Figure 6.12. TEST 3 - Comparison of mode shape data from FEA and EMA for the first mode (Model 1 - shaker located at the top)	176
Figure 6.13. TEST 3 - Comparison of mode shape data from FEA and EMA for the first mode (Model 2 - shaker located at the bottom)	177
Figure 6.14. TEST 3 - Driving-point FRF (accelerance) from (a) Model 1, and (b) Model 2	178
Figure 6.15. TEST 2 - Comparison of mode shape data from FEA and EMA for the first mode	183

List of Tables

Table 3.1. Material and geometric property values of the beam used in sample results 52

Table 3.2. Natural frequencies of the first 10 flexible modes for a beam with free-free boundary conditions using Euler-Bernoulli theory 52

Table 4.1. Material and geometric property data for the beam used in sample analyses 89

Table 4.2. Convergence characteristics of the Euler-Bernoulli beam element 90

Table 4.3. Convergence characteristics of the Timoshenko beam element 91

Table 4.4. Influence of a constant compressive load on the natural frequencies of a simply supported beam 93

Table 4.5. Influence of gravity force on the natural frequencies of the first ten flexible modes of a vertically suspended beam 93

Table 5.1. Tabulation of test parameters used in TEST 1 135

Table 5.2. Tabulation of test parameters used in TEST 2 137

Table 5.3. Tabulation of test parameters used in TEST 3 139

Table 6.1. Material and geometric property values used in FE analyses 143

Table 6.2. FEA natural frequencies, of the first 10 flexible modes, for the two beams used in the modal tests 144

Table 6.3. Natural frequencies from FEA with inertia-loading effect from TEST 1 simulated (shown for modes 1 through 5 for all the 23 response locations) 147

Table 6.4. Natural frequencies from FEA with inertia-loading effect from TEST 1 simulated (shown for modes 6 through 10 for all the 23 response locations) 148

Table 6.5. Natural frequencies from FEA for various modeling conditions from TEST 2 . . . 150

Table 6.6. Natural frequencies from FEA for various modeling conditions from TEST 3 (Model 1) 152

Table 6.7. Comparison of FEA and EMA natural frequencies from TEST 1, along with damping ratio estimates from EMA 154

Table 6.8. Comparison of FEA and EMA natural frequencies from TEST 2, along with damping ratio estimates from EMA	155
Table 6.9. Comparison of natural frequencies and damping ratios obtained from EMA for Model 1 and Model 2	156
Table 6.10. Results for the first mode from TEST 1,TEST 2 and TEST 3	182

Chapter 1

Introduction

Historically, the experimental modal analysis technique is a fairly recent development. The past two decades have seen a rapid growth in the area of experimental modal analysis. Though the late 50's and the early 60's used the concept of resonance testing, it was not until 1965 when Cooley and Tukey [1]¹ came up with the fast Fourier transform (FFT)² that the experimental modal analysis became an attractive tool. In a similar fashion the finite element method also had its birth in the 60's [2-4]. But, it was not until the mid 70's that the finite element technique became an attractive tool for dynamic analysis, though it was already a very popular analysis method for solving static problems. This was mainly due to the non-availability of suitable solution algorithms and the required computing power. But when both became available, the finite element technique, due to its versatility, soon became a very powerful and indispensable analysis tool. Since then the technique has been exploited extensively making even nonlinear analysis possible, both static and dynamic. The enormous growth in computing power along with advancements made in computer graphics and related technology, have been instrumental to the growth of finite element technology.

¹ Numbers in brackets denote references at the end of this thesis

² the abbreviated form FFT will be used to denote fast Fourier transform

Analytical dynamic modeling of structures is invariably carried out by the finite element technique. There are many advantages in building an analytical model as opposed to an experimental model. Some of the important ones are that an analytical model can be made at the design stage and modifications can be made and evaluated very easily. Also, several optimization schemes can be carried out with very little cost. However, there are inherent uncertainties in building an analytical model. Approximation of distributed physical properties, boundary conditions, inaccurate material property values, damping representation, modeling of joints, etc. are some of the more obvious problems. This makes experimental validation useful. Since the finite element method discretizes a structure's stiffness, mass and sometimes damping, experimental techniques which provide information on the above physical parameters of the structure would be the most useful. Unfortunately, experimental determination of physical properties is equally fraught with uncertainty and difficulties found in analytical modeling. Consequently, the experimental approach in which the modal parameters, viz., natural frequencies, mode shapes and damping ratios, are estimated, has gained prominence. Since these modal parameters describe the dynamics of a linear system completely, and since they can be estimated with sufficient accuracy, they can be used to obtain an experimental dynamic model. Also, the analytical model can be solved mathematically to yield these modal parameters. Since the modal parameters are directly related to the physical properties of a structure, comparison and correlation of modal parameters from analytical and experimental models has been the most popular method of validating one with reference to the other.

1.1 Problem Statement

Experimental modal analysis (EMA)³ has become a very valuable tool in studying a structure's dynamic characteristics. Its popularity could be attributed, in part, to its complementary nature to

³ The abbreviation EMA will be used most of the time instead of experimental modal analysis

other analytical tools available today to study the dynamic behavior of structures. Also, the technique deals with the structure directly, unlike the abstract world of analytical modeling. Therefore, experimental modal analysis, like most other experimental techniques, is capable of predicting the true behavior of a structure.

In recent years a major effort has been made to correlate and combine analytical techniques to experimental methods in the area of structural modeling. Almost invariably, the finite element method is used in analytical modeling of structures. Due to the reliability of its results, experimental modal models are used to update finite element models. Extensive work has been done to identify errors and inadequacies in the finite element model that yield inaccurate results. An assumption associated with finite element model updating from experimental models is that the experimental is the reference to which the analytical model is to be matched. This assumption is corrupted by a number of factors identified by several authors [5,6]. Due to the diverse and inexact nature of some of the processes involved, the final experimental model may deviate from accuracy. Every stage of the experimental modal analysis process is a potential source of errors that finally contribute to an inaccurate model. Some of the more obvious and critical problems are stated below,

- The transduction methods are capable of introducing undetectable errors. Typical problems with force transducers are their sensitivity to bending and shear loads and measurement errors they introduce at resonances. Similarly, transverse sensitivity of accelerometers is a critical problem. Both force and response transduction result in inertia-loading (mass-loading)⁴ of the structure, the effect of which has several ramifications. Further, the transducers may vary in response as a function of frequency.
- Several techniques are used to support and excite test structures. These may alter the implied boundary conditions and hence the dynamic properties of the structure. Also, there is a stag-

⁴ Since both translational and rotational inertias of transducers contribute to this effect, the term inertia-loading is preferred to mass-loading

gering variety of excitation techniques available, each with specific advantages and limitations. Thus, the use of an inappropriate excitation method can result in an inaccurate model.

- Several signal processing techniques employed are inexact in nature, and have the effect of altering the data if used improperly. Principally, leakage of frequency-domain data introduces bias errors which are very hard to quantify.
- The accurate estimation of frequency response functions (FRFs)⁵ is central and crucial to realizing accurate experimental dynamic models, since it forms the basis of experimental modal analysis. In spite of tremendous research activity which this area has attracted, practical and efficient methods for unbiased estimation of FRFs are yet to be realized. Problems of measurement noise, frequency resolution, leakage and nonlinearities are the key contributors to inaccurate FRF estimation.
- The estimation of modal parameters by curve-fitting the experimentally acquired FRFs is the goal of the modal parameter extraction process. A wide variety of methods are used, both in the time- and frequency-domain. Some use a single-degree-of-freedom (SDOF) assumption while others use a multiple-degree-of-freedom (MDOF) assumption. The problem is essentially nonlinear, though several linearized methods are in use. While nonlinear methods yield unbiased results with minimum variance, linearized methods yield estimates which have variance and bias errors. Several factors affect the accuracy of these modal parameter estimation algorithms. Typically, these are high damping, high modal densities, closely spaced modes, measurement noise and insufficient frequency resolution. Usually, a higher model order is used for accurate estimation of the modal parameters. This results in the creation of extraneous (computational) modes which could cause serious problems if the system has closely spaced modes. To date, there is no quantitative method to evaluate the accuracy of the curve-fit.

⁵ The terms frequency response function will be denoted by FRF, and FRFs when plural

The combination of these errors detract from the confidence and reliability of the experimental modal analysis results. Often, this lack of confidence has precluded attempts to perform detailed updating of the analytical model. Observing the nature and subtleties of the various processes involved, it is apparent that quantifying errors in them is a rather difficult task. Nevertheless, it is necessary if accurate models are to be realized. Even otherwise, the practitioner has to "understand" the degree of accuracy his or her model possesses.

This research effort has been aimed at determining the accuracy of the experimental model from a quantitative perspective. A simple structure, a free-free beam, is chosen as the structure (system) to be modeled, so that all the above errors which are typically found in an analytical model are reduced to a minimum. Thus, using the analytical model as the reference, attempts are made to study the errors arising from deriving an experimental model. The sources of error typically associated with experimentation, i.e., calibration and linearity of the transduction method, are not the focus of this work. Correlation of natural frequencies and mode shapes to an analytical model are performed, to identify the contribution of the measurement and modal parameter estimation process to the inaccuracy of the final modal model.

1.2 Brief Description of Tasks

The errors typically found in an EMA process are those due to transduction, signal processing, frequency response function (FRF) estimation and modal parameter estimation. The quality of the modal model obtained directly depends on the accuracy of the above processes. To study how these impact the quality of the modal model, several modal tests are designed. A beam, with simulated free-free boundary conditions, is used as the structure whose modal parameters are to be estimated. A finite element model of the beam is used to provide results which are to be used as the

reference. All the errors which are typically associated with a finite element model are kept to a minimum by using a simple structure such as this beam with free-free boundary conditions.

Modal Tests

Two different uniform steel beams are used as test structures to be modeled. All the tests are performed using base-band analysis. All the tests use a test configuration in which the beam is suspended vertically. The first test (TEST 1)⁶ is performed using an electrodynamic shaker as the excitation source, using burst random excitation. Response measurements are made using an accelerometer capable of making simultaneous translational and rotational measurements. Twenty three translational and rotational measurements are acquired using the H^{e7} FRF estimator [7,8], in the frequency range 0-1000 Hz. The second test (TEST 2), performed in the range 0-500 Hz, uses the impulse excitation technique. Unlike the first test, the excitation location is varied along the beam while the response location is fixed. A total of 61 FRFs are acquired using the H_1 [9] estimator. The third test (TEST 3) is designed to investigate the influence of exciter location on the resulting modal parameters. The test is repeated twice, once with shaker located at the top and then with the shaker located at the bottom of the beam. Twenty one FRFs are obtained using the H_1 [9] estimator. A global frequency-domain parameter estimation algorithm, using Forsythe orthogonal polynomials [10], is used to extract the modal parameters. The curve-fitting is performed on individual FRFs in all the tests. In case of global parameters (natural frequencies and damping ratios) the mean of all the individual estimates is used along with a statement of variance. The details of signal processing, FRF estimation, modal parameter extraction, etc. are elaborated in Chapter 5.

Analytical Modeling

Two popular beam theories, the Euler-Bernoulli and the Timoshenko beam theory, are used in the analytical modeling of the beam. The equations of motion of beams using these two beam theories

⁶ Subsequently, the three modal tests will be identified as TEST 1, TEST 2 and TEST 3

⁷ Refer to Appendix A for the nomenclature used in this thesis

are presented in detail in Chapter 3. The influence of shear deformation and rotatory inertia on the natural frequencies of a simply supported beam are shown with the aid of plots available in the literature. The free vibration problem of a uniform beam according the Euler-Bernoulli theory is stated. Also, the frequency and mode shape equations for a beam with free-free boundary conditions are stated. This is followed by a short discussion of several aspects regarding the analytical modeling of the test structure. Equations of rigid-body motion of a beam suspended vertically, by means of a string, is derived using a two-degree-of-freedom model. The model is then used to calculate the rigid-body modes of the test structure

The choice of finite element method for analytical modeling of the test structure is justified. The finite element equations based on the Euler-Bernoulli and the Timoshenko beam theories are developed using the Ritz variational approach. The finite element matrices that result from the above formulation are stated for both the beam elements. The finite element technique, using these two element types, is implemented through a FORTRAN code. The modeling techniques used to simulate inertia-loading by transducers, gravity force and boundary conditions that exist in the actual testing environment are discussed. The solutions from finite element models are validated by comparing them with exact solutions, if they are available. This is done by comparison of natural frequencies obtained by both methods.

Correlations of Experimental and Analytical Models

The experimental modal model comprises of natural frequencies, damping ratios and translational mode vectors (rotational mode vectors are included in TEST 1). Though the parameter estimation method used accounts for complex modes, if they exist, normal mode assumptions are used for the test structure. Thus, only the imaginary part of the residue is used in establishing the mode vectors. The finite element models, on the other hand, comprise of only the natural frequencies and mode vectors. Correlation between experimental and analytical natural frequencies are made using linear regression models along with tabulations. The mode vectors are correlated using the Modal Assurance Criterion (MAC) [11]. The accuracy and hence the levels of errors in the EMA process are determined by the degree of correlation obtained with the results from FE model. Subse-

quently, the errors in the experimental modal model (natural frequencies and mode shapes) from TEST 1 and TEST 2 are quantified.

1.3 Organization of Thesis

The current Chapter ends with a summary of results from this work. Chapter 2 reviews pertinent work in the literature that identifies errors in the EMA process. Errors associated with transduction, test structure support, signal processing, FRF estimation and modal parameter estimation are reviewed via literature that exists.

Chapter 3 is devoted to the analytical development of the equations of motion of beams. The governing equations of motion of a beam using the Euler-Bernoulli and Timoshenko theories are presented. The assumptions and limitations of the above theories are stated. Also, frequency and mode shape equations from the Euler-Bernoulli beam theory are presented. The Euler-Bernoulli and the Timoshenko theories are compared on the basis of significance of shear deformation and rotatory inertia effects. The influence of these effects on the natural frequencies of a uniform beam with simply supported boundary conditions are illustrated. Further, several aspects of analytical modeling of the test structure are discussed. Finally, a section which exclusively discusses correlation methods, used for correlating experimental and analytical results, is included.

Derivation of the finite element equations of motion, modeling techniques used and validation of finite element models through sample results form the contents of Chapter 4. First, choosing the finite element method for analytical modeling of the test structure is justified. The finite element equations of motion, based on the Euler-Bernoulli and Timoshenko beam theory, are derived using the Ritz variational approach. The element matrices that result from the above variational ap-

proach are stated for both the beam elements. The details of computer implementation of the method are given. The modeling procedures used to construct the analytical model of the test structure, to simulate experimental test conditions, are discussed. These include inertia-loading by transducers and gravity force acting on the vertically suspended beam with the associated boundary conditions. Also, two different approaches to model the gravity force are discussed. Finally, the solutions from finite element models are validated by comparing them with the corresponding exact solutions. Such comparison and validation are restricted to Euler-Bernoulli beam elements, since exact solutions are available. Furthermore, only natural frequencies are used for comparison and validation purposes.

Chapter 5 is concerned with the experimental modal analysis technique and the modal tests performed. Some theoretical concepts that form the basis of experimental modal analysis will be outlined. These include the assumptions and simplifications that are used in arriving at theoretical models (equations) for the FRF. Alternative methods for deriving the FRF, methods in which transient and random excitations are used, are stated. The sources and nature of errors that arise in the EMA process are mentioned. This includes a detail discussion of the errors that may be encountered during transduction, signal processing, FRF estimation and modal parameter extraction. Next, a detail description of the experimental set-up used and the specifics of each modal test performed are presented. The procedures used and their details - transduction (excitation and response measurements), signal processing, FRF estimation and modal parameter estimation, are presented. This is done for each test performed (TEST 1, TEST 2 and TEST 3). This is done by using a chart which provides easy and efficient access to details and information about each test.

Chapter 6 begins with the presentation of results from finite element analyses of analytical models that correspond to TEST 1, TEST 2 and TEST 3. The analytical (FE) model that corresponds to each test and its modeling details are given. The results for natural frequencies from each of these models are presented. Next, results for natural frequencies and damping ratios from each modal test are tabulated, along with the corresponding FEA natural frequencies. This is followed by a Section in which the results from EMA and FEA are compared and discussed. This is done on a

test-by-test basis, starting from TEST 1. First, the natural frequencies are compared, visually, and discussed. Then, a correlation study between experimental and analytical natural frequencies is done by using linear regression models. This is followed by a Section in which errors in estimating natural frequencies by EMA are quantified. Next, the mode shapes from EMA are correlated with those obtained from the corresponding FE models using the modal assurance criterion (MAC). The quality of the mode vectors from EMA are assessed based on the degree of correlation, established through MAC, observed. Errors in estimating the modal displacements by EMA are then quantified by using mode vectors from FEA as the reference. A discussion of results from EMA in which poor correlation is observed is included in the final Sections of the Chapter. The Chapter concludes with a summary of results from the study.

A note on conventions that will be followed

Through-out this thesis the SI units will be used. Without exception, only the cyclic frequency, expressed in Hertz (Hz), will be used to express frequencies. Several phrases, e.g., experimental modal analysis (EMA), finite element analysis (FEA), occur too often and too many times in this thesis. It is preferred, therefore, to make use of their abbreviated form whenever necessary. Any convention, when used for the first time, will be explained in a footnote. Symbols, both Latin and Greek, used are defined at the end of this thesis, in Appendix A. However, certain symbols are used on an *ad hoc* basis in certain portions of this thesis. Under such circumstances, the symbols will be defined locally within the text. References will be cited using brackets, and will be numbered sequentially in the order that they are made. Equation numbers will be denoted in parenthesis. Several references that may not have a direct bearing on this thesis will be referenced through footnotes.

1.4 Summary of Results and Conclusions

The goal of this thesis was to identify and quantify errors in modal models derived experimentally using FFT-based procedures. The interest was on errors incurred in estimating natural frequencies and mode shapes. Specifically, the contribution of the transduction (measurement) and modal identification process to the inaccuracy of the final modal model was the focus of the effort. A simple uniform steel beam was used as the test structure whose modal properties were to be determined. Three modal tests, each differing principally in the excitation method and FRF estimator used, were designed and performed on the beam. The experimentally derived modal models were compared with corresponding analytical models that were used as the reference, and therefore assumed to be accurate. The finite element method was used in analytical modeling of the test structure.

The quality of the experimentally derived modal models were assessed based on the degree of correlation realized with the corresponding analytical models. Linear regression models were used for correlating experimental and analytical natural frequencies. Since the FRFs were curve-fitted individually, statistical variation of the estimates of global parameters was available in each case. This enabled a quantitative assessment of the degree of variability in estimating global parameters. The errors in estimating natural frequencies were also quantified spatially, i.e., for each spatial location/measurement. The errors in identifying mode shapes were quantified, with reference to analytical mode vectors, using the modal assurance criterion (MAC). As was done with natural frequencies, the errors in experimental mode vectors were quantified, with reference to analytical mode vectors, spatially.

TEST 1

The test was done in a base-band of 0-1000 Hz. Both translational and rotational response measurements were made at 23 locations along the length of the beam. Burst random excitation,

with an exponential window on both excitation and response measurements, was used. The H^c estimator with 20 ensemble averages was used for FRF estimation. A total of 10 beam bending modes were identified. Based on the results obtained, the following conclusions are made:

- From linear regression analysis, the natural frequencies from EMA show a high degree of correlation with those obtained from FEA. However, there are slight differences between analytical and experimental values, owing to the fact that accurate material property values were not known. The accuracy of the variation (shifts) of natural frequencies from EMA, due to inertia-loading, were strongly influenced by the frequency resolution (in the FRF) used in the FFT process. This was corroborated by the correlations observed for variation of natural frequencies due to inertia-loading effect. The inertia-loading affect also accounts for the high variances observed in estimating the natural frequencies. The errors in estimating natural frequencies, from individual FRF measurements, were significant only at locations near nodal points of modes. This was due to poor signal-to-noise ratios at these locations, the errors being generally less than 2%.
- The quality of the mode vectors from translational measurement are excellent. This is suggested by the high MAC values (in excess of 0.99) obtained for translational mode vectors. Also the EMA process was found to be sensitive enough to measure changes in modal displacement due to inertia-loading effect. This was shown consistently for all the 10 modes. The rotational mode vectors were poor compared to translational mode vectors due to very poor signal-to-noise ratios, as was suggested by poor values of coherence function estimates. The errors in estimating modal displacements were generally less than 5%, except near nodal points of modes.

The frequency resolution used for FFT computation and poor signal-to-noise ratios seem to be the singular factor that has affected the accuracy of modal parameter estimates from individual measurements. The contribution of the transduction process (inertia-loading) comes second in importance, though these are not as significant. The modal parameter estimation phase does not seem

to have injected errors that could be recognized as significant, except near nodes, where estimates of all three parameters were oftentimes poor. Finally, the choice of test configuration has not influenced the modal model significantly.

TEST 2

This test was performed in a base-band of 0-500 Hz. Fixed accelerometer location and use of impact excitation were the main features of this test. Force window for excitation measurements and an exponential window for response measurements was used. The H_1 estimator with 10 ensemble averages was used for FRF estimation. A total of 61 FRFs were acquired from translational measurements. The following observations were made from the correlations made with analytical models:

- Using linear regression models a high degree of correlation was observed between test and analysis natural frequencies. Also, the variability in estimating the natural frequencies were much smaller than those observed in TEST 1, where the inertia-loading effect shifted natural frequencies. This proved conclusively that the high variances in estimating natural frequencies in TEST 1 were neither due to measurement nor parameter estimation processes, but due to inertia-loading. The variances observed from TEST 2 results show the combined (total) errors in estimating natural frequencies that are inherent to the EMA processes. Also, with respect to the frequency resolution used, the variability observed for natural frequency estimates is not significant. The errors in estimating natural frequencies, from individual FRF measurements, were significant only at location near nodal points of modes.
- Estimates of mode shapes were considered to be excellent, except for the first mode, on the basis of the MAC values obtained. Modes 2 through 8 have MAC values above 0.99. Also, the MAC values consistently increased for all the modes when the accelerometer inertias were included in the FE model. This showed the sensitivity of the EMA process to detect small deviations, such as the one introduced by the accelerometer inertia. The quality of the first mode, presumably, was affected by several factors discussed in Chapter 6. The errors in esti-

mating modal displacements were all within 5%, except for the first mode, which showed a systematic deviation. Also, as was seen for TEST 1, the estimates near nodal points were generally poor.

TEST 3

This test was performed in the frequency range 0-125 Hz. The main purpose was to assess the influence of shaker location on the resulting modal model. The H_1 estimator with 10 ensemble averages was used for FRF estimation, and the accelerometer used had very little mass. This was to minimize the effect of inertia-loading. The test was performed twice, once with the shaker located at the top (**Model 1**) and then with the shaker located at the bottom of the beam (**Model 2**). For each model 21 response locations were used for acquiring translational measurements. Three bending modes were identified in the frequency range. The results are summarized below:

- The natural frequencies from both models differed slightly, but the differences were insignificant.
- The mode vectors from **Model 1** had reasonably good correlation, comparable to the one from TEST 2. However, mode vectors from **Model 2** had poor correlation, compared to mode vectors from **Model 1**. The first mode in particular had very low MAC value (0.93). This was reconciled as being due to the identification (by the parameter estimation algorithm) of a spurious mode in the range 0-10 Hz, which contaminated the estimates of the first mode.

In general, results from TEST 3 were poorer, compared to TEST 1 and TEST 2 results. For **Model 2**, though the frequency resolution used was high, and only three modes were involved, the quality of the experimental model was far from good. A discussion of probable reasons for this was presented in Chapter 6. The modal model realized through **Model 2** showed the importance of proper test structure suspension and exciter location.

CONCLUSIONS

Based on the results obtained from TEST 1, TEST 2 and TEST 3, the following conclusions were drawn,

- The contribution of the transduction processes to the inaccuracy was very small. *Quality* transducers and *careful* measurements can hold this error to negligible levels.
- The errors due to the parameter estimation process were significant only at locations near nodal points of modes.
- Both natural frequency and residue estimates were very poor at locations close to nodal points of modes. All the four modal parameters were in substantial error at these locations. The natural frequency estimates were the poorest of all modal parameters, the error being around 2 to 3%.
- Poor signal-to-noise ratios and insufficient frequency resolution were the singular limiting factors, apparently, to the accuracy of modal parameter estimates from individual FRF measurements.
- The choice of test structure support has to be carefully made. An erroneous choice may imply wrong boundary conditions that may alter the model substantially.
- Finally, in conclusion, a carefully planned and performed modal test that takes into account all the sources of error can yield very accurate models.

Chapter 2

Literature Review

The material presented in this chapter covers pertinent literature that has the scope of identifying errors in the EMA process. For the most part it reviews literature that identifies errors and shortcomings of the experimental modal analysis process. Fast Fourier transform methods, due to their speed and versatility, have become very popular in EMA work. Though time-domain techniques, methods which use input and output time-domain data as well as those using the impulse response function, are being investigated by researchers, a vast majority of modal testing is done using FFT-based methods. Therefore, the scope of this thesis, and hence this literature review, is restricted to FFT-based techniques.

A typical modal test and analysis begins by making force and response measurements at a number of locations on the structure. These force and response signals are processed suitably (signal processing) and an FFT is performed to transform the time-domain signals to frequency-domain data. Then, using an appropriate estimator the FRF is estimated. This is followed by curve-fitting the FRF data using an appropriate modal parameter estimation algorithm. Thus, the modal parameters, viz., natural frequencies, mode shapes and damping ratios present in the frequency band tested are estimated. These modal parameters are then compared to those obtained from an analytical

model, typically a finite element model. As identified in the introductory Chapter, there are several aspects of FFT-based methods which, in practice, result in less-than-expected accuracy. As mentioned earlier, every stage of the process is a potential source of errors, which has a cascading effect on the accuracy of the final modal model. The following Sections review pertinent literature which identifies errors in the EMA process.

2.1 Errors in the Experimental Modal Analysis Process

The quality of the experimental model depends directly on every stage of the modal test and analysis. The State-of-the-Art of Mobility Measurements (SAMM) results presented by Ewins and Griffin [5] show the level of accuracy and consistency that could be expected from a modal test. They point out, logically, that the variability is due to systematic errors [5]. They point out [5] the sources of these systematic errors to such factors as secondary excitations generated by poor shaker attachments, uncorrected effects of transducer inertias, poor signal conditioning, amplitude-dependent nonlinearity, etc., not to mention modal parameter estimation. Some pertinent literature falling within the scope of this thesis will be briefly reviewed here.

Experimental models are only as good as the measurements made. Therefore, the quality of the transduction process is very vital to obtaining an accurate experimental model. Transducer testing, calibration and subsequent validation of transducers used is a very important step of every modal test. A very detailed discussion of "internal validation" techniques of experimental data is presented by Stein [12]. Various techniques that could be used to ensure acquiring of valid data, problems related to dynamic properties of measuring systems, environmental factors that influence the response of measuring systems are all identified and discussed in detail. In addition, the problems of measuring system/process interaction are stated (e.g., inertia-loading). Hopton and Deblauwe [13] show how transducer inertia-loading can result in mode vectors which are complex, even for a

proportionally damped system. They state [13] that the problem is essentially due to frequency shifts, which makes the problem of estimating the number of poles in a frequency range difficult.

A method of predicting inertia-loading effects due to transducers is presented by Ole Dossing [14]. Dossing uses the theory of structural dynamics modification, and arrives at the following relation for predicting natural frequency shifts due to inertia-loading [14],

$$\omega_r^2 = \frac{\omega_{orig}^2}{1 + \frac{2 R_{iir}^{(acc)}}{j\omega_{rd}} \cdot \delta m_i} \quad (2.1)$$

where, ω_{orig} denotes the natural frequency of the original structure, ω_{rd} and $R_{iir}^{(acc)}$ are the damped natural frequency and the driving-point residue, respectively, from accelerance measurements. The quantity δm_i denotes the amount of mass added or removed from the coordinate of interest. McConnell [15] studies the sensitivity and measurement errors of force transducers, demonstrating that the maximum error occurs at resonances of the structure being tested. The typical case of force transducer-stinger-exciter combination is explored. Assuming that the natural frequency of the force transducer is ten times that of the structure's resonance, the maximum and minimum errors that are encountered are shown [15] for mass-ratios (ratio of mass of the structure to that of the transducer-exciter assembly) ranging from 0.001 to 1. For a mass-ratio of 0.01, he shows [15] that amplitude errors can be as high as 27 % and phase errors can be up to 26 degrees, at the structure's resonances. McConnell [15] also investigates the sensitivity of the force transducer to bending moment and shear loads. Through an experiment he shows [15] that the force transducer response can change substantially, in the presence of bending and shear loads. He also reports [15] concomitant changes in the voltage-to-force sensitivity of the force transducer. Also, he [15] explores the effect of the mass of impact hammer and tip on the transducer's sensitivity, when used for impact testing. Walter [16] provides some basic factors and insights into accelerometer transduction, specifications and calibration techniques. Transducer cross-axis sensitivity is another important factor. Han and McConnell [17] discuss the effect of transducer cross-axis sensitivity in exper-

imental modal analysis. They develop [18] a theoretical tri-axial accelerometer model to explain the characteristics of cross-axis sensitivity. Using this model they [18] show that a tri-axial accelerometer is required to measure the true acceleration components, where the cross-axis sensitivity of each accelerometer is known with respect to the other two directions. The authors [18] demonstrate the validity of the model by removing the cross-axis contamination from measured FRF data, using the proposed correction model, and comparing it with data from a known structure.

The excitation methods used in modal testing are numerous and they have a direct impact on the quality of the modal parameters. Each excitation method has its own advantages and disadvantages and a judicious choice has to be made in using the best excitation method in a given situation. The choice of an excitation method depends on several, if not many factors. A very definitive survey of excitation techniques that were available in the late seventies is made by Brown, Carbon and Ramsey [19]. They [19] recommend impact, pure random and periodic random excitations. They state [18] that impact testing, due to its simplicity and speed, is attractive if a quick evaluation is desired. The pure random excitation, according to the authors [18], provides the best linear approximation to a system with nonlinearities, though frequency resolution and leakage are associated problems. The periodic random excitation, although alleviating the frequency resolution and leakage problem, is much slower than continuous random and impact excitation methods [19]. Burst random excitation suggested by Olsen [20], seeks to combine the favourable features of true random and impact excitations. A detailed comparison of excitation functions for structural FRF measurements is made by Olsen [21]. Olsen compares [21] the merits and demerits of random, periodic, transient, steady-state sine and operating excitations, based on leakage/windowing, measurement speed, linear/nonlinear systems, signal-to-noise ratios, etc. Most of the popular excitation methods, with the exception of impact excitation, require the use of an electrodynamic shaker. Further, a few to a many shakers are used if multiple input/output procedures are used for FRF measurements. Though using a shaker is an attractive proposition, there are several "measuring system/process interaction" problems they introduce. The electrodynamic interaction between the

shaker and structure is discussed in great detail by Rao [22]. From his investigations Rao [22] concludes that grounded structures need lighter armatures while heavier armatures are required for free structures. Olsen [23] identifies and discusses some important problems in using electrodynamic shakers and suggests means to overcome them. One of the main problems in using electrodynamic shakers is the drop-off in force output by the shaker at structural resonances. Based on his analysis Olsen [23] concludes that the dominant and controllable parameter which contributes to the force drop-off is the armature mass of the shaker. He [23] suggests that minimizing armature mass would significantly reduce the force drop-off encountered at structural resonances. The problem of force drop-off is also reviewed by Peterson and Mouch [24]. They [24] show how the amount of force drop-off could be reduced and suggest practical methods to get around the problem. Peterson [25] compares the pros and cons of three different modal excitation techniques, viz., impact, random and burst random. He [25] points out that burst random yields better FRFs than continuous random excitation, and continuous random produces superior FRFs than those obtained through impact excitation. The problems and errors associated with impact testing and their reconciliation is discussed by Corelli and Brown [26]. Sohaney and Nieters [27] review proper use of weighting functions to be used with impact testing. Many aspects of signal processing influence the quality of the experimental model. The phenomenon of aliasing, leakage, etc. can corrupt the frequency-domain data. Also, windowing and its effect on data have to be understood. A very comprehensive review of the various window functions used for harmonic analysis with the discrete Fourier transform is made by Harris [28].

The test-configuration, in other words, physical supporting of the test structure, electrodynamic shakers, transducers, etc. is also an important aspect of every modal test. An ideal configuration would be one that isolates the structure completely and is such that the boundary conditions could be simulated accurately in the analytical model. Soucy and Deering [29] show how data acquisition conditions can affect the modal parameters estimated. By using a light-weight beam they [29] investigate the influence of exciter location, exciter suspension and cable attachment, among other parameters, on the estimated modal parameters. They [29] report that the damping estimates are

affected the most, while the residue estimates are relatively stable. Wang, Wei and Wei [30], using a T-plate, demonstrate that simple boundary conditions like clamped, free, etc. do not exist in practice. Also, when substructure synthesis is implemented via experimental modal analysis, rigid-body modes of the individual substructures have to be determined. In such cases the way a substructure is supported and excited influences the accuracy of the estimated rigid-body modes. Lamontia [31], using the quantities residual flexibility and inertia restraint in the receptance form of FRF equation,

$$H_{jk}(\omega) = \frac{x_j}{f_k} = -\frac{Y_{jk}}{\omega^2} + \sum_{r=1}^n \frac{A_{jk}^r}{\omega_r^2 - \omega^2 + i(2\zeta_r\omega_r\omega)} + Z_{jk} \quad (2.2)$$

presents procedures for estimating the inertia restraint Y_{jk} through analytical and analytical/experimental approaches. Also, the effects of not including inertia restraints for structures tested in free-free conditions are shown [31] through an example. Okubo and Furukawa [32] establish a criterion for realizing a free-free state in testing, with respect to supporting and exciting of structures. The criteria [32] states that the degree of free-free conditions realized is proportional to the amount of response, in the frequency range from 0 to the first anti-resonance. Further, the response in this frequency range is required to be uniform (flat) in accelerance measurements. They [32] also discuss various support/excitation methods to achieve free-free testing conditions.

The estimation of frequency response function (FRF) is a very important and crucial stage of the EMA process. Over the last decade a number of researchers were concerned with the development of an estimator which yields the true FRF, which could be equationally stated as

$$H_0(\omega) = \frac{G_{uv}}{G_{vv}} \quad (2.3)$$

Since the measured signals are contaminated with noise, several estimators, each differing the other in its treatment of measurement noise, were developed. Bendat [9] stated that the optimal FRF estimator could be obtained as,

$$H_1(\omega) = \frac{G_{xy}}{G_{xx}} \quad (2.4)$$

The above model, which is insensitive to output noise, is susceptible to noise at the input. Mitchell [33] pointed to the fact that in structural applications interest dwells around the resonance regions of the FRF. He showed [33,34] that the H_1 estimator is highly biased at resonances, where the force delivered by an electrodynamic shaker drops to noise levels due to shaker-structure impedance mismatch. He proposed an estimator [33,34] which was formulated by minimizing the noise at the input. The estimator, and its relationship to the coherence function and the H_1 estimator are given as,

$$H_2(\omega) = \frac{G_{yy}}{G_{yx}} \quad \gamma_{xy}^2 = \frac{H_1}{H_2} \quad (2.5)$$

For the general case in which noise is present in both the input and output measurements, Mitchell showed [33,34] that H_2 was a better estimator at resonances and a poorer estimator at anti-resonances, the opposite being true for the H_1 estimator. The accuracy of the FRF required around regions of resonance and the force drop-off encountered there-in, indeed, seems to be an ironic situation. In this context the H_2 has been widely accepted to be a better estimator. Further, Mitchell [34] presents another estimator, the H_3 estimator, which is obtained as an arithmetic mean of H_1 and H_2 estimators. This estimator is shown [34] to yield lesser biased estimates than those provided by H_1 or H_2 , due to the fact that the latter yield positively and negatively biased estimates respectively. The performance of the H_1 and H_2 estimators have been investigated by several authors [35-37]. Several important aspects of the FFT-based approach, viz., frequency resolution, leakage/windowing, etc., as it impacts the FRF estimated by H_1 and H_2 estimators, are investigated by Cawley [35]. He [35] shows that the accuracy of the FRF estimates obtained by FFT-based

methods depend on the product of frequency, f_n , and the damping factor, η , divided by the frequency resolution, Δf . If a shaker is used to excite the structure, the accuracy obtained is also shown [35] to be a function of the ratio $\frac{s}{\eta}$, where s is the ratio of effective shaker plus force gauge mass to the modal mass of the structure. The error in the FRF estimate is shown [35] to increase with the ratio $\frac{s}{\eta}$, and through-out H_2 being the more accurate of the two estimators. Also, according to Cawley [35], the frequency resolution (and hence the testing time) for a given accuracy is reduced by 50% if the H_2 estimator is used. This is due to the fact that resonance amplitudes are under-estimated due to finite frequency resolution used, and since $H_2 > H_1$ for a non-unity coherence condition, the H_2 estimator yields better estimates [35].

The H_1 and the H_2 are univariate estimators in that they minimize the effects of noise at either the input or the output. Several estimators that seek to minimize the effects of noise at both the input and output were developed by several researchers [34,36,38,39]. Such a bivariate estimation is implicit in the H_3 estimator proposed by Mitchell [34]. Rocklin, Crowley and Vold [36] present an estimator, called the H_v estimator, that is a geometric mean of the H_1 and H_2 estimators,

$$H_v(\omega) = \frac{G_{yx}}{|G_{yx}|} \sqrt{\frac{G_{yy}}{G_{xx}}} \quad (2.6)$$

Though this estimator yields substantially less biased estimates, in the average sense, it is still biased at resonances. These authors compare [36] the H_1 , H_2 and H_v estimators on the basis of parameters like excitation techniques, structure type and modal parameter extraction methods (circle-fits, peak-picking and polyreference). They conclude [36] that the H_v estimator would yield better results when leakage and nonlinearities are present, and are the causes of poor coherence, and when wide-band parameter estimation methods are used. A very detailed work involving the estimation of FRF in the presence of uncorrelated signals has been carried out by Wicks [38]. An estimator developed through this work is presented by Wicks and Vold [39], and is given by

$$H_s(\omega) = \frac{G_{yy} - s^2 G_{xx} + \sqrt{(s^2 G_{xx} - G_{yy})^2 + 4s^2 G_{xy} G_{yx}}}{2 G_{yx}} \quad (2.7)$$

In the above estimator the ratio of the autospectra of input and output noise, s^2 , is assumed to be known *a priori*. The accuracy of this ratio s^2 determines the accuracy of the FRF estimate. An unbiased estimator introduced by Goyder [7] sought to eliminate the problems associated with uncorrelated content (noise) in the measured input and output signals. In his approach [7], Goyder used a third measurement channel that would serve as a reference, from the standpoint of recognizing noise in the input and output measurements. Goyder used [7] the random signal supplied by the signal generator to the shaker, in random excitation tests, as the reference signal $s(t)$. He obtained [7] the estimator by forming cross-spectra of the input and output with this reference signal. The estimator, called the H^c estimator, is given by [7]

$$H^c(\omega) = \frac{G_{sy}}{G_{sx}} \quad (2.8)$$

The idea behind this estimator is that any uncorrelated content with input and output measurements is eliminated while averaging the cross-spectral data. A detailed investigation of the performance of the H^c estimator was carried out by Mitchell, Cobb, Deel and Luk [8]. The authors show [8] that this estimator provides an unbiased estimate of the true FRF in the presence of uncorrelated noise content in both the input and output measurement. The authors point out [8] that this estimator, however, possesses a bias error due to finite sample size.

The performance of these various FRF estimators in terms of the resulting modal parameters of a system, compared to the true modal parameters, has not been clearly understood. However, Wicks and Han [37] present an interesting study on the influence of FRF estimation method on modal parameter estimators. They formulate [37] an FRF for an arbitrary degree-of-freedom system and perform Monte-Carlo simulation in the frequency-domain. In their study [37] they use a random forcing function with a known amount of noise at both the input and output. The force drop-off at resonances is simulated by weighting the forcing function with the imaginary part of the FRF. They compare [37] the performance of H_1 , H_2 , H_s and H^c estimators on the basis of accuracy of the modal parameters estimated, using a global frequency domain parameter estimation method [10]

which uses Forsythe orthogonal polynomials. From their study [37] they conclude that the H_1 estimator yields biased results for damping and residue, identified as being due to the shaker-structure impedance mismatch at resonances. They also conclude [37] that the H_r and H^e are good estimators, if a truly independent source signal is present for the latter and the ratio s^2 is known for the former.

A number of factors contribute to the accuracy of FRF data. The FRF estimators developed typically consider only measurement noise in arriving at a model. Errors due to leakage, frequency resolution, nonlinearities and excitation type are often very hard to quantify in terms of FRF data. Hence, the coherence function has been used universally to validate FRF data. The shortcomings of the coherence function as an FRF data quality indicator has been pointed out by Smiley, Patrick and Sohaney [40]. They proposed a new index, a quality function Q ,

$$Q = \left[\frac{1}{1 + \frac{\Delta f}{f}} \right]^2 \left[\frac{1}{1 + \frac{\left| \frac{d^4 H(f)}{df^4} \right|}{H(f)}} \right] \quad (2.9)$$

in the range 0 to 1, which accounts for noise and insufficient frequency resolution in the FRF estimation. The authors demonstrate [40] the performance of the quality function, in comparison to the coherence function, for a practical measurement. Cobb [41] developed methods, based on the three-channel measurements used for H^e type estimator, that could be used to quantitatively estimate the uncorrelated content in the input and output measurements. These estimation methods are shown to be useful in detecting leakage, extraneous noise [41] and nonlinear behavior, along with the information of their sources.

Detection and identification of nonlinearities in a system during the course of a modal test has been addressed in the literature by several authors [42-44]. Kirshenboim and Ewins [42] have proposed a J factor to characterize the extent of system nonlinearity, on a 0 to 1 scale. He and Ewins [43] use a method based on FRF acquired using sine excitation and a single-degree-of-freedom as-

sumption. By separating the real and imaginary part of the inverse FRF, they identify [43] the type of nonlinear element involved (stiffness and damping). Nonlinear systems exhibit a variety of phenomenon which are unique to the type of nonlinearity present. Generally speaking, all aspects of modal testing can contribute to inaccurate detection and identification, if the system happens to be nonlinear. Zavodney [44] explores some of these possibilities.

A number of frequency-domain parameter estimation algorithms are in use today. Over the last decade several innovative approaches were suggested by researchers for identifying modal parameters directly from estimated FRFs. Ibrahim [45] reviews and assesses many of these methods. The MDOF approaches were a logical and natural extension of SDOF methods, which were inadequate for identifying parameters of systems with substantially coupled modes. One of the first demonstrations of a MDOF capability was made by Richardson and Potter [46], in which the following form of the FRF (partial fraction form) was used,

$$H_{jk}(\omega) = \sum_{r=1}^N \left[\frac{A_{jk}^r}{(i\omega - s_r)} + \frac{A_{jk}^{r*}}{(i\omega - s_r^*)} \right] \quad (2.10)$$

The authors [46] used a least-squares minimization scheme to estimate the modal parameters. Brown, Allemang, Zimmerman and Mergeay [47] outline and discuss several techniques, both SDOF and MDOF, for identifying modal parameters from measured data. The theory behind SDOF methods like peak-picking, circle-fit, etc. are discussed [47]. The MDOF methods discussed [47] are based on the following equation,

$$H_{jk}(\omega) = L_{jk} + \sum_{r=1}^N \left[\frac{A_{jk}^r}{(i\omega - s_r)} + \frac{A_{jk}^{r*}}{(i\omega - s_r^*)} \right] + Z_{jk} \quad (2.11)$$

which accounts for the residual effects due to out-of-band modes. They present [47] a linear least-squares algorithm to determine the residues, the natural frequencies and damping ratios having been

determined earlier by some other method. The authors also discuss [47] a linearized least-squares algorithm for all modal parameters.

Methods developed over the last decade perform a nonlinear least-squares estimation with appropriate weighting. Since nonlinear least-squares estimation is attempted, numerical stability and sensitivity, typically, has been a problem with these modern techniques [48]. The method proposed by Richardson and Formenti [48], which draws significantly from the complex exponential algorithm in the time-domain, seeks to overcome several of these problems. They use [48] the rational fraction form of the FRF,

$$H(\omega) = \frac{\sum_{k=0}^m a_k s^k}{\sum_{k=0}^n b_k s^k} \quad (2.12)$$

and make use of orthogonal polynomials to curve-fit the experimental data. The authors demonstrate [48] that the use of orthogonal polynomials, instead of ordinary polynomials, alleviates the ill-conditioning problem in addition to reducing the number of equations to be solved. In a subsequent paper [49], the authors show that estimating the natural frequencies and damping ratios first and using these estimates in a second curve-fitting process yields better estimates of the parameters. The method, called the global method, is shown [49] to yield much better results for situations in which substantial modal coupling and measurement noise are present. However, they point out [49] that the global method would yield erroneous results if the global properties (natural frequencies and damping ratios) vary substantially from one location (measurement) to another. Curve-fitting methods are typically judged on the basis of their capability of handling the following situations,

- Systems with low/high damping
- Systems with closely coupled modes

- Systems with high modal densities
- Measurement noise/inadequate frequency resolution in the estimated FRFs.

Turunen [50] uses mathematical parameter estimation theory to develop statistical limits to the accuracy of the estimated modal parameters. Specifically, the impact of signal/noise ratios, model order used and the algorithm (linear, nonlinear, etc.) are studied [50]. Two synthesized models, one with four well-separated poles and the other with four closely coupled modes, with synthesized white noise to simulate measurement noise, are used in the investigation [50]. The author shows [50] that linear algorithms produce estimates which are often highly biased and have a variance which exceeds the theoretical minimum. Also, near signal-to-noise ratio threshold, linear algorithms produce estimates with larger bias than variance [50]. In other words, he states that the results are repeatable but not accurate. Furthermore, it is also shown [50] that for systems with closely spaced modes with low signal-to-noise ratios, very large model orders are required for obtaining reasonable results. This can be particularly troublesome, since this may give rise to computational modes too close to the closely coupled modes in question. Nonlinear algorithms, however, are shown by Turunen [50] to yield optimal results. Lee and Richardson [51] recently studied the accuracy of frequency-domain modal parameter estimation techniques. In their study [51], the authors use synthesized FRF data with three modes and a frequency resolution of 0.0625 Hz. They generate various combinations [51] of FRF data - from light modal coupling to high modal coupling, by varying the frequency spacing between modes and modal damping values. To study the impact of measurement noise the authors [51] use 2.5% random noise in the FRFs, for cases in which measurement noise is a parameter. The performance of an SDOF and MDOF (using rational fraction polynomials [48]) curve-fitting routine is evaluated [51] in the study. The authors [51] report levels of errors that may be incurred in estimating all the four modal parameters, for the various combinations of modal coupling, noise and damping.

The literature surveyed above clearly shows the non-unique nature of each stage of the experimental modal analysis process, in that there are several options available to execute each stage. Further,

it is noted that each stage is a potential source of errors which finally result in an inaccurate modal model. Hence, there is a need for quantitative appraisal of the quality of experimental modal models, as pointed out recently by several authors [6,52]. It is the purpose of this thesis to attempt at quantifying the errors encountered in deriving an experimental modal model.

Chapter 3

Analytical Techniques

The objective of this work is to quantify errors in the experimental modal analysis process. The choice of a test structure is dictated by two requirements. Firstly, the structure should be fairly representative of a general arbitrary structure, in so far as the EMA process is concerned. Secondly, the structure is required to be as simple as possible from the standpoint of analytical modeling. This enables one to build accurate analytical models, which are to be used as the reference. A uniform beam satisfies these requirements adequately. Also, the dynamics of a uniform beam, with associated boundary conditions, are better understood than those of many other structural elements.

In the ensuing Sections equations of motion of straight beams, employing the two most popular theories, viz., the Euler-Bernoulli and the Timoshenko theory, are presented employing a continuum mechanics approach. Subsequently these equations are simplified for specific cases. The Euler-Bernoulli and the Timoshenko beam theories are compared on the basis of the influence of shear deformation and rotatory inertia on the natural frequencies of a simply supported beam. The free vibration problem based on the equations from Euler-Bernoulli theory is stated. The analytical solution for a beam with free-free boundary conditions and sample results for natural fre-

quencies and mode shapes are presented. A brief description of analytical modeling of the experimental test structure is included. Finally, a separate Section is devoted to correlation techniques employed to correlate experimental and analytical models.

3.1 Bending of Straight Beams

Beams are members which undergo bending deformation due to transverse forces. Also, they are subjected to stretching as in the case of bars. Generally, the following assumptions are used to arrive at a model of behaviour:

1. The cross-section of the beam has a longitudinal plane of symmetry.
2. The transversely applied loads lie in the longitudinal plane of symmetry.
3. Sections, initially plane and perpendicular to the longitudinal axis, remain plane after bending.
4. Planes of transverse cross-section do not deform, but may rotate as planes.

Assumptions 1 and 2 are used to exclude any possibility of twisting of the member. However, for small deformations, the twisting and bending deformations can be superposed. This is because of the linearity that could be assumed for small deformations. Implications of assumptions 3 and 4 are that the normal strains in the transverse directions are zero. The equations presented in the following Sections are valid only when the above-stated assumptions are met. However, beams with unsymmetric cross-sections and beams subjected to combined bending and torsion are not uncommon. Theories which take into account such factors could be found elsewhere in most texts on advanced mechanics of materials.

3.1.1 The Euler-Bernoulli Beam Theory

The Euler-Bernoulli beam theory, the so-called classical beam theory, is the simplest and mostly used theory of beam behaviour. It results in a single differential equation that relates transverse deformations to applied loads. A basic assumption of the theory is that the transverse planes not only remain plane after bending but remain perpendicular to the longitudinal axis of the beam. This implies that all the shear strains are zero. The popularity of the theory stems from the fact that for simple boundary conditions exact solutions are readily available. In the following paragraphs, the Euler-Bernoulli beam theory will be used to arrive at the governing equations of motion of a beam⁸. At this time no assumption is made as to the amount of deformation, small or large, that the beam is subjected to. Also, axial loads are allowed to act on the beam. Referring to Fig. 3.1a we can write the following kinematical relations for the displacement components u_1 , u_2 and u_3 along the x , y and z coordinate directions.

$$u_1 = u - z \left(\frac{\partial w}{\partial x} \right) \quad (3.1a)$$

$$u_2 = 0 \quad (3.1b)$$

$$u_3 = w(x,t) \quad (3.1c)$$

The first of the above equations uses the assumption that straight lines normal to the longitudinal axis, x , remain normal. The second equation implies that these lines are inextensible (Poisson effects are ignored). The strain components to be used take into account second-order effects. Using Green's strain definition⁹

⁸ The derivation of these equations of motion follows the procedure outlined in Ref. [53]

⁹ See Frederick, D., and Chang, T.S., *Continuum Mechanics*, Scientific Publishers, Inc., 1972, Cambridge, Massachusetts

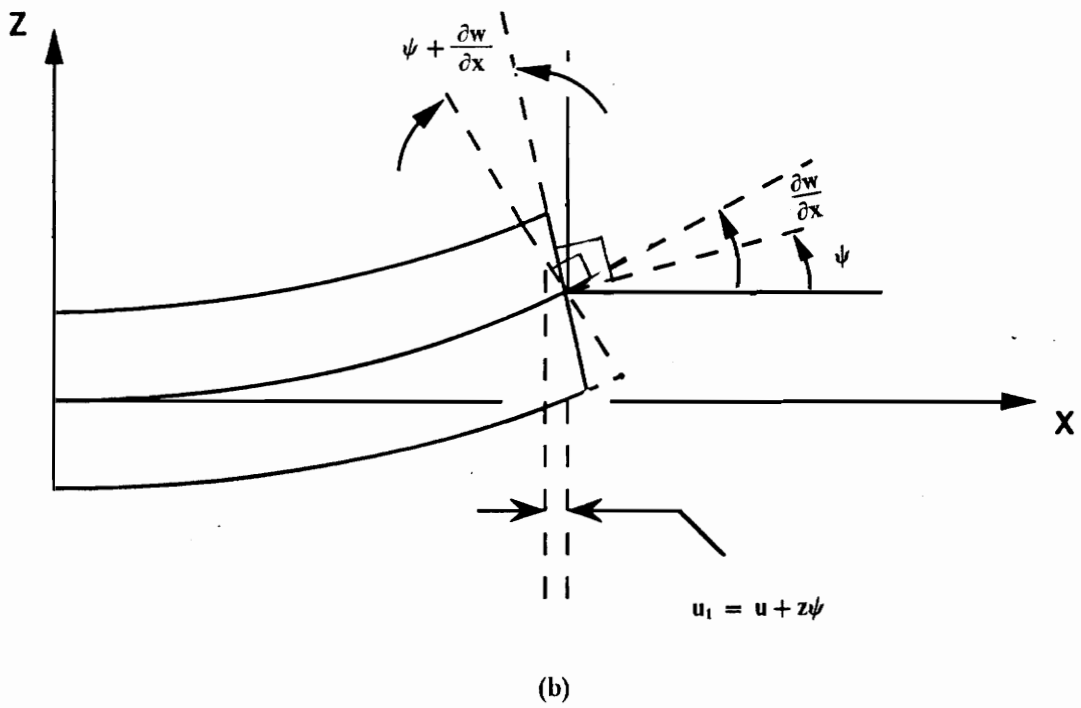
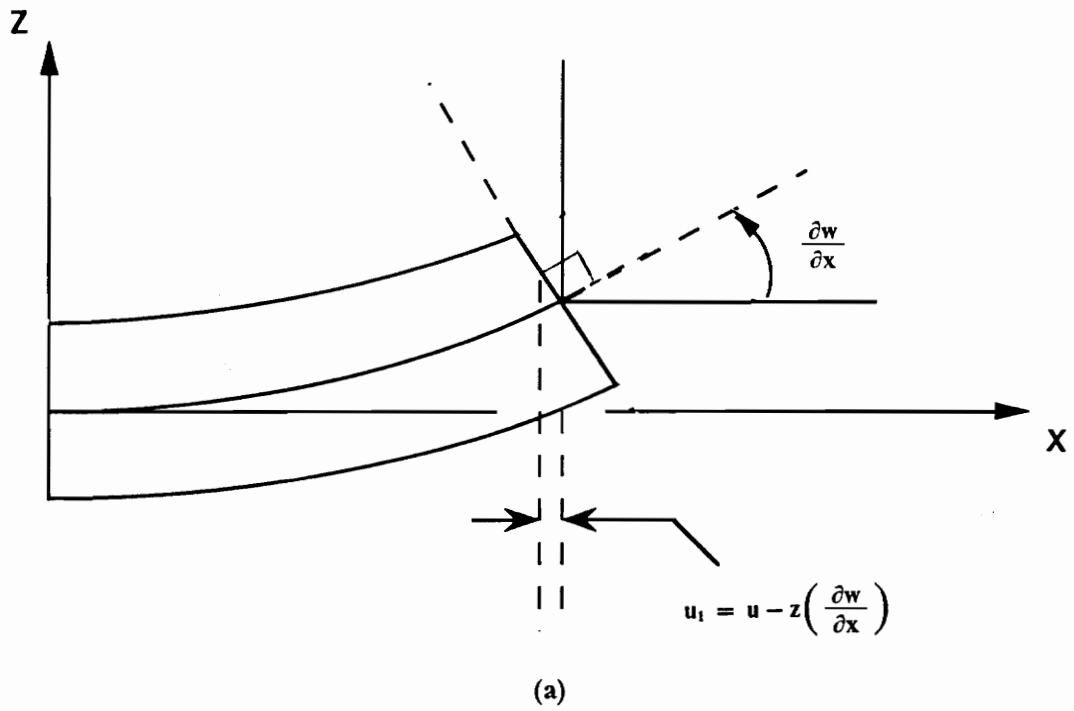


Figure 3.1. Kinematics of deformation in the (a) Euler-Bernoulli beam theory (b) Timoshenko beam theory

$$\{\varepsilon\} = [\varepsilon_x, \varepsilon_y, \varepsilon_z, \varepsilon_{xy}, \varepsilon_{yx}, \varepsilon_{zx}]^T \quad (3.2)$$

where,

$$\varepsilon_x = \frac{\partial u_1}{\partial x} + \frac{1}{2} \left[\left(\frac{\partial u_1}{\partial x} \right)^2 + \left(\frac{\partial u_2}{\partial x} \right)^2 + \left(\frac{\partial u_3}{\partial x} \right)^2 \right] \quad (3.2a)$$

$$\varepsilon_{xy} = \frac{\partial u_1}{\partial y} + \frac{\partial u_2}{\partial x} + \left(\frac{\partial u_1}{\partial x} \frac{\partial u_1}{\partial y} + \frac{\partial u_2}{\partial x} \frac{\partial u_2}{\partial y} + \frac{\partial u_3}{\partial x} \frac{\partial u_3}{\partial y} \right) \quad (3.2b)$$

The strains, for the above assumed displacement field in Eq. (3.1), can be written as,

$$\varepsilon_x = \frac{\partial u}{\partial x} - z \left(\frac{\partial^2 w}{\partial x^2} \right) + \frac{1}{2} \left(\frac{\partial w}{\partial x} \right)^2 \quad (3.3a)$$

$$\varepsilon_y = \varepsilon_z = 0 \quad (3.3b)$$

$$\varepsilon_{xy} = \varepsilon_{yz} = \varepsilon_{zx} = 0 \quad (3.3c)$$

In deriving the above strains, Poisson effects are ignored. If the material is isotropic and linearly elastic, we could write,

$$\sigma_x = E \varepsilon_x$$

$$\sigma_x = E \left\{ \left[\frac{\partial u}{\partial x} - z \left(\frac{\partial^2 w}{\partial x^2} \right) \right] + \frac{1}{2} \left(\frac{\partial w}{\partial x} \right)^2 \right\} \quad (3.4)$$

The internal stresses developed in the beam have to be in equilibrium with the resultant forces and moments at any point. This condition yields the following equations of equilibrium,

$$\int_A \sigma_x dA - P = 0 \quad (3.5)$$

$$\int_A \sigma_x z dA - M = 0 \quad (3.6)$$

Using Eq. (3.4) in Eqs. (3.5 and 3.6), we can write

$$P = EA \left[\frac{\partial u}{\partial x} + \frac{1}{2} \left(\frac{\partial w}{\partial x} \right)^2 \right] \quad (3.7)$$

$$M = -EI \left(\frac{\partial^2 w}{\partial x^2} \right) \quad (3.8)$$

where A denotes the cross-sectional area and I the second moment-of-area of the cross-section about the y -axis. Figure 3.2a shows a cantilever beam with distributed transverse and axial forces acting on it. In Fig. 3.2b the forces and moments acting on an elemental length of the beam (shown in Fig. 3.2a) are shown. Considering the dynamic equilibrium of the transverse forces and the moments about the y -axis of an infinitesimal element of the beam, we arrive at the following equations (see Fig. 3.2b)

$$-P + (P + \Delta P) + p(x_0) \Delta x = \rho A \left(\frac{\partial^2 u}{\partial t^2} \right) \Delta x \quad (3.9)$$

$$-V + (V + \Delta V) - N_x + (N_x + \Delta N_x) + f(x_0) \Delta x = \rho A \left(\frac{\partial^2 w}{\partial t^2} \right) \Delta x \quad (3.10)$$

$$+M - (M + \Delta M) - V \Delta x + f(x_0) \Delta x c \Delta x = \rho A \left(\frac{\partial^2 w}{\partial t^2} \right) \Delta x c \Delta x + M_I \Delta x \quad (3.11)$$

where $x < x_0 < \Delta x + x$ and $0 < c < 1$, which are introduced to account for the non-uniform force f . The quantity N_x denotes the component of the axial force in the transverse direction (z -axis), when the beam is in the deformed configuration. It is given by the relation,

$$N_x = EA \left\{ \frac{\partial u}{\partial x} + \frac{1}{2} \left(\frac{\partial w}{\partial x} \right)^2 \right\} \frac{\partial w}{\partial x} \quad (3.10a)$$

using Eq. (3.7) this could be simplified to,

$$N_x = P \left(\frac{\partial w}{\partial x} \right) \quad (3.10b)$$

The quantity M_I denotes the moment of the axial inertial force per unit length of the beam, which could be obtained as

$$M_I = \int_A \rho \left(\frac{\partial^2 u_1}{\partial t^2} \right) z dA$$

$$M_I = \int_A \rho \frac{\partial^2}{\partial t^2} \left[u - z \left(\frac{\partial w}{\partial x} \right) \right] z dA = \rho I \frac{\partial^2}{\partial t^2} \left(\frac{\partial w}{\partial x} \right) \quad (3.12)$$

The term on the right-hand side is called *Rotatory Inertia*, the product of mass moment-of-inertia ρI and the angular acceleration $\frac{\partial^2}{\partial t^2} \left(\frac{\partial w}{\partial x} \right)$. Dividing Eqs. (3.9 through 3.11), by Δx and taking the limit $\Delta x \rightarrow 0$, we obtain

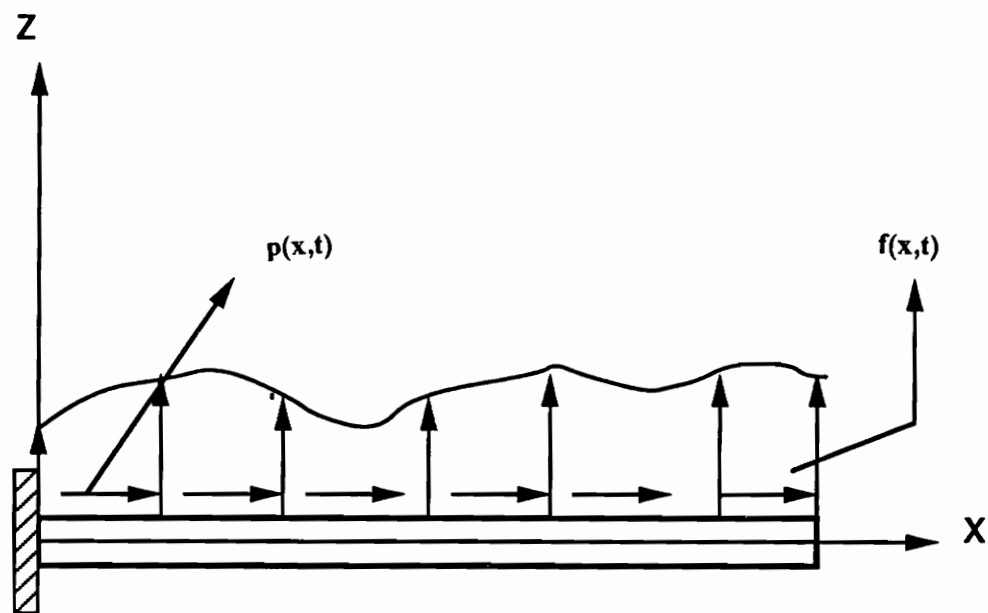
$$\frac{\partial P}{\partial x} + p = \rho A \frac{\partial^2 u}{\partial t^2} \quad (3.13)$$

$$\frac{\partial V}{\partial x} + \frac{\partial N_x}{\partial x} + f = \rho A \frac{\partial^2 w}{\partial t^2} \quad (3.14)$$

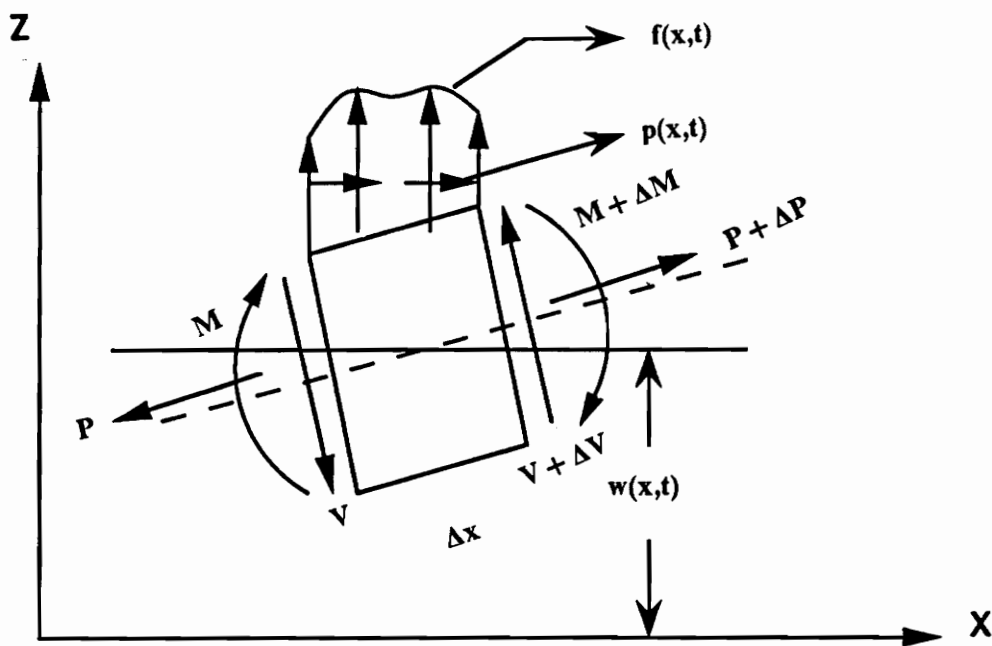
$$-\frac{\partial M}{\partial x} - V = M_I \quad (3.15)$$

Equations (3.13) through (3.15) can now be reduced to two equations, in which transverse deflection w and the axial deflection u are the primary unknowns. That is,

$$-\frac{\partial}{\partial x} \left[EA \left\{ \frac{\partial u}{\partial x} + 1/2 \left(\frac{\partial w}{\partial x} \right)^2 \right\} \right] + \rho A \frac{\partial^2 u}{\partial t^2} = p(x,t) \quad (3.16)$$



(a)



(b)

Figure 3.2. (a) Beam in loaded configuration (b) Forces and moments acting on an elemental length of the beam

$$\begin{aligned} & \frac{\partial^2}{\partial x^2} \left[EI \frac{\partial^2 w}{\partial x^2} \right] - \frac{\partial}{\partial x} \left[EA \left\{ \frac{\partial u}{\partial x} + \frac{1}{2} \left(\frac{\partial w}{\partial x} \right)^2 \right\} \frac{\partial w}{\partial x} \right] \\ & + \rho A \frac{\partial^2 w}{\partial t^2} + \rho I \frac{\partial^2}{\partial t^2} \left(\frac{\partial^2 w}{\partial x^2} \right) = f(x,t) \end{aligned} \quad (3.17)$$

The above are the equations governing the motion of an isotropic elastic beam, with axial forces and second-order effects taken into account, according to the Euler-Bernoulli theory.

3.1.2 The Timoshenko Beam Theory

The Timoshenko beam theory, as opposed to the Euler-Bernoulli theory, takes into account the transverse shear strains. As a result, the assumption that planes normal to the longitudinal axis remain normal after deformation cannot be used anymore. This is because of the fact that these planes undergo an additional rotation $\kappa(x,t)$ due to shear deformation. This can be seen from the geometry of deformation in Fig. 3.1b. Thus, the total slope is composed of two parts, the slope $\frac{\partial w}{\partial x}$ due to bending of the beam and the slope κ due to shearing of the beam. The total (true) slope, therefore, is denoted by

$$\psi(x,t) = \frac{\partial w(x,t)}{\partial x} + \kappa(x,t) \quad (3.18a)$$

Figure 3.1b shows the kinematics of deformation assumed in the theory. The following are the kinematical relations¹⁰

$$u_1 = u + z \psi \quad (3.18b)$$

$$u_2 = 0 \quad (3.18c)$$

¹⁰ These equations were developed in Ref. [53]

$$u_3 = w(x, t) \quad (3.18d)$$

The strains associated with the above displacement field are,

$$\varepsilon_x = \frac{\partial u}{\partial x} + z \left(\frac{\partial \psi}{\partial x} \right) + \frac{1}{2} \left(\frac{\partial w}{\partial x} \right)^2 \quad (3.19a)$$

$$2 \varepsilon_{xz} = \psi + \frac{\partial w}{\partial x} \quad (3.19b)$$

Again, Poisson effects are neglected, and therefore all other strain components are assumed to be zero. Using the conditions of equilibrium of internal moments and equilibrium of internal axial and transverse forces (since transverse strains are accounted for), the following equations are obtained

$$\int_A \sigma_x dA - P = 0 \quad (3.20)$$

$$\int_A \sigma_x z dA - M = 0 \quad (3.21)$$

$$\int_A K \sigma_{xz} dA - V = 0 \quad (3.22)$$

where K denotes the shear correction coefficient, introduced to account for the difference in the constant state of shear stress in the theory and the parabolic variation of the actual shear stress. Solving Eqs. (3.20 through 3.22), the quantities P , M and V are obtained. Thus,

$$P = EA \left[\frac{\partial u}{\partial x} + \frac{1}{2} \left(\frac{\partial w}{\partial x} \right)^2 \right] \quad (3.20a)$$

$$M = EI \frac{\partial \psi}{\partial x} \quad (3.21a)$$

$$V = KGA \left(\psi + \frac{\partial w}{\partial x} \right) \quad (3.22a)$$

The moment of the axial inertial force per unit length of the beam, M_I , in this case would be

$$M_I = \int_A \left(\rho z \frac{\partial^2 \psi}{\partial t^2} \right) z dA = \rho I \frac{\partial^2 \psi}{\partial t^2} \quad (3.23)$$

Substituting Eqs. (3.20a through 3.22a) into Eqs. (3.13 through 3.15), we obtain

$$-\frac{\partial}{\partial x} \left[EA \left\{ \frac{\partial u}{\partial x} + \frac{1}{2} \left(\frac{\partial w}{\partial x} \right)^2 \right\} \right] + \rho A \frac{\partial^2 u}{\partial t^2} = p(x,t) \quad (3.24)$$

$$-\frac{\partial}{\partial x} \left[EI \frac{\partial \psi}{\partial x} \right] + KGA \left(\frac{\partial w}{\partial x} + \psi \right) + \rho I \frac{\partial^2 \psi}{\partial t^2} = 0 \quad (3.25)$$

$$-\frac{\partial}{\partial x} \left[EA \left\{ \frac{\partial u}{\partial x} + \frac{1}{2} \left(\frac{\partial w}{\partial x} \right)^2 \right\} \frac{\partial w}{\partial x} \right] - \frac{\partial}{\partial x} \left[KGA \left(\frac{\partial w}{\partial x} + \psi \right) \right] + \rho A \frac{\partial^2 w}{\partial t^2} = f(x,t) \quad (3.26)$$

Thus the Timoshenko theory, in which axial forces and second-order strains are included, results in three equations.

3.1.3 Working Forms of the Equations of Motion of a Beam

The equations presented above are quite general in that they can be used for cases in which axial forces and large displacements are present. However, in most situations the vibration problem is

linear and axial forces may not be present. In such situations, the equations of motion presented above could be simplified further. In the following paragraphs, the forms of the above equations used for specific cases are stated.

3.1.3.a Small motions with axial forces

When the displacements are small, second-order effects could be ignored. This results in simple strain-displacement relations, relations in which the square of the derivatives of the displacements are negligible. Thus the terms involving $\left(\frac{\partial w}{\partial x}\right)^2$ in the equations presented until now vanish. This results in the following equations for the Euler-Bernoulli and the Timoshenko theories,

Euler-Bernoulli beam theory

$$-\frac{\partial}{\partial x} \left[EA \left(\frac{\partial u}{\partial x} \right) \right] + \rho A \frac{\partial^2 u}{\partial t^2} = p(x,t) \quad (3.16a)$$

$$\frac{\partial^2}{\partial x^2} \left[EI \left(\frac{\partial^2 w}{\partial x^2} \right) \right] - \frac{\partial}{\partial x} \left[P \left(\frac{\partial w}{\partial x} \right) \right] + \rho A \frac{\partial^2 w}{\partial t^2} + \rho I \frac{\partial^2}{\partial t^2} \left(\frac{\partial^2 w}{\partial x^2} \right) = f(x,t) \quad (3.17a)$$

Timoshenko beam theory

$$-\frac{\partial}{\partial x} \left[EA \left(\frac{\partial u}{\partial x} \right) \right] + \rho A \frac{\partial^2 u}{\partial t^2} = p(x,t) \quad (3.24a)$$

$$-\frac{\partial}{\partial x} \left[EI \frac{\partial \psi}{\partial x} \right] + KGA \left(\frac{\partial w}{\partial x} + \psi \right) + \rho I \frac{\partial^2 \psi}{\partial t^2} = 0 \quad (3.25a)$$

$$-\frac{\partial}{\partial x} \left[P \left(\frac{\partial w}{\partial x} \right) \right] - \frac{\partial}{\partial x} \left[KGA \left(\frac{\partial w}{\partial x} + \psi \right) \right] + \rho A \frac{\partial^2 w}{\partial t^2} = f(x,t) \quad (3.26a)$$

3.1.3.b Small motions without axial forces

The case in which the displacements are small and one in which axial forces are absent is the one most commonly encountered in practice. The following equations result,

Euler-Bernoulli beam theory

$$\frac{\partial^2}{\partial x^2} \left[EI \left(\frac{\partial^2 w}{\partial x^2} \right) \right] + \rho A \frac{\partial^2 w}{\partial t^2} + \rho I \frac{\partial^2}{\partial t^2} \left(\frac{\partial^2 w}{\partial x^2} \right) = f(x,t) \quad (3.17b)$$

Timoshenko beam theory

$$-\frac{\partial}{\partial x} \left[EI \frac{\partial \psi}{\partial x} \right] + KGA \left(\frac{\partial w}{\partial x} + \psi \right) + \rho I \frac{\partial^2 \psi}{\partial t^2} = 0 \quad (3.25b)$$

$$-\frac{\partial}{\partial x} \left[KGA \left(\frac{\partial w}{\partial x} + \psi \right) \right] + \rho A \frac{\partial^2 w}{\partial t^2} = f(x,t) \quad (3.26b)$$

3.1.4 Euler-Bernoulli (vs) Timoshenko beam theory

The Euler-Bernoulli theory is very simple, elegant and gives fairly accurate results for lower modes of slender beams. Since inclusion of rotatory inertia term introduces a mixed time derivative, and

since rotatory inertia effects are very small for slender beams at low frequencies, the Euler-Bernoulli theory seldom includes rotatory inertia terms in the equations of motion.

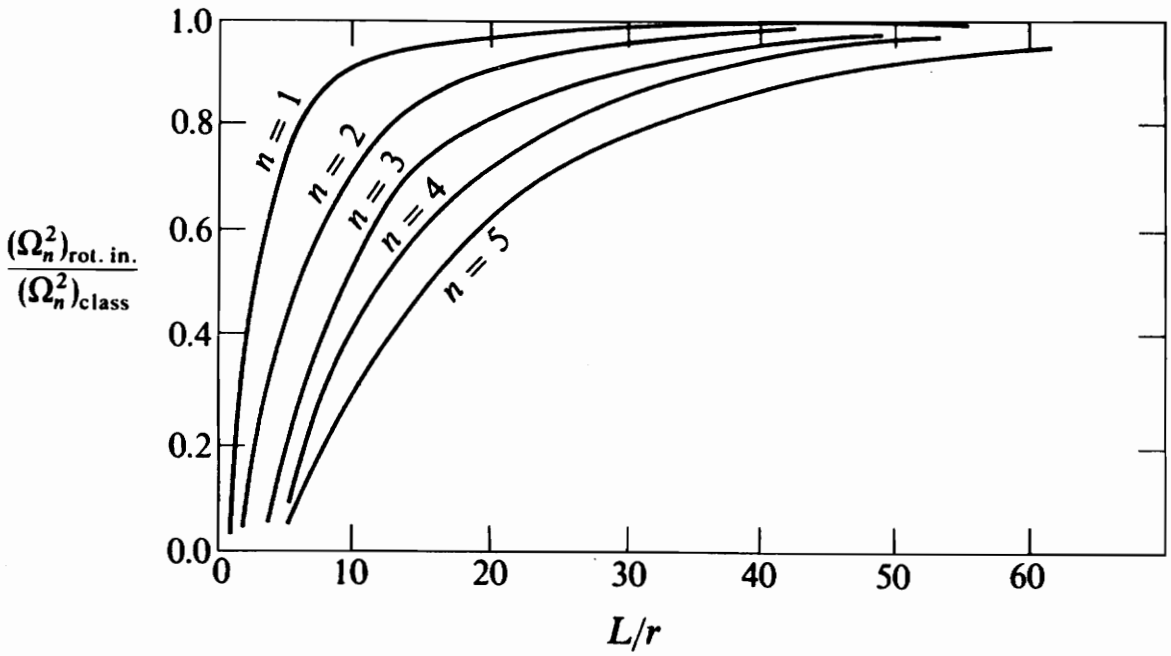
The Timoshenko beam theory accounts for shear deformation and therefore is more accurate than the Euler-Bernoulli theory. Also, accounting for rotatory inertia results in only second-order time derivatives, unlike the Euler-Bernoulli equations. Thus, the standard equations of motion of a beam, according to the Timoshenko theory, accounts for both shear deformation and rotatory inertia effects.

Shear Deformation and Rotatory Inertia Effects

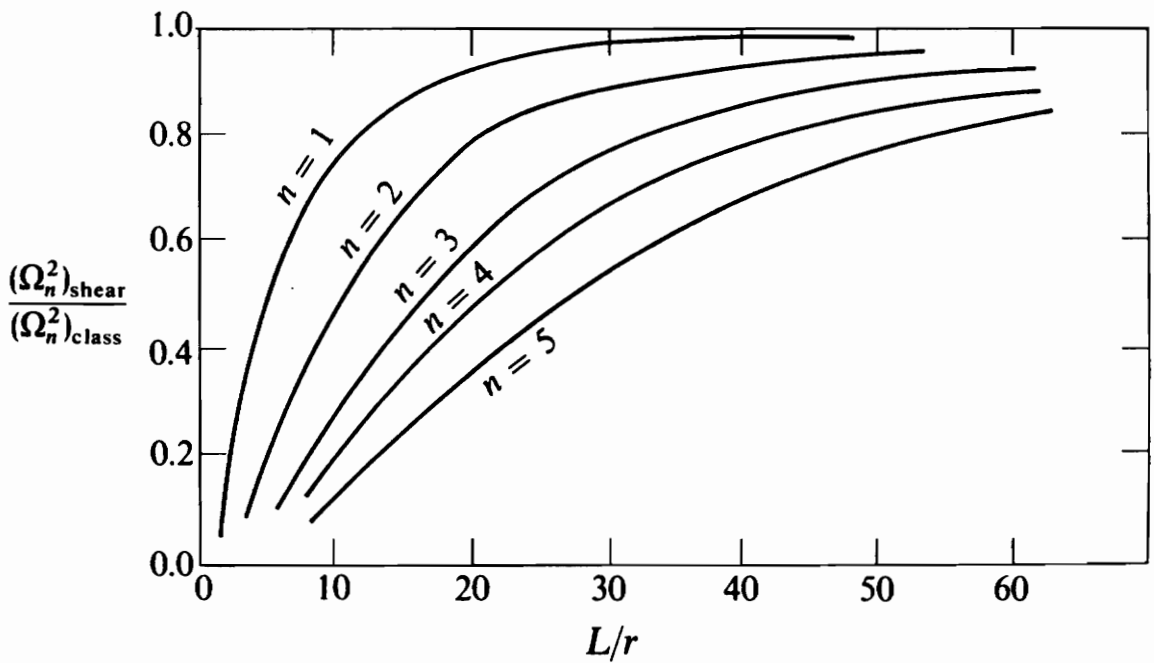
Rotatory inertia and shear deformation effects are significant for beams with small slenderness ratios (stubby beams). However, even for slender beams, rotatory inertia effects become significant at higher frequencies, whereas shear deformation effects become significant at higher modes. Shear deformation makes the beam more flexible, and therefore the effect of shear deformation is to reduce the natural frequencies. Since rotatory inertia adds to the existing inertia effects, the effect of rotatory inertia is to reduce the natural frequencies. Except for the case where the slenderness ratio is very small (stubby beams) shear deformation effects are more significant than rotatory inertia effects. The effects of rotatory inertia and shear deformation on the natural frequencies of a beam with simply supported boundary conditions are shown in Figs.¹¹ 3.3 and 3.4.

The quantities L and r are the length of the beam and radius of gyration about the neutral axis of the beam, respectively. In Figs. 3.3 and 3.4, the quantity $(\Omega_n^2)_{class}$ denotes the natural frequencies of the beam without shear deformation and rotatory inertia effects included (that is, from the classical theory). The quantity $(\Omega_n^2)_{rot.in.}$ denotes the natural frequencies of the beam when only rotatory inertia effects are included, and the quantity $(\Omega_n^2)_{shear}$ denotes the natural frequencies of the beam when only shear deformation effects are included. The quantity (Ω_n^2) denotes the natural

¹¹ Figures 3.3 and 3.4 are taken from Dym, C.L. and Shames, I. H., *Solid Mechanics: A Variational Approach*, McGraw Hill, 1973



(a)



(b)

Figure 3.3. Influence of (a) Rotatory inertia (b) Shear deformation on the natural frequencies of a simply supported beam: taken from Dym, C.L. and Shames, I. H., *Solid Mechanics: A Variational Approach*, McGraw Hill, 1973

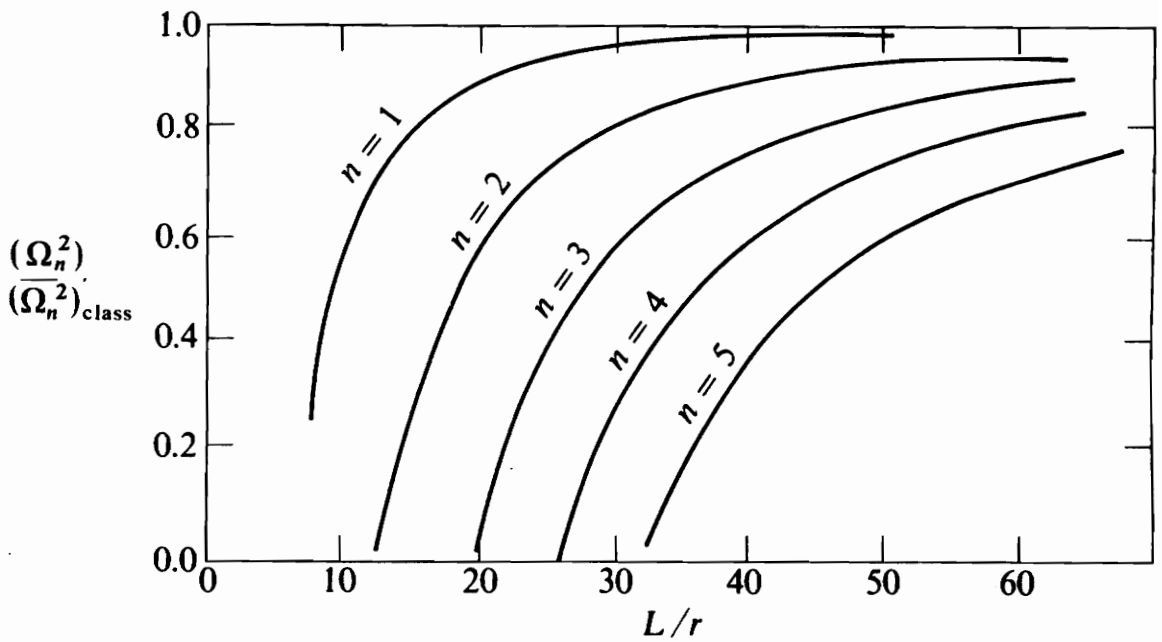


Figure 3.4. Combined effects of rotatory inertia and shear deformation on the natural frequencies of a simply supported beam: taken from Dym, C.L. and Shames, I. H., *Solid Mechanics: A Variational Approach*, McGraw Hill, 1973

frequencies of a beam with both shear deformation and rotatory inertia effects included. Note that the frequency ratios, eg., $\frac{(\Omega_n^2)}{(\Omega_n^2)_{class}}$, and the slenderness ratios, $\frac{L}{r}$, are dimensionless quantities. Figure 3.3a shows the effect of rotatory inertia on the natural frequencies as a function of the slenderness ratio $\frac{L}{r}$, with the mode number n as a parameter. Figure 3.3b shows the effect of shear deformation on natural frequencies, for the same set of variables. From Fig. 3.3, it is clear that shear deformation and rotatory inertia effects are significant for stubby beams, even for the first mode of vibration, e.g., for an $\frac{L}{r}$ ratio of 10 the shear deformation effects are 7% and 42% respectively for the first and the third mode (see Fig. 3.3b), whereas the corresponding rotatory inertia effects are 3% and 20% respectively (see Fig. 3.3a). Further, using an $\frac{L}{r}$ ratio of 60 to represent a less stubbier beam, the shear deformation effects for the first and the third mode are 1% and 10% respectively, whereas the corresponding rotatory inertia effects are approximately 0% and 2% respectively. As can be seen, shear deformation effects are more significant than those due to rotatory inertia, for prismatic structures such as this uniform beam. Figure 3.4 shows the combined effect of shear deformation and rotatory inertia on the natural frequencies of a simply supported beam, for various slenderness ratios.

3.2 *The Free Vibration Problem*

In this Section the standard procedure used to obtain exact closed-form solutions for differential eigenvalue problems resulting from the equations of motion of a beam will be shown. This is done merely to illustrate the oversimplifications that are necessary to make the equations of motion amenable to an exact closed-form solution. No attempt is being made here to obtain exact solutions to the differential eigenvalue problem that correspond to the equations of motion, which were quite general in nature, presented in the earlier Sections.

3.2.1 The Eigenvalue Problem

Consider the Eq. (3.17b) which represents the equation of motion of a beam according to the Euler-Bernoulli theory. Ignoring the effects of rotatory inertia, we can write the following equation if there are no external forces acting on the beam, (See Ref. [54])

$$\frac{\partial^2}{\partial x^2} \left[EI \left(\frac{\partial^2 w}{\partial x^2} \right) \right] = -m(x) \frac{\partial^2 w}{\partial t^2} \quad (3.27)$$

where, we have replaced ρA by $m(x)$ to denote the mass per unit length of the beam. The above is the differential equation for free vibration of a beam, ignoring shear deformation and rotatory inertia effects. Assuming that the solution is separable in space and time, we could write,

$$w(x,t) = W(x) q(t) \quad (3.28)$$

Using Eq. (3.28) in Eq. (3.27) and dividing through-out by $m(x) W(x) q(t)$, we get

$$\frac{1}{m(x) W(x)} \frac{d^2}{dx^2} \left[EI \frac{d^2 W(x)}{dx^2} \right] = -\frac{1}{q(t)} \frac{d^2 q(t)}{dt^2} \quad (3.29)$$

Using the standard procedure, when spatial and temporal independence of the solution is assumed, we write the following equations,

$$\frac{d^2}{dx^2} \left[EI \frac{d^2 W(x)}{dx^2} \right] - \omega^2 m(x) W(x) = 0 \quad (3.30a)$$

$$\frac{d^2 q(t)}{dt^2} + \omega^2 q(t) = 0 \quad (3.30b)$$

Equation (3.30b) is that of a harmonic oscillator, signifying the fact that the equations developed represent a conservative system. This is to be expected since we did not account for forces which dissipate energy (nonconservative). Also, Eq. (3.30a) is a fourth-order differential equation, requiring four boundary conditions to obtain a solution. The problem of obtaining the values for the parameter ω^2 , for which the homogeneous differential equation, Eq. (3.30a), has a non-trivial solution, satisfying the homogeneous boundary conditions, is called the characteristic or eigenvalue problem. The corresponding functions $W(x)$ are called the characteristic or eigenfunctions.

3.2.2 Natural Frequencies and Mode Shapes

In the following paragraphs, the solution to the free-vibration problem of a beam with free-free boundary conditions is presented. It is assumed that the beam is uniform, in which case Eq. (3.30a) reduces to

$$\frac{d^4 W(x)}{dx^4} - \beta^4 W(x) = 0 \quad (3.31)$$

where,

$$\beta^4 = \frac{\omega^2 m(x)}{EI} \quad (3.31a)$$

Since the beam is not geometrically restrained, geometric boundary conditions cannot be specified. However the natural or force boundary conditions at either end could be written as,

$$\frac{d^2 W(x)}{dx^2} \Big|_{x=0} = 0 \quad \frac{d^3 W(x)}{dx^3} \Big|_{x=0} = 0 \quad (3.32a)$$

$$\frac{d^2 W(x)}{dx^2} \Big|_{x=L} = 0 \quad \frac{d^3 W(x)}{dx^3} \Big|_{x=L} = 0 \quad (3.32b)$$

The general solution to the Eq. (3.31) is given by,

$$W(x) = C_1 \sin \beta x + C_2 \cos \beta x + C_3 \sinh \beta x + C_4 \cosh \beta x \quad (3.33)$$

Using the boundary conditions of Eq. (3.32), we arrive at the following frequency equation,

$$\cos \beta L \cosh \beta L = 1 \quad (3.34)$$

which is a transcendental equation and could be solved numerically to obtain the eigenvalues β . The above frequency equation yields a double root, $\beta_0 = \beta_1 = 0$. For $\beta = 0$, Eq. (3.31) reduces to

$$\frac{d^4 W(x)}{dx^4} = 0 \quad (3.35)$$

The general solution to the above equation is,

$$W(x) = D_1 + D_2 x + D_3 x^2 + D_4 x^3 \quad (3.36)$$

Using the boundary conditions in Eqs. (3.32a and 3.32b), the modes corresponding to the double root are obtained as,

$$W_0(x) = A_0 \quad (3.37)$$

$$W_1(x) = A_1 \left(x - \frac{L}{2} \right) \quad (3.38)$$

The above two modes represent correspondingly the rigid-body translation and rotation about the center of mass of the beam. Since β_0 is a double root, any linear combination of $W_0(x)$ and $W_1(x)$ is also a natural mode. Equation (3.34) further yields an infinite sequence of eigenvalues β_r . The frequencies of the first four flexible modes can be obtained by using the following values for the quantity $\beta_r L$,

$$\beta_2 L = 4.730041 \quad (3.34a)$$

$$\beta_3 L = 7.853205 \quad (3.34b)$$

$$\beta_4 L = 10.99561 \quad (3.34c)$$

$$\beta_5 L = 14.13717 \quad (3.34d)$$

Usually, the frequencies of higher modes are approximated by the following relation,

$$\beta_r L \simeq (2r - 1) \frac{\pi}{2} \quad (3.34e)$$

The corresponding eigenfunctions are given by,

$$W_r(x) = A_r [(\cos \beta_r L - \cosh \beta_r L) (\sin \beta_r x + \sinh \beta_r x)] -$$

$$A_r [(\sin \beta_r L - \sinh \beta_r L) (\cos \beta_r x + \cosh \beta_r x)] \quad (3.39)$$

The two rigid-body modes and the first two flexible modes for the bar in free-free vibration are shown in Fig. 3.5. In Fig. 3.5, $Y_r(x)$ denotes the eigenfunction for the r th mode and ω denotes circular natural frequency expressed in radians per second. The data for the beam used in sample results in this Chapter is given in Table 3.1. Sample results for natural frequencies of a bar with free-free boundary conditions are shown in Table 3.2.

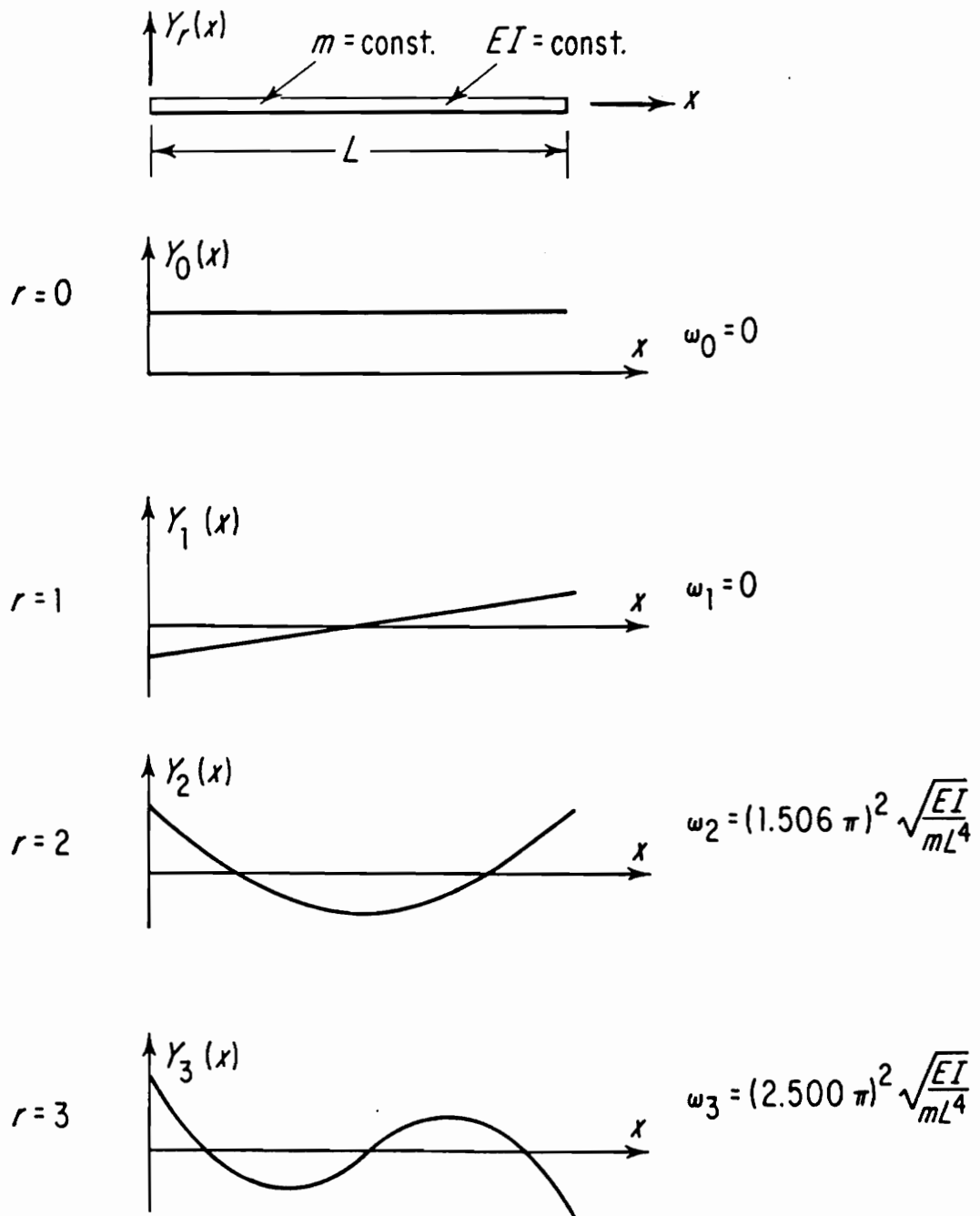


Figure 3.5. First four natural modes of a free-free bar in bending vibration: taken from Ref. [54]

Table 3.1. Material and geometric property values of the beam used in sample results

Material/Geometric Property of the Beam	Value
Young's Modulus	1.9306×10^{11} Pascals
Mass density	7832.3 kg/m^3
Length	1.3970 m
Width	0.07696 m
Depth	0.0066 m

Table 3.2. Natural frequencies of the first 10 flexible modes for a beam with free-free boundary conditions using Euler-Bernoulli theory

Mode Number	Natural Frequency (Hz)
1	17.359
2	47.851
3	93.807
4	155.067
5	231.644
6	323.536
7	430.743
8	553.265
9	691.103
10	844.256

3.2.4 Analytical Modeling of the Test Structure

The beams used in this work are tested in the configuration shown in Fig. 3.6a (schematic). Figure 3.6b shows several aspects that have to be considered in the analytical modeling process to realize an accurate analytical model. Apart from these, factors like shear deformation and rotatory inertia have to be included, if higher modes and frequencies are considered.

As discussed earlier in the Chapter on literature review, the way a structure is supported and excited influences the quality of the modal parameters obtained. The test structure shown in Fig. 3.6a, strictly speaking, is not suitably supported to simulate free-free boundary conditions. Also, this way of supporting loads the structure due to the gravity force. A simple analytical calculation can be made to estimate the frequencies of rigid-body modes, and the corresponding mode shapes.

Assume the structure in Fig. 3.6a is tested with an impact hammer. Referring to Fig. 3.7, using the small-motions assumption, the following linearized equations of motion are derived,

$$\begin{bmatrix} mL_1^2 & \frac{1}{2} mL_1L_2 \\ \frac{1}{2} mL_1L_2 & \frac{1}{3} mL_2^2 \end{bmatrix} \begin{Bmatrix} \ddot{\theta}_1 \\ \ddot{\theta}_2 \end{Bmatrix} + \begin{bmatrix} mgL_1 & 0 \\ 0 & \frac{1}{2} mgL_2 \end{bmatrix} \begin{Bmatrix} \theta_1 \\ \theta_2 \end{Bmatrix} = \begin{Bmatrix} FL_1 \cos \theta_1 \\ FL_2 \cos \theta_2 \end{Bmatrix} \quad (3.40)$$

where L_1 and L_2 denote the lengths of the string and beam respectively. The quantities m and g represent the mass of the beam and the acceleration due to gravity respectively. The vector on the right hand side of Eq. (3.40) contains the generalized forces, where F denotes the force applied in the horizontal direction, as shown in Fig. 3.7. Using Eq. (3.40) the corresponding free vibration and eigenvalue problem could be stated as,

$$[M]\{\ddot{\theta}\} + [K]\{\theta\} = \{0\} \quad (3.40a)$$

$$Det\{[K] - \omega^2[M]\} = 0 \quad (3.41)$$

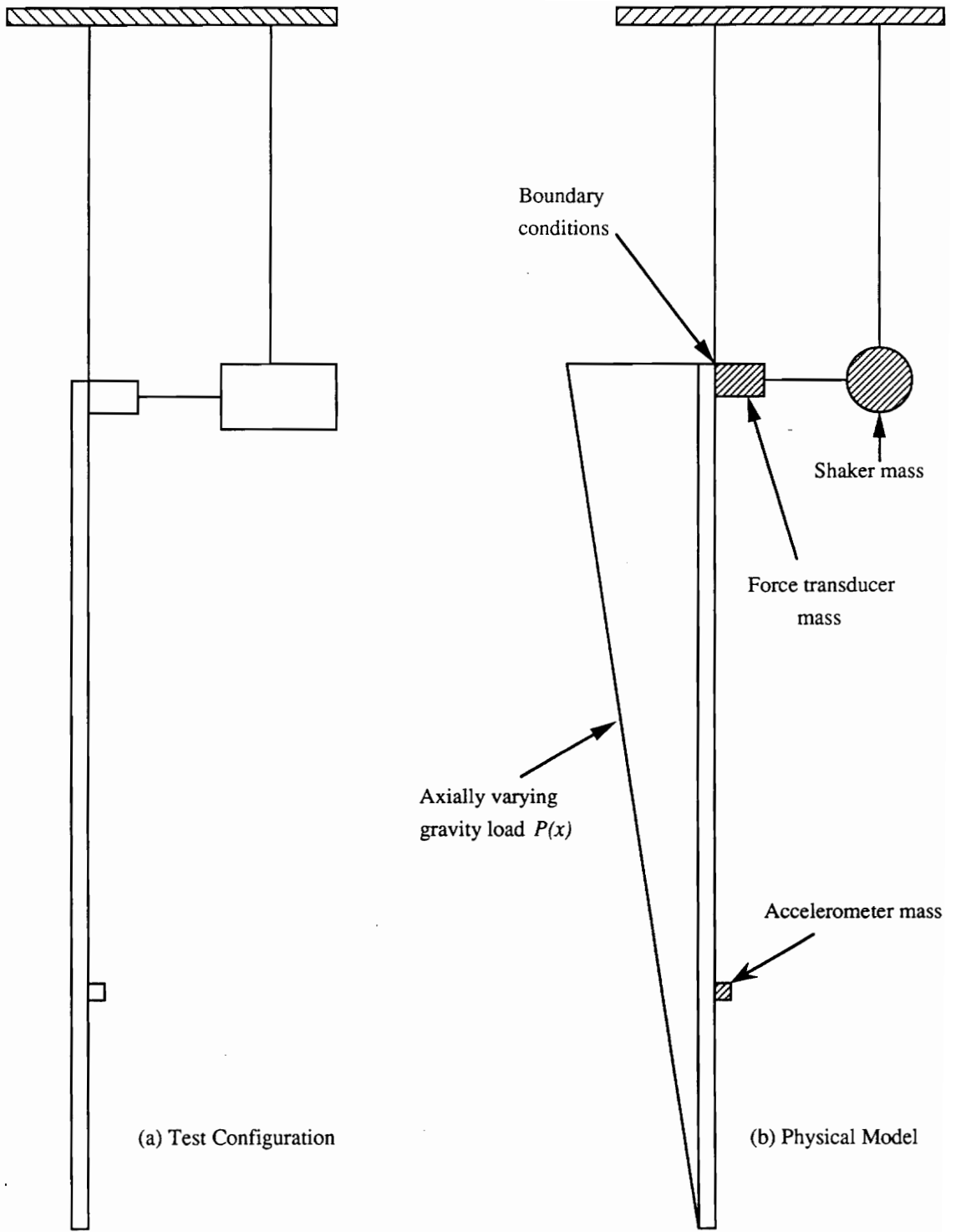


Figure 3.6. Test configuration and the corresponding physical model

For the data, $m = 7832.3 \text{ kg/m}^3$, $L_1 = 1.3208 \text{ m}$, $L_2 = 1.5240 \text{ m}$ and $g = 9.81 \text{ m/sec}^2$, we have the following modal parameters,

$$f_1 = 0.3375 \text{ Hz} \quad \{\phi\}_1 = \begin{Bmatrix} 0.8837 \\ 1.0 \end{Bmatrix} \quad (3.42a)$$

$$f_2 = 1.2719 \text{ Hz} \quad \{\phi\}_2 = \begin{Bmatrix} -0.6529 \\ 1.0 \end{Bmatrix} \quad (3.42b)$$

As can be noticed, the rigid-body modes for a beam with free-free boundary conditions given by Eqs. (3.37 and 3.38) have not been realized.

Next, suspending the beam vertically as shown in Fig. 3.6a induces a body force, due to gravity, which varies axially as shown in Fig. 3.6b. This gives rise to a variable coefficient, $P(x)$, in the differential equations of motion. Also, if the gravity force is modeled, the associated force boundary conditions have to be applied. This may introduce non-classical boundary conditions. Another factor that needs to be accounted for is the inertias of transducer masses, shown in Fig. 3.6b. These introduce a mass distribution that is non-uniform. The combination of these problems complicates the solution process. Therefore, an exact closed-form solution may not be possible. Hence, only approximate solution methods have to be investigated.

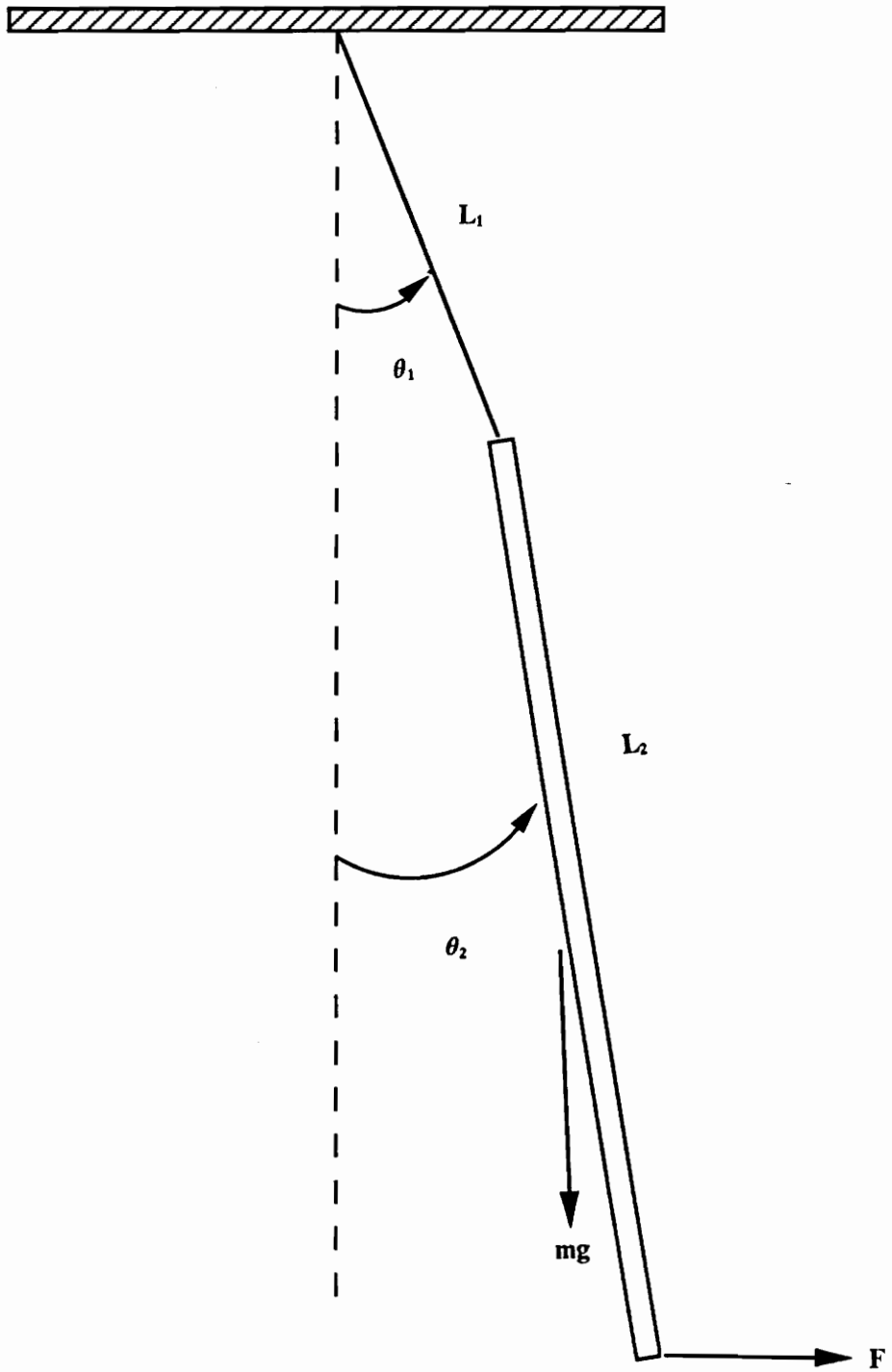


Figure 3.7. A two-degree-of-freedom model for estimating the rigid-body modes of the test structure

3.3 Techniques for Correlation of Experimental and Analytical Structural Dynamic Models

In structural dynamics modeling the experimental and analytical methods are complementary in nature. This has numerous advantages. However, the primary disadvantage of their complementary nature is that they do not have so much in common that can be observed or understood physically. This results in a situation where one cannot confidently argue about the validity of either model, because cross-checking of the physical parameters involved, viz., mass, stiffness and damping, is not possible. The strengths of one are the weaknesses of the other. Therefore, correlation methods that can give valuable insights into the defects in either model are of paramount importance if benefits are to be realized.

The two most commonly available models are those from a modal testing and finite element analysis. Apart from the fact that one is experimental and the other is analytical, a primary difference is that they take different approaches to arrive at the models. According to Ewins [55], three different models are possible and meaningful for comparison. They are:

1. Spatial model
2. Modal model
3. Response model

As mentioned above, the analytical methods start with the spatial model and arrive at the modal model, with which a response model can be built if required. On the other hand, the experimental methods start with a response model and arrive at a modal model, from which a generalized spatial model can be built, i.e., a spatial model in the modal domain. Though direct comparisons between

experimental and analytical modal as well as response models are possible, spatial models can be compared only in the modal domain. This is particularly disadvantageous in that the spatial models in the modal domain represent generalized stiffnesses and masses, i.e., stiffness and masses in modal coordinates, which have no physical meaning. Therefore, most comparisons are restricted to the modal and response models, the former being the most popular. A detailed treatment of correlation of structural dynamic models can be found in an article by Pakstys [56]. Another excellent review is made by Ibrahim [57]. In this work correlation between experimental and analytical models is made using modal models. The following Sections detail some of the techniques used for performing correlation of modal models.

3.3.1 Correlation of Modal Models

By and large, this is the most popular and advanced method used to correlate experimental and analytical models. Since damping is typically not modeled in a finite element model, the only modal parameters that are correlated are natural frequencies (a global property) and mode shapes (a local property) of a structure.

3.3.1.a Natural Frequencies

This is the first comparison made between analytical and test results. A simple comparison of the tabulated natural frequencies is the first step. To gain more insight, a linear plot is made between analytical and experimental natural frequencies. A good correlation is indicated by a straight line whose slope approaches a value of 1. If the slope is more or less than one, then incorrect material property values could be the problem (assuming a converged FE solution in the frequency range). If there are small random deviations from the straight line, then such errors could be experimental.

Thus, if errors exist, insights as to whether they are systematic or random can be obtained from such a plot [55].

3.3.1.b Mode Shapes

There are several methods used in conjunction with each other to correlate experimental and analytical mode vectors. Also, there are several aspects relating to mode vectors obtained experimentally and analytically which need to be mentioned before discussing various techniques used for mode shape correlation. The first problem encountered in correlating experimental and analytical mode vectors is that due to unequal degrees of freedom. Finite element models usually have degrees of freedom which are 1 or 2 orders of magnitude more than that which testing can provide. Of course, correlation can be performed by using those points in the analytical model where information is available from testing. However, if updating of finite element models is to be performed, the test and analytical degrees of freedom should be identical.

The above problem is overcome by reducing the FE model to the same degrees of freedom as the experimental coordinates. Further, rotational degrees of freedom are not measured in a modal test. As a result correlation is performed only for translational degrees of freedom. Several techniques that perform finite element model reduction are in use. The most commonly used method is the Guyan reduction [58]. Though these methods are highly effective, the condensed system of physical matrices involve approximations (mass matrix in the case of Guyan reduction).

3.3.2 Methods for Correlating Mode Shapes

3.3.2.a Visual Inspection

This is the simplest method used to compare mode shapes from test and analysis. It could be very useful if the structure is simple and symmetric. In this case it can reveal locations where analytical or test mode vectors are in error. This approach is also used if other methods for correlating mode vectors yield results which cannot be reconciled with.

3.3.2.b Orthogonality Check Method

If a structural dynamic system is proportionally damped, each mode vector is orthogonal to all other mode vectors of the system when weighted with the physical matrices, viz., mass, stiffness or damping matrix that is a linear sum of mass and stiffness matrices. This fact is used to check the orthogonality of the measured mode vectors. Since the physical matrices are not obtainable from experimental results, recourse is made to matrices obtained from finite element analysis. The most reliable physical matrix that an FE model could provide is the mass matrix, which we shall denote as $[M_{FE}]$. Therefore, orthogonality checks are usually made with respect to the mass matrix. The following relations hold in an ideal situation,

$$\{U_j\}^T [M_{FE}] \{U_i\} = \delta_{ij} M_i \quad (3.43)$$

where U_j denotes the j th mode, M_i the generalized mass of mode i , and δ_{ij} the Kronecker delta function. Alternatively, we can define the mass-normalized mode vectors, $\{\phi_i\}$, as follows,

$$\{\phi_i\} = \frac{\{U_i\}}{\{U_i\}^T [M_{FE}] \{U_i\}} \quad (3.44)$$

Equations (3.43 and 3.44) can be re-arranged to yield

$$\{\phi_i\}^T [M_{FE}] \{\phi_j\} = \delta_{ij} \quad (3.43a)$$

Now we can define the orthogonality check matrix as,

$$[\Phi] [M_{FE}] [\Phi] = [O_c] \quad (3.45)$$

where $[\Phi]$ is the modal matrix which has mass-normalized mode vectors as its columns and $[O_c]$ is the orthogonality check matrix.

Ideally the off-diagonal terms are supposed to be "0". However, such values cannot be realized in practice. Values of 0.1 or less are generally acceptable. The shortcoming of the method is that the mass matrix is from the FE model, which we are trying to validate. Also, due to the smaller number of experimental degrees of freedom, the mass matrix has to be reduced by condensation techniques. If the reduction method is Guyan [58], then the condensed mass matrix is inaccurate. This can cause severe errors. Thus, one cannot identify where the problem lies, in case of poor orthogonality results. It could be either due to the measured mode vectors themselves or due to the FE mass matrix or due to both. Therefore, a more reliable way of establishing the accuracy of measured modes is required.

3.3.2.c Modal Assurance Criterion (MAC)

The concept of Modal Assurance Criterion (MAC) and Modal Scale Factor (MSF) parallels the idea of Coherence Function and Frequency Response Function respectively [11]. Thus, through the modal assurance criterion, a causality relationship is established between two vectors. The reference or input vector $\{\phi\}_i$ is assumed to be composed of two parts, one part being completely correlated with the output vector $\{\phi\}_j$ (the vector to be correlated with) and the other completely

uncorrelated. In this manner the modal assurance criterion is defined in exactly the same way as the coherence function [11]. Thus,

$$MAC[\{\phi\}_i, \{\phi\}_j] = \frac{\left| \left(\sum_{m=1}^n \phi_{mi} \phi_{mj}^* \right) \right|^2}{\left(\sum_{m=1}^n \phi_{mi} \phi_{mi}^* \right) \left(\sum_{m=1}^n \phi_{mj} \phi_{mj}^* \right)} \quad (3.46)$$

$$MSF[\{\phi\}_i, \{\phi\}_j] = \frac{\{\phi\}_i^T \{\phi\}_j^*}{\{\phi\}_j^T \{\phi\}_j^*} \quad (3.47)$$

Thus, if the MAC value approaches unity, the modal scale factor computed is correct. It has to be noted that all the error has been lumped on one vector, and the reference vector is assumed to be error-free. The modal assurance criterion is a scalar constant relating two vectors and the modal scale factor is the corresponding linear scaling between the two vectors. The properties, advantages and limitations of the modal assurance criterion are discussed elaborately in Ref. [11].

Some applications of the Modal Assurance Criterion (MAC)

1. Experimental mode vectors originating from an undamped or proportionally damped system can be evaluated based on their orthogonal relationship. Deviations from orthogonality give clues as to the mode vectors that are in error.
2. Comparisons with analytical mode vectors can be made. If experimental mode vectors are assumed to be error-free, then the accuracy of the analytical mode vectors can be estimated, or vice versa. Currently, the modal assurance criterion is used almost universally for this purpose.

The modal assurance criterion has found several other uses apart from those mentioned above. It is necessary here to point out that the theory behind modal assurance criterion and modal scale factor (as is the theory behind coherence function and frequency response function) assumes linear and stationary systems.

Chapter 4

The Finite Element Model

An accurate analytical model is the goal of the analytical modeling process. The purpose here is to quantify errors in deriving an experimental modal model, a model that comprises of natural frequencies, damping ratios and mode shape of a linear system. The reasons for choosing a simple beam as the system were outlined in Chapter 3. There, the governing equations of motion for simple beams were developed. Two common beam theories, the Euler-Bernoulli and the Timoshenko beam theory, were employed to develop the equations of motion. To establish the modal properties of a beam, therefore, the differential eigenvalue problem has to be solved. The exact solutions to such differential eigenvalue problems are available for simple (classical) boundary conditions, when equations from either beam theory are used. However, such exact solutions may not be possible if

- non-classical boundary conditions exist
- the equations of motion contain variable coefficients

In such situations, only approximate methods of solution [54] can be employed. Again, these approximate methods may be difficult to implement, because of finding suitable approximation functions that satisfy the requirements demanded by these approximate methods. The finite element method, on the other hand, is very versatile in handling situations which are intractable by other methods. Here, the finite element method is chosen because of its capability to model and simulate various experimental test conditions, without unduly complicating the analytical modeling process. This chapter, therefore, deals exclusively with finite element procedures used in the analytical modeling of the test structure.

First, the governing differential equations of motion, from the Euler-Bernoulli and the Timoshenko theory, that will be used in the FE formulation are stated. Next, the finite element equations of motion are derived using the variational form, employing the Ritz approach. This is performed for a typical element, employing both the beam theories. The finite element models based on these two element types are implemented through a FORTRAN code, written and executed on the IBM 3090 mainframe computer system. Writing a code, rather than using a general purpose finite element code, is preferred for the following reasons:

- To avoid using the general purpose code as a “Black-box”, since the formulation of element equations and the associated assumptions are usually not available.
- To have more flexibility in modeling, and to have better control over the solution process.

The convergence characteristics of these two beam elements are presented for the case of a free-free beam in bending vibration. Also, the modeling techniques used to simulate experimental test conditions will be discussed. Subsequently, samples of typical analyses results are presented.

4.1 The Finite Element Equations

In Chapter 3, equations governing the transverse motion of beams were outlined. Their development assumed the presence of distributed axial force and were not restricted to small motions. Also, the equations were specialized to cases where the motions were small. The equations for the case in which the motions are small and in which axial forces are present are restated here for continuity. The finite element models used will be based on those equations.

4.1.1 The Governing Equations of Motion

Since the axial and bending deformations are uncoupled (due to the small motions assumption), only equations involving bending deformation need to be solved. Therefore, the equation describing axial motions is not stated here. Further, the rotatory inertia term from the Euler-Bernoulli beam equation will be dropped for simplicity. The equations of motion are stated below,

Euler-Bernoulli beam theory

$$\frac{\partial^2}{\partial x^2} \left[EI \frac{\partial^2 w}{\partial x^2} \right] - \frac{\partial}{\partial x} \left[P(x) \frac{\partial w}{\partial x} \right] + \rho A \frac{\partial^2 w}{\partial t^2} = f(x,t) \quad (4.1)$$

Timoshenko beam theory

$$\frac{\partial}{\partial x} \left[EI \frac{\partial \psi}{\partial x} \right] - KGA \left(\psi + \frac{\partial w}{\partial x} \right) + \rho I \frac{\partial^2 \psi}{\partial t^2} = 0 \quad (4.2a)$$

$$-\frac{\partial}{\partial x} \left[P \left(\frac{\partial w}{\partial x} \right) \right] - \frac{\partial}{\partial x} \left[KGA \left(\psi + \frac{\partial w}{\partial x} \right) \right] + \rho A \frac{\partial^2 w}{\partial t^2} = f(x,t) \quad (4.2b)$$

4.1.2 Formulation of the Euler-Bernoulli Beam Element

The governing equations of motion are now discretized using the Ritz variational approach [59]. This results in a weak form of the governing equations. That is, the differentiability and hence the continuity requirements on the approximation (interpolation) functions are weakened (lessened). First, the formulation of the Euler-Bernoulli beam element is presented, which will be followed by the formulation of the Timoshenko beam element¹².

Variational statement of the governing equations

The domain of the beam is discretized into a mesh of finite elements. Figure 4.2a shows a typical element in the mesh. Using the test function $v(x)$, the following variational statement of Eq. (4.1) could be made, for a typical element

$$\int_{\Omega^e} \left[v \left\{ \frac{\partial^2}{\partial x^2} \left(EI \frac{\partial^2 w}{\partial x^2} \right) - \frac{\partial}{\partial x} \left(P(x) \frac{\partial w}{\partial x} \right) + \rho A \frac{\partial^2 w}{\partial t^2} - f(x,t) \right\} \right] dx = 0 \quad (4.3)$$

Now, referring to Fig. 4.2a, we could define a local coordinate system such that the length of the element is L_e . Then, Eq. (4.3) could be written as,

¹² The formulation procedures used here follow those outlined in Refs. [53] and [59]

$$\int_0^{L_e} \left[v \left\{ \frac{\partial^2}{\partial x^2} \left(EI \frac{\partial^2 w}{\partial x^2} \right) - \frac{\partial}{\partial x} \left(P(x) \frac{\partial w}{\partial x} \right) + \rho A \frac{\partial^2 w}{\partial t^2} - f(x,t) \right\} \right] dx = 0 \quad (4.3a)$$

Integrating Eq. (4.3a) by parts, twice, we obtain

$$\int_0^{L_e} \left[EI \frac{\partial^2 v}{\partial x^2} \frac{\partial^2 w}{\partial x^2} + P \frac{\partial v}{\partial x} \frac{\partial w}{\partial x} + \rho A v \frac{\partial^2 w}{\partial t^2} - vf \right] dx -$$

$$v \left[\frac{\partial}{\partial x} \left(EI \frac{\partial^2 w}{\partial x^2} \right) - P \left(\frac{\partial w}{\partial x} \right) \right] \Big|_0^{L_e} - \left(-\frac{\partial v}{\partial x} \right) EI \left(\frac{\partial^2 w}{\partial x^2} \right) \Big|_0^{L_e} = 0 \quad (4.4)$$

Evaluating the limits for the terms outside the integral, we note

$$\int_0^{L_e} \left[EI \frac{\partial^2 v}{\partial x^2} \frac{\partial^2 w}{\partial x^2} + P \frac{\partial v}{\partial x} \frac{\partial w}{\partial x} + \rho A v \frac{\partial^2 w}{\partial t^2} - vf \right] dx -$$

$$Q_1 v(0) - Q_2 \left(-\frac{\partial v}{\partial x} \right) \Big|_0 - Q_3 v(L_e) - Q_4 \left(-\frac{\partial v}{\partial x} \right) \Big|_{L_e} = 0 \quad (4.4a)$$

where, the quantities Q_1 , Q_2 , Q_3 and Q_4 are given below (See Fig. 4.1a),

$$Q_1 = - \left[\frac{\partial}{\partial x} \left(EI \frac{\partial^2 w}{\partial x^2} \right) - P \left(\frac{\partial w}{\partial x} \right) \right]_{x=0} \quad Q_2 = - EI \left(\frac{\partial^2 w}{\partial x^2} \right)_{x=0} \quad (4.5)$$

$$Q_3 = \left[\frac{\partial}{\partial x} \left(EI \frac{\partial^2 w}{\partial x^2} \right) - P \left(\frac{\partial w}{\partial x} \right) \right]_{x=L_e} \quad Q_4 = EI \left(\frac{\partial^2 w}{\partial x^2} \right)_{x=L_e} \quad (4.6)$$

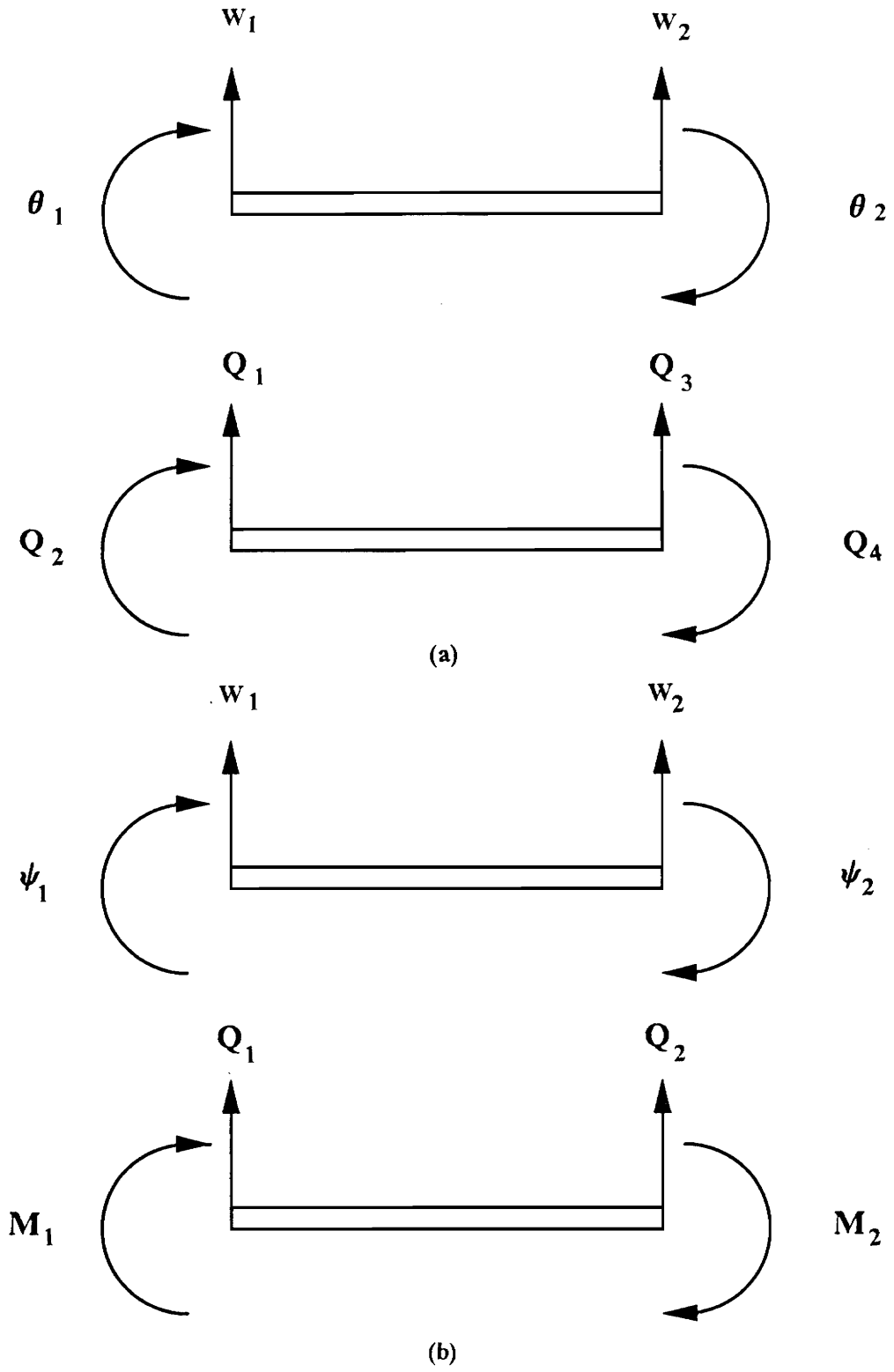


Figure 4.1. Degrees of freedom in (a) Euler-Bernoulli beam element (b) Timoshenko beam element

Interpolation

From the variational statement (weak form), we note that the continuity requirement on the interpolation function is that it needs to be at least differentiable thrice (Eqs. 4.5 and 4.6). We are interested in interpolating both the deflection and the slope degrees of freedom, at each node. Since there are two nodes (see Fig. 4.2a) in the element, the interpolation function should be at least a fourth-order polynomial. For convenience, $\frac{\partial w}{\partial x}$ will be denoted by $-\theta$ (negative θ). Observing the notation,

$$w(0) = w_1 \qquad w(L_e) = w_2 \qquad (4.7)$$

$$\theta(0) = \theta_1 \qquad \theta(L_e) = \theta_2 \qquad (4.8)$$

we note that the interpolation function has to satisfy the four parameters, namely, w_1 , θ_1 , w_2 and θ_2 . Therefore, the following fourth-order polynomial is used,

$$w(x) = a_0 + a_1x + a_2x^2 + a_3x^3 \qquad (4.9)$$

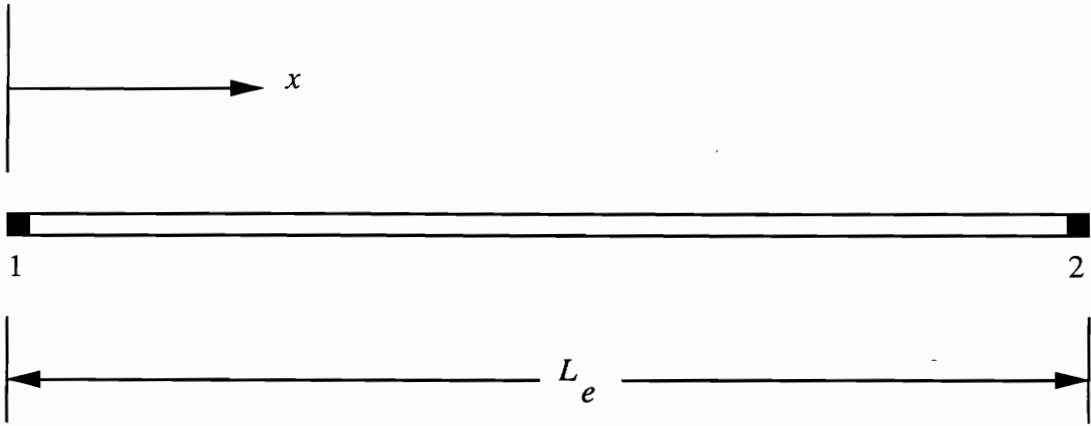
Now, the above equation can be expressed in terms of the four end-conditions, namely, w_1 , θ_1 , w_2 and θ_2 . Thus,

$$w(x) = w_1\phi_1(x) + \theta_1\phi_2(x) + w_2\phi_3(x) + \theta_2\phi_4(x) \qquad (4.10)$$

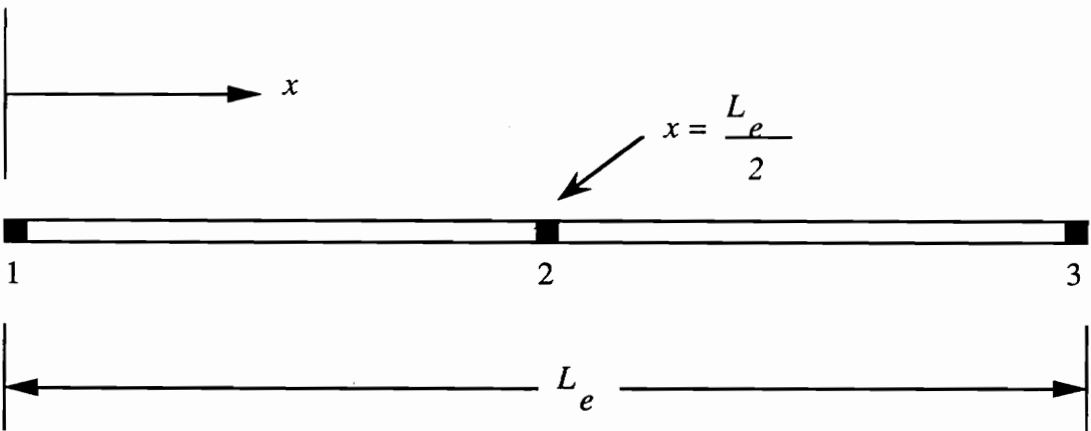
Using Eqs. (4.7 and 4.8) in Eq. (4.9), the parameters w_1 , θ_1 , w_2 and θ_2 are obtained (in terms of a_0 , a_1 , a_2 , a_3 and x). The ϕ_i 's are now solved by using these parameters in Eq. (4.10). These form the basis functions with which interpolation will be carried out. In terms of the element's local coordinates shown in Fig. 4.2a, they are as follows¹³

$$\phi_1(x) = 1 - 3\left(\frac{x}{L_e}\right)^2 + 2\left(\frac{x}{L_e}\right)^3 \qquad (4.11)$$

¹³ Reference [59] discusses the properties of these interpolation functions



(a)



(b)

Figure 4.2. A typical element in the mesh shown in local coordinates for (a) Euler-Bernoulli beam element (b) Timoshenko beam element

$$\phi_2(x) = -x \left(1 - \frac{x}{L_e}\right)^2 \quad (4.12)$$

$$\phi_3(x) = 3 \left(\frac{x}{L_e}\right)^2 - 2 \left(\frac{x}{L_e}\right)^3 \quad (4.13)$$

$$\phi_4(x) = -x \left[\left(\frac{x}{L_e}\right)^2 - \frac{x}{L_e} \right] \quad (4.14)$$

Equation (4.10) can now be conveniently written as,

$$w(x) = \sum_{j=1}^4 u_j \phi_j(x) \quad (4.15)$$

Finite element equations of motion

Using Eq. (4.15) in Eq. (4.4) and letting $v(x) = \phi_i$, the following equation results,

$$\sum_{j=1}^4 \left(\int_0^{L_e} \left[EI \frac{d^2 \phi_i}{d^2 x} \frac{d^2 \phi_j}{d^2 x} + P \frac{d \phi_i}{dx} \frac{d \phi_j}{dx} \right] dx \right) u_j +$$

$$\sum_{j=1}^4 \left(\int_0^{L_e} [\rho A \phi_i \phi_j] dx \right) \ddot{u}_j + \int_0^{L_e} \phi_j f dx - Q_i = 0 \quad (4.16)$$

More conveniently, we could write,

$$\sum_{j=1}^4 M_{ij}^e \ddot{u}_j + \sum_{j=1}^4 K_{ij}^e u_j - F_i^e = 0 \quad (4.16a)$$

which can now be put in matrix notation,

$$[M^e]\{\ddot{u}\} + [K^e]\{u\} = \{F^e\} \quad (4.16b)$$

The superscript e is used to denote element quantities, as opposed to global quantities. The Euler-Bernoulli beam element and its degrees of freedom are shown in Fig. 4.1a. The element stiffness matrix, $[K^e]$, mass matrix, $[M^e]$, and force vector, $\{F^e\}$, for the Euler-Bernoulli beam element are given below,

Element matrices for the Euler-Bernoulli beam element

$$K_{ij} = \int_{\Omega^e} \left[EI \frac{d^2 \phi_i}{dx^2} \frac{d^2 \phi_j}{dx^2} + P \frac{d\phi_i}{dx} \frac{d\phi_j}{dx} \right] dx \quad (4.17)$$

$$M_{ij} = \int_{\Omega^e} \rho A \phi_i \phi_j dx \quad (4.18)$$

$$\{u\} = \{w_1 \ \theta_1 \ w_2 \ \theta_2\}^T \quad (4.19)$$

$$\{F\} = \{F_1 \ F_2 \ F_3 \ F_4\}^T \quad (4.20)$$

$$F_i = - \int_{\Omega^e} \phi_i f(x,t) dx + Q_i \quad (4.21)$$

4.1.3 Formulation of the Timoshenko Beam Element

Again, the domain of the beam is discretized into a mesh of finite elements. Figure 4.2b shows a typical element in the mesh. Using the test functions $v_1(x)$ and $v_2(x)$, the following variational statement of Eqs. (4.2a and 4.2b) could be made, for a typical element.

Variational statement of the governing equations

$$\int_{\Omega^e} \left[v_1 \left\{ \frac{\partial}{\partial x} \left[EI \frac{\partial \psi}{\partial x} \right] - KGA \left(\psi + \frac{\partial w}{\partial x} \right) + \rho I \frac{\partial^2 \psi}{\partial t^2} \right\} \right] dx = 0 \quad (4.22a)$$

$$\int_{\Omega^e} \left[v_2 \left\{ -\frac{\partial}{\partial x} \left[P \left(\frac{\partial w}{\partial x} \right) \right] - \frac{\partial}{\partial x} \left[KGA \left(\psi + \frac{\partial w}{\partial x} \right) \right] + \rho A \frac{\partial^2 w}{\partial t^2} - f(x,t) \right\} \right] dx = 0 \quad (4.22b)$$

Again, we assume a local coordinate system for the element as shown in Fig. 4.2b, where L_e denotes the element length. Using this coordinate system, the variational statements in Eqs. (4.22a and 4.22b) can be rewritten as,

$$\int_0^{L_e} \left[v_1 \left\{ \frac{\partial}{\partial x} \left[EI \frac{\partial \psi}{\partial x} \right] - KGA \left(\psi + \frac{\partial w}{\partial x} \right) + \rho I \frac{\partial^2 \psi}{\partial t^2} \right\} \right] dx = 0 \quad (4.23a)$$

$$\int_0^{L_e} \left[v_2 \left\{ -\frac{\partial}{\partial x} \left[P \left(\frac{\partial w}{\partial x} \right) \right] - \frac{\partial}{\partial x} \left[KGA \left(\psi + \frac{\partial w}{\partial x} \right) \right] + \rho A \frac{\partial^2 w}{\partial t^2} - f(x,t) \right\} \right] dx = 0 \quad (4.23b)$$

Integrating by parts, once, the weak statements of Eqs. (4.23a and 4.23b) are obtained. Thus,

$$\int_0^{L_e} \left[EI \frac{\partial v_1}{\partial x} \frac{\partial \psi}{\partial x} + KGA v_1 \frac{\partial w}{\partial x} + KGA v_1 \psi + \rho I v_1 \frac{\partial^2 \psi}{\partial t^2} \right] dx - v_1 EI \frac{\partial \psi}{\partial x} \Big|_0^{L_e} = 0 \quad (4.24a)$$

$$\int_0^{L_e} \left[KGA \frac{\partial v_2}{\partial x} \frac{\partial w}{\partial x} + KGA \psi \frac{\partial v_2}{\partial x} + P \frac{\partial v_2}{\partial x} \frac{\partial w}{\partial x} + \rho A v_2 \frac{\partial^2 w}{\partial t^2} - v_2 f \right] dx - v_2 \left[KGA \left(\frac{\partial w}{\partial x} + \psi \right) + P \left(\frac{\partial w}{\partial x} \right) \right] \Big|_0^{L_e} = 0 \quad (4.24b)$$

Evaluating the limits for terms outside the integral in Eqs. (4.24a and 4.24b), we obtain

$$\int_0^{L_e} \left[EI \frac{\partial v_1}{\partial x} \frac{\partial \psi}{\partial x} + KGA v_1 \frac{\partial w}{\partial x} + KGA v_1 \psi + \rho I v_1 \frac{\partial^2 \psi}{\partial t^2} \right] dx - v_1(0) M_1 - v_1(L_e) M_2 = 0 \quad (4.25a)$$

$$\int_0^{L_e} \left[KGA \frac{\partial v_2}{\partial x} \frac{\partial w}{\partial x} + KGA\psi \frac{\partial v_2}{\partial x} + P \frac{\partial v_2}{\partial x} \frac{\partial w}{\partial x} + \rho Av_2 \frac{\partial^2 w}{\partial t^2} - v_2 f \right] dx -$$

$$v_2(0) Q_1 - v_2(L_e) Q_2 = 0 \quad (4.25b)$$

where, the quantities Q_1 , Q_2 , M_1 and M_2 are given below (See Fig. 4.1b),

$$Q_1 = - \left[KGA \left(\frac{dw}{dx} + \psi \right) + P \left(\frac{\partial w}{\partial x} \right) \right]_{x=0} \quad M_1 = - EI \left(\frac{d\psi}{dx} \right)_{x=0} \quad (4.26)$$

$$Q_2 = \left[KGA \left(\frac{dw}{dx} + \psi \right) + P \left(\frac{\partial w}{\partial x} \right) \right]_{x=L_e} \quad M_2 = EI \left(\frac{d\psi}{dx} \right)_{x=L_e} \quad (4.27)$$

Interpolation

Since there are two primary variables¹⁴, w and ψ , these have to be interpolated separately. From the weak statements of Eqs. (4.22a and 4.22b), we note that the interpolation functions chosen for w and ψ need to be continuous and at least once differentiable. This can be concluded from the boundary condition terms in Eqs. (4.26 and 4.27). These conditions are met by the linear Lagrange interpolation (shape) functions. However, these are only minimum requirements, and one could choose higher-order Lagrange interpolation functions. Also, interpolation functions of different orders could be used for w and ψ . Choosing the quadratic Lagrange interpolation functions for both the deflection and slope degrees of freedom, we use the following approximation functions in our formulation of the Timoshenko beam element,

¹⁴ See reference [59] for a definition of primary and secondary variables

$$w(x) = \sum_{j=1}^3 w_j \psi_j(x) \quad (4.28)$$

$$\psi(x) = \sum_{j=1}^3 s_j \psi_j(x) \quad (4.29)$$

Since a higher order interpolation function than that is required is used, additional degrees of freedom (one each for $w(x)$ and $\psi(x)$) have to be identified. We choose a center node as shown in Fig. 4.2b. The center node is similar in every respect to the other nodes, except that it is in the domain and the other two are at the boundary of the domain of the finite element. Using the same approach employed for finding the shape functions used in the Euler-Bernoulli beam element formulation, the following quadratic shape functions can be established,

$$\psi_1(x) = 1 - 3\left(\frac{x}{L_e}\right) + 2\left(\frac{x}{L_e}\right)^2 \quad (4.30)$$

$$\psi_2(x) = 4\left(\frac{x}{L_e}\right) - 4\left(\frac{x}{L_e}\right)^2 \quad (4.31)$$

$$\psi_3(x) = -\left(\frac{x}{L_e}\right) + 2\left(\frac{x}{L_e}\right)^2 \quad (4.32)$$

Using the approximation functions described by Eqs. (4.28 and 4.29) in the weak form of variational statements (Eqs. 4.25a and 4.25b), and letting $v_1(x) = \psi_i$ and $v_2(x) = \psi_i$, the following equations are obtained

Finite element equations of motion

$$\sum_{j=1}^3 \left(\int_0^{L_e} \left[EI \frac{\partial \psi_i}{\partial x} \frac{\partial \psi_j}{\partial x} + KGA \psi_i \psi_j \right] dx \right) s_j + \sum_{j=1}^3 \left(\int_0^{L_e} \left[KGA \psi_i \frac{\partial \psi_j}{\partial x} \right] dx \right) w_j + \sum_{j=1}^3 \left(\int_0^{L_e} \rho I \psi_i \psi_j dx \right) \ddot{s}_j - M_i = 0 \quad (4.33a)$$

$$\sum_{j=1}^3 \left(\int_0^{L_e} \left[KGA \frac{\partial \psi_i}{\partial x} \frac{\partial \psi_j}{\partial x} + P \frac{\partial \psi_i}{\partial x} \frac{\partial \psi_j}{\partial x} \right] dx \right) w_j + \sum_{j=1}^3 \left(\int_0^{L_e} \left[KGA \frac{\partial \psi_i}{\partial x} \psi_j \right] dx \right) s_j + \sum_{j=1}^3 \left(\int_0^{L_e} \rho A \psi_i \psi_j dx \right) \ddot{w}_j - \int_0^{L_e} \psi_i f dx - Q_i = 0 \quad (4.33b)$$

The above equations can be written as,

$$\sum_{j=1}^3 M^{11}_{ij} \ddot{s}_j + \sum_{j=1}^3 (K^{11}_{ij} s_j + K^{12}_{ij} w_j) - F^1_i = 0 \quad (4.34a)$$

$$\sum_{j=1}^3 M^{22}_{ij} \ddot{w}_j + \sum_{j=1}^3 (K^{21}_{ij} s_j + K^{22}_{ij} w_j) - F^2_i = 0 \quad (4.34b)$$

Therefore, the equations of motion of the element, in matrix notation can be compactly written as

$$[M^e]\{\ddot{u}\} + [K^e]\{u\} = \{F^e\} \quad (4.35)$$

Element matrices for the Timoshenko beam element

The element matrices for the Timoshenko beam element, based on the governing equations stated by Eqs. (4.2a and 4.2b), are shown below

$$[K^e] = \begin{bmatrix} [K^{11}] & [K^{12}] \\ [K^{21}] & [K^{22}] \end{bmatrix} \quad [M^e] = \begin{bmatrix} [M^{11}] & [M^{12}] \\ [M^{21}] & [M^{22}] \end{bmatrix} \quad (4.36)$$

The submatrices are given by :

$$K^{11}_{ij} = \int_{\Omega^e} \left[EI \frac{d\psi_i}{dx} \frac{d\psi_j}{dx} + KGA \psi_i \psi_j \right] dx \quad K^{12}_{ij} = \int_{\Omega^e} \left[KGA \psi_i \frac{d\psi_j}{dx} \right] dx \quad (4.37)$$

$$K^{21}_{ij} = \int_{\Omega^e} \left[KGA \frac{d\psi_i}{dx} \psi_j \right] dx \quad K^{22}_{ij} = \int_{\Omega^e} \left[KGA \frac{d\psi_i}{dx} \frac{d\psi_j}{dx} + P \frac{d\psi_i}{dx} \frac{d\psi_j}{dx} \right] dx \quad (4.38)$$

$$M^{11}_{ij} = \int_{\Omega^e} \rho I \psi_i \psi_j dx \quad M^{22}_{ij} = \int_{\Omega^e} \rho A \psi_i \psi_j dx \quad (4.39)$$

$$[M^{21}] = [M^{12}] = [0] \quad (4.40)$$

$$\{u\} = \begin{Bmatrix} \{s\} \\ \{w\} \end{Bmatrix} \quad \{F\} = \begin{Bmatrix} \{F^1\} \\ \{F^2\} \end{Bmatrix} \quad (4.41)$$

where,

$$F^1_i = M_i \qquad F^2_i = Q_i + \int_{\Omega^e} \psi_j f(x,t) dx \qquad (4.42)$$

4.2 Computer Implementation

The first step in the finite element method of solution is to discretize the physical domain into a mesh of finite elements. Then, using a suitable element type, the element matrices are evaluated. This involves the integration of each term of the finite element matrices, e.g., Eqs. (4.12 to 4.17). This can be accomplished in two ways. The entries in each element matrix can be evaluated symbolically, or, they can be computed numerically. For higher-order elements, especially in two and three dimensions, numerical integration is essential. Each element matrix, once computed, is assembled into the corresponding global matrix using geometric connectivity relations. Once the global matrices are completely assembled, the boundary/initial conditions are imposed. Now, the system of algebraic equations are solved by using a standard solution algorithm.

4.2.1 The Free Vibration Problem

The free vibrations or natural vibrations of a system is one in which the system oscillates freely without any external stimuli. In our case, the vibrations of a beam without any external forces acting. The global matrices in the finite element model comprise the equations (algebraic) of motion of the beam. Thus, the discretized equations of motion are given by,

$$[M]\{\ddot{U}\} + [K]\{U\} = \{Q\} \quad (4.43)$$

where, the variables in Eq. (4.43) denote global quantities. The free vibration problem can now be stated as,

$$[M]\{\ddot{U}\} + [K]\{U\} = \{0\} \quad (4.44)$$

assuming a harmonic solution of the type,

$$\{U\} = \{\phi\} \sin \omega t \quad (4.45)$$

the free vibration problem can be stated as,

$$\{[K] - \omega^2[M]\}\{\phi\} \sin \omega t = \{0\} \quad (4.46)$$

which implies,

$$\{[K] - \omega^2[M]\}\{\phi\} = \{0\} \quad (4.47)$$

and we have the following algebraic eigenvalue problem,

$$Det\{[K] - \omega^2[M]\} = 0 \quad (4.48)$$

the solution of the above matrix eigenvalue problem yields the natural frequencies ω_n and mode shape vectors $\{\phi\}_n$

4.2.2 Solution Methodology Used in This Work

The beams used in the modal tests in this work are very simple and therefore can be easily modeled using the finite element technique. Since the beams are prismatic and uniform, there will be no

errors due to discretization of the geometry. However, establishing the boundary conditions existing in the actual testing environment is not a simple task. Details of the modeling procedures used will be discussed subsequently in a separate Section. All the finite element models used in this work are generated by a computer code written in FORTRAN. The finite element models are generated and solved on the IBM 3090 mainframe computer system. In the next several paragraphs, the details of the computer implementation of the problem are discussed.

Input data to the program

The input data to the program are the material properties, geometric properties, inertia properties of the transducers (when used in the model), a value for the gravity load (when used in the model), number of elements in the mesh, coordinates of the nodes, connectivity matrix, nodes in which the transducers are located and the boundary conditions information.

Evaluation of element matrices

All computations are done using double precision arithmetic. The element matrices are evaluated numerically using the Gauss-Legendre quadrature. The number of points (weights) used are selected to be more than sufficient, to exactly evaluate the integrals. In case of the Timoshenko beam element, reduced integration¹⁵ is performed on terms involving the shear modulus G . This is done to maintain consistency in interpolation. Reference [4] details the theory behind reduced integration. Also the interpolation (shape) functions are transformed to natural coordinates to facilitate numerical integration. The mass matrices used are consistent mass matrices, stated by Eqs. (4.18 and 4.39), for the Euler-Bernoulli and Timoshenko beam elements respectively.

Assembly of element matrices and imposition of boundary conditions

¹⁵ Since the same interpolation function is used for both deflection and slope degrees of freedom, reduced integration becomes necessary. See Ref. [4].

The global matrices are stored in full mode. That is, the global matrices are not stored in the band-symmetric storage mode. The problems solved here are for the case of free-free vibrations of a beam, and therefore displacement boundary conditions need not be specified. Since modeling the gravity force and transducer inertias result in displacement- and acceleration-dependent forces (see the Section on modeling), these have to be specified when necessary. However, imposition of these boundary conditions result in the mere addition of certain inertia and stiffness terms to certain entries of the global mass and stiffness matrices, and can be accomplished easily.

Solution of the finite element models

All the finite element models are solved on the IBM 3090 mainframe computer. The International Mathematical Subroutines Library's (IMSL) Eigensystem subroutine DGVCSF is used to solve the final matrix eigenvalue problem. The DGVCSF subroutine takes as input the matrices $[K]$ and $[M]$, along with their dimensions, resulting from the eigenvalue problem $[K]\{\phi\} = \lambda[M]\{\phi\}$. Also, the matrices $[K]$ and $[M]$ have to be real and symmetric and have to be stored in full mode. Further, the matrix $[M]$ is required to be positive definite.

4.3 Modeling

Two important factors which need to be modeled are,

1. The inertias of the force and response transducers.
2. The gravity force which induces a body force axially along the beam, as a result of suspending the beam vertically.

Generally, these factors are ignored in the analytical modeling process, because of their assumed negligible influence on the structure's dynamic behavior.

4.3.1 Inertias of Transducers

The inertial effects, both translational and rotational, of the transducers are assumed to act at a point. Due to the dynamics of the beam the points of transduction experience a force and a moment. The amount of force equals the translational inertia times the acceleration of the point. Similarly the amount of moment equals the rotational inertia times the angular acceleration (of the beam) at the point. Denoting the node number in the finite element model by i , the external force and moment due to inertia-loading at the point in question can be written as,

$$F_i = m_i \ddot{w}_i$$

$$M_i = I_i \ddot{\theta}_i$$

where, F_i and M_i are the force and moment respectively, and \ddot{w}_i and $\ddot{\theta}_i$ the corresponding accelerations at node i . The quantities m_i and I_i denote the translational and rotational inertias respectively, of the transducer. Thus, the external loads F_i and M_i are applied at the points of transduction, along with the boundary conditions. Since these inertial loads contain the nodal accelerations as variables, they can be rearranged in the system of equations by grouping them with other inertia force terms. In fact, the quantities m_i and I_i simply add to the corresponding diagonal terms of the global mass matrix.

The masses of the both force and response transducers are obtained from the technical manuals supplied by the manufacturers. Since the transducers have well-defined geometry, calculation of the mass moment-of-inertias is straightforward. The mass moment-of-inertias of the transducers are calculated about the neutral axis of the beam. Though the transducers do not possess uniform

density, a uniform density assumption is made. The uniform density is computed by dividing the total mass by the total volume, for each transducer. For the case of the force transducer, only half the translational inertia is used, while modeling. This is due to the fact that the dynamic force being measured is at a point approximately at the centre of the force transducer. However, the entire geometry and mass of the transducer is used for rotational inertia calculations.

4.3.2 Body Force Due to Gravity Load

In all the modal tests performed, the beam is suspended vertically by means of a thin strand of nylon cords, which is attached to an elastic bungee cord at the other end. This induces a body force, due to gravity, that varies axially as shown in Fig. 4.3. The variation of this load can be denoted by,

$$P(x) = \rho AL \left(1 - \frac{x}{L}\right) \quad (4.49)$$

or, using the notation $P_0 = \rho AL$,

$$P(x) = P_0 \left(1 - \frac{x}{L}\right) \quad (4.49a)$$

Examining the stiffness coefficients in Eq. (4.17), we could conclude that an axial tensile load would increase the system stiffness, and hence its natural frequencies. However, the impact on mode shapes cannot be easily (intuitively) assessed.

Inclusion of the body force (axial force) in the modeling process requires the establishment of the associated boundary conditions. Particularly the force boundary conditions, since the displacement boundary conditions remain unaltered. Re-examining the derivation of the equations of motion of the beam (Chapter 3), we see that the effect of the axial force is to add to the shear force at any cross-section of the beam. Further, referring to the weak form of the variational statement in the

formulation of the Euler-Bernoulli beam element, Eq. (4.4), we obtain the boundary conditions. A discussion of these boundary conditions and alternative modeling procedures used to model the body force are discussed in the following Section.

Boundary conditions

Referring to Fig. 4.3, the boundary conditions that exist at the top end of the vertically suspended beam are not those which correspond to that of a free-free beam. Therefore, it is necessary to establish them to simulate the actual boundary conditions. Figure 4.3 illustrates two mathematical models that could be used to simulate the boundary conditions. If Eq. (4.1) is used, then the associated force boundary conditions are,

At $x = 0$,

$$\left[\frac{\partial}{\partial x} \left(EI \frac{\partial^2 w}{\partial^2 x} \right) - P_0 \left(\frac{\partial w}{\partial x} \right) \right] = 0 \quad EI \left(\frac{\partial^2 w}{\partial^2 x} \right) = 0 \quad (4.50)$$

and at $x = L$,

$$\frac{\partial}{\partial x} \left(EI \frac{\partial^2 w}{\partial^2 x} \right) = 0 \quad EI \left(\frac{\partial^2 w}{\partial^2 x} \right) = 0 \quad (4.51)$$

The second of equation (4.50) implies a force boundary condition,

$$\frac{\partial}{\partial x} \left(EI \frac{\partial^2 w}{\partial^2 x} \right) = P_0 \left(\frac{\partial w}{\partial x} \right) \quad (4.50a)$$

Inclusion of the force boundary condition will result in an unsymmetrical $[K]$ matrix, and hence an unsymmetrical eigenvalue problem. Figure 4.3c shows another model, in which the string and the beam are modeled as shown there. The following equation is used to model the string with finite elements.

$$\frac{\partial}{\partial x} \left[T(x) \frac{\partial w}{\partial x} \right] = \rho_s(x) \frac{\partial^2 w}{\partial t^2} \quad (4.52)$$

where $T(x)$ is the tension in the string (assumed to be constant) and $\rho_s(x)$ is the mass of the string per unit length. For a beam of weight P_0 , suspended vertically, the tension $T(x)$ in the string is given by,

$$T(x) = P(x) \Big|_{x=0} = P_0 \quad (4.53)$$

By using this model, the boundary conditions at $x = 0$ are accounted for, because of the force equilibrium and displacement compatibility at the interface, between the string and the beam element. Also, this model would be able to predict the rigid body modes of the suspended structure, in addition to being a more accurate model.

4.3.3 Sample Results and Discussion

The Ritz finite element model for the Euler-Bernoulli and Timoshenko beam theories were presented. The essential difference between the Euler-Bernoulli and the Timoshenko theories is that the latter accounts for shear deformation and rotatory inertia effects. The influence of shear deformation and rotatory inertia are significant for beams with smaller length-to-depth ratios. However, even for beams with larger length-to-depth ratios, shear deformation becomes significant for higher modes and rotatory inertia becomes significant at higher frequencies. Another important aspect was the inclusion of uniformly distributed axial forces in the equations of motion of a beam. This results in differential equations with a variable coefficient. The objective here is to have an accurate analytical model for validating experimental results.

The Euler-Bernoulli beam element uses a cubic Hermite interpolation. Thus the displacement function is a cubic function, as is the exact solution, for static problems, according to the Euler-Bernoulli theory. Therefore, for the case where the coefficients of the governing differential equation are constant, the element gives the exact solution for static problems (at nodes). The Timoshenko beam element uses the quadratic Lagrange interpolation function. Reduced quadrature is used on shear terms to maintain consistency of interpolation.

The material and geometric property values of the beam that will be used for sample analyses is given in Table 4.1. Table 4.2 shows the convergence characteristics of the Euler-Bernoulli beam element for a bar in bending vibration with free-free boundary conditions. The exact solution for the natural frequencies of the first ten flexible modes are shown, along with the results obtained using 5, 10, 20, 40 and 80 elements. As can be observed 8 elements per mode gives a fairly accurate solution. Table 4.3 shows corresponding results for the Timoshenko beam element. Cross comparison with results from Euler-Bernoulli element (Table 4.2) shows that the Timoshenko beam element converges at a slower rate. The influence of shear deformation and rotatory inertia can be seen for higher modes.

A simply supported beam with an axial compressive end-load is modeled, to validate the formulations for the case in which axial loads are present. A mesh of 80 Euler-Bernoulli beam elements is used with an axial load of 222.4 N. The exact solution¹⁶ from the linear Euler-Bernoulli theory is given below,

$$\omega_n = \left(\frac{n\pi}{L} \right)^2 \sqrt{\frac{EI}{\rho A}} \sqrt{1 + \left(\frac{L}{n\pi} \right)^2 \frac{P}{EI}} \quad (4.54)$$

$$\phi_n(x) = A \sin\left(\frac{n\pi}{L} \right)x \quad (4.55)$$

¹⁶ See Timoshenko, S.P., Young, D.H., Weaver, W., Jr., *Vibration Problems in Engineering*, Wiley, New York, 1974, 4th Ed.

where, ω_n denotes the natural frequency of the n th mode and $\phi_n(x)$ the corresponding mode shape. The results from exact solution and finite element analysis are shown in Table 4.4. As can be seen, the first mode is influenced the most. Also, the finite element model accurately predicts results obtained from exact solution. Next, the effect of gravity on the modal properties of a beam hung vertically is analyzed. The test configuration and the variation of the gravity load is shown in Fig. 4.3a. The finite element model with the associated boundary conditions are shown in Fig. 4.3b. As before 80 Euler-Bernoulli elements are used in the analysis. The natural frequencies of the first 10 modes are compared with the case in which no gravity load is present, in Table 4.5. The first two modes are also plotted in Fig. 4.4 and Fig. 4.5. The results suggest that the influence of gravity is very small and therefore negligible. As expected, the effect on the first mode is the most significant.

Table 4.1. Material and geometric property data for the beam used in sample analyses

Material/Geometric Property of the Beam	Value
Young's Modulus	1.9306×10^{11} Pascals
Mass density	7832.3 kg/m^3
Length	1.3970 m
Width	0.07696 m
Depth	0.0066 m

Table 4.2. Convergence characteristics of the Euler-Bernoulli beam element

Mode Number	5 Elements	10 Elements	20 Elements	40 Elements	80 Elements	Exact Solution
1	17.367	17.360	17.359	17.359	17.359	17.359
2	48.005	47.862	47.851	47.851	47.850	47.851
3	94.750	93.893	93.812	93.806	93.806	93.807
4	156.998	155.443	155.092	155.068	155.066	155.067
5	257.992	232.841	231.728	231.647	231.642	231.644
6	374.653	326.613	323.764	323.548	323.543	323.536
7	545.537	437.433	431.279	430.774	430.741	430.743
8	811.406	565.478	554.389	553.335	553.265	553.265
9	1416.90	704.008	693.264	691.242	691.106	691.103
10	1556.14	932.415	848.135	844.512	844.260	844.256

Table 4.3. Convergence characteristics of the Timoshenko beam element

Mode Number	5 Elements	10 Elements	20 Elements	40 Elements	80 Elements	120 Elements
1	17.385	17.359	17.358	17.358	17.357	17.357
2	48.375	47.876	47.842	47.839	47.839	47.839
3	97.521	94.031	93.780	93.764	93.763	93.763
4	172.471	156.117	155.026	154.953	154.948	154.948
5	265.651	235.134	231.636	231.395	231.379	231.378
6	434.304	332.880	323.711	323.063	323.021	323.019
7	708.859	452.357	431.435	429.933	429.834	429.829
8	1238.22	598.648	555.104	551.980	551.772	551.760
9	2676.54	788.528	695.156	689.185	688.782	688.760
10	22020.1	956.584	852.201	841.536	840.807	840.767

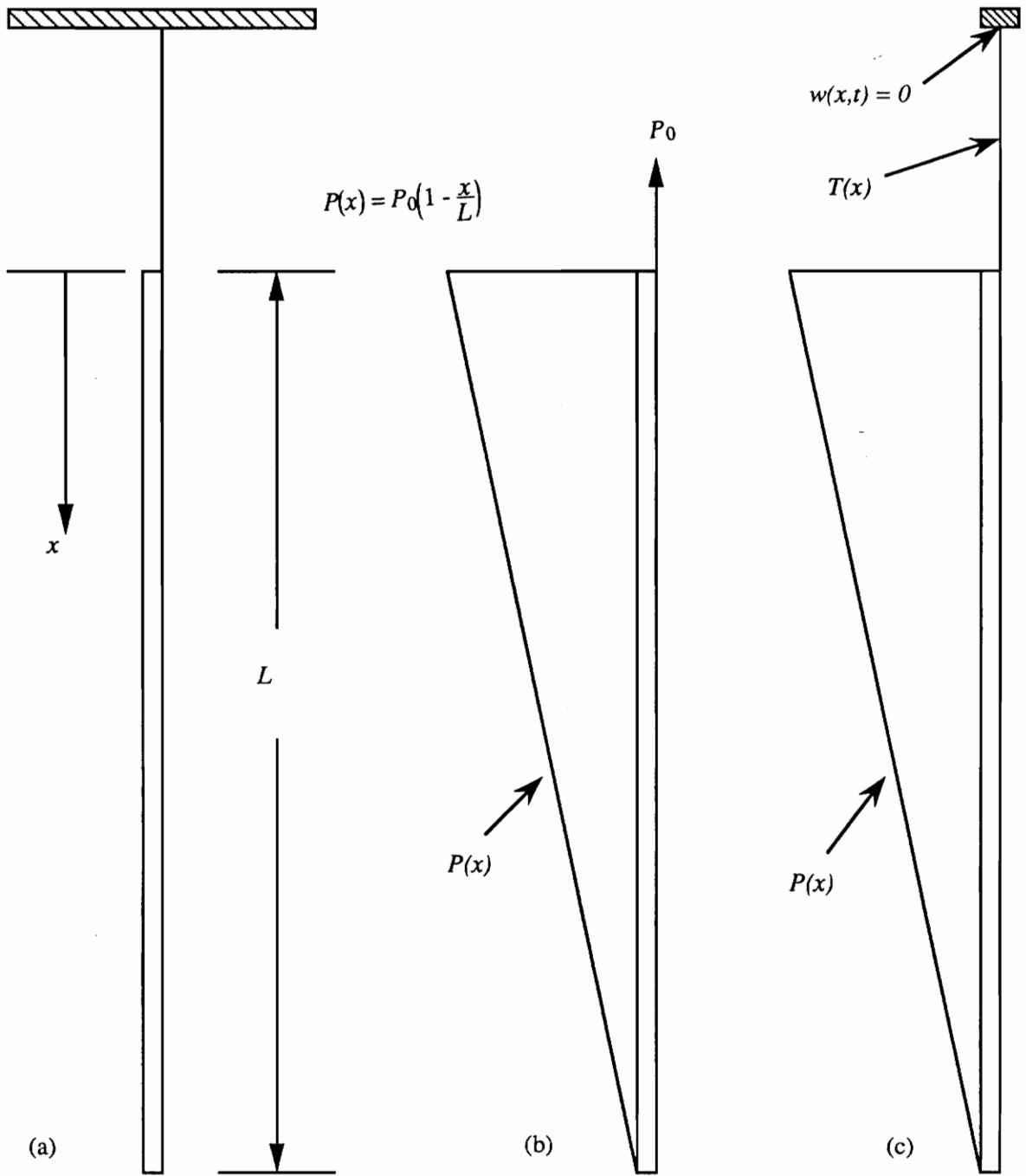


Figure 4.3. Test configuration and two mathematical models

Table 4.4. Influence of a constant compressive load on the natural frequencies of a simply supported beam

Mode Number	Exact Solution P = 0 N	Exact Solution P = 222.4 N	FEA 80 Euler-Bernoulli Elements P = 222.4 N
1	7.6577	8.1161	8.1161
2	30.631	31.099	31.099
3	68.919	69.389	69.389
4	122.52	122.99	122.99
5	191.44	191.91	191.91
6	275.68	276.15	276.15
7	375.22	375.70	375.70
8	490.09	490.56	490.56
9	620.27	620.74	620.74
10	765.76	766.24	766.24

Table 4.5. Influence of gravity force on the natural frequencies of the first ten flexible modes of a vertically suspended beam

Mode Number	Without Gravity Force	With Gravity Force
1	17.359	17.672
2	47.851	48.068
3	93.807	93.978
4	155.067	155.212
5	231.644	231.772
6	323.536	323.653
7	430.743	430.852
8	553.265	553.369
9	691.103	691.205
10	844.256	844.360

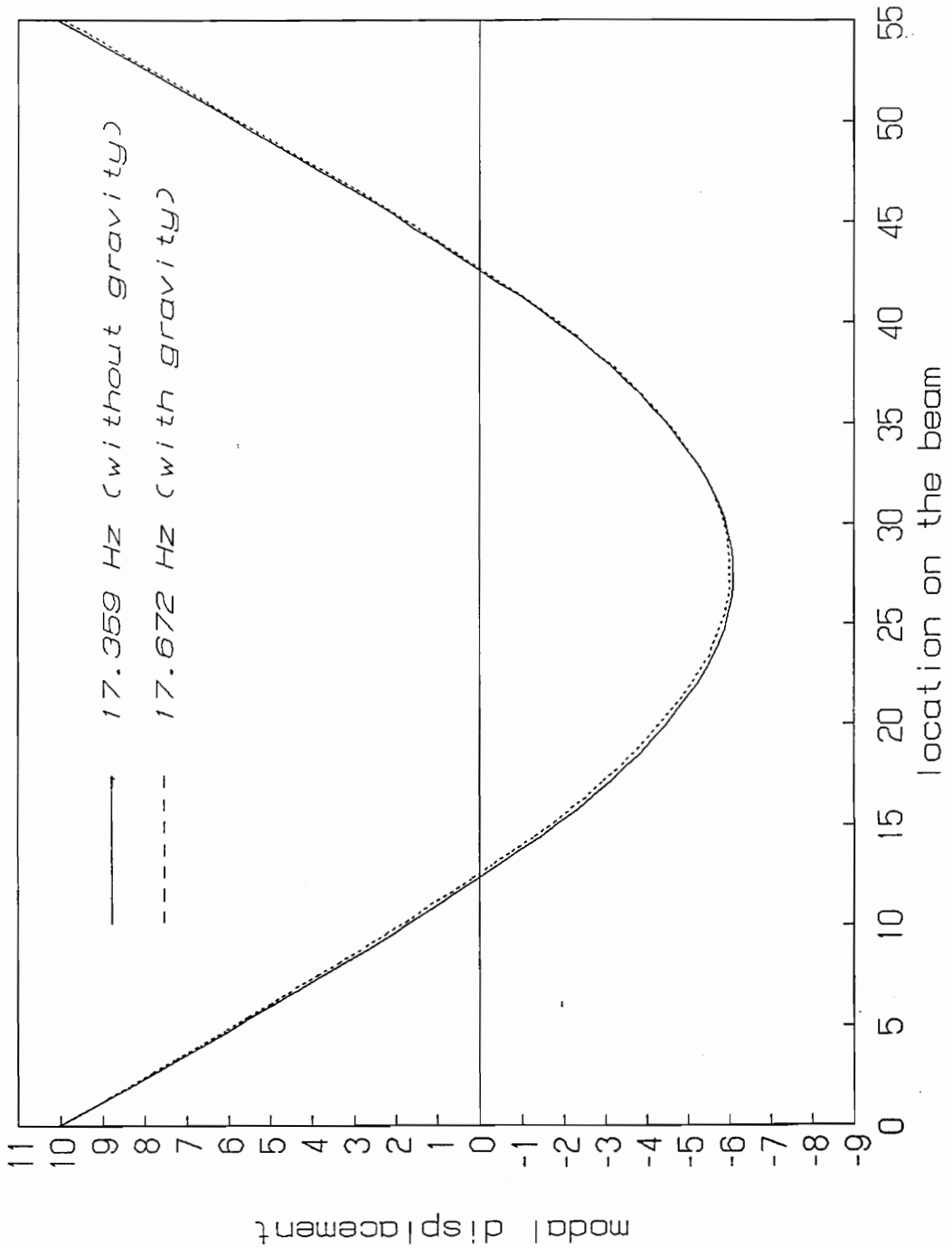


Figure 4.4 Influence of gravity force on the first mode of a vertically suspended beam

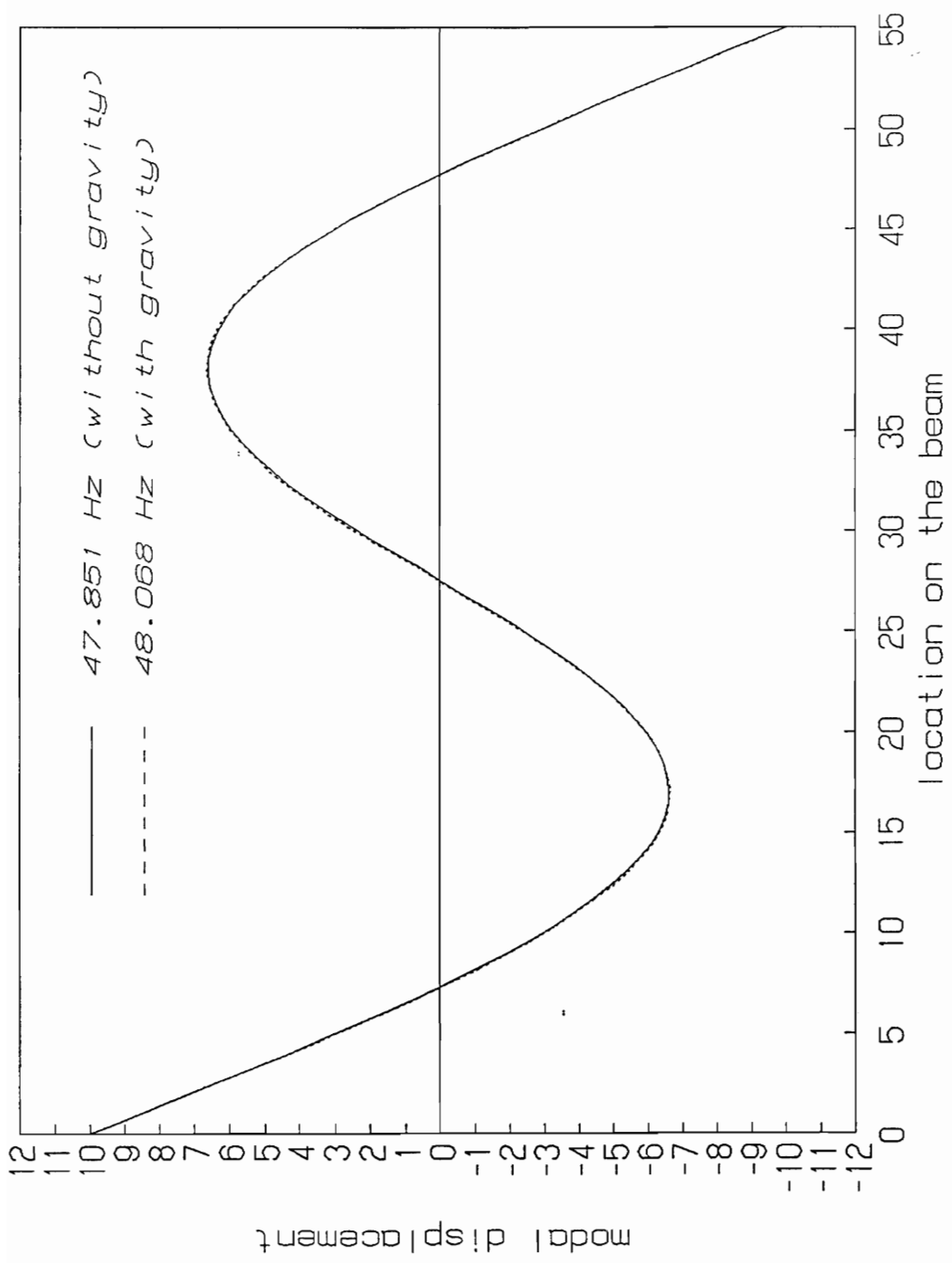


Figure 4.5 Influence of gravity force on the second mode of a vertically suspended beam

Chapter 5

The Experimental Model

Experimental modal analysis, today, has emerged as a very reliable tool in studying a structure's dynamics. The technology has evolved and matured significantly. However, owing to the diverse nature of the processes involved and due to the inexact nature of some techniques used, the resulting experimental modal model may be inaccurate. How accurate an experimental model is required depends on what the modal parameters will be used for subsequently. In any case there is a need to quantify errors in the experimental modal analysis process.

Errors in the final model can result from various sources during the EMA process, viz., transduction, supporting and exciting of test structure, signal processing, FRF estimation and modal parameter extraction. Choosing the right technique in each of the above processes is very vital to obtaining a realistic and accurate model. Also, the levels of error that could creep in and their quantification is essential, if meaningful reconciliation and validation of the experimental model is to be made. In this Chapter, some theoretical concepts used in experimental modal analysis work will be outlined first. Then, the sources and nature of errors that result from the EMA process will be reviewed. Finally, the modal tests performed in this work will be described in detail.

5.1 Theoretical Concepts in Modal Analysis

As with any activity in experimental mechanics, strong theoretical foundations form a rational basis for investigating physically observable phenomena. To start with, some salient features of single-degree-of-freedom (SDOF) systems are outlined. Insights gained from studying the behavior of SDOF systems are of fundamental importance in studying multi-degree-of-freedom (MDOF) systems. Though the concepts are quite general in nature, discussions are restricted to mechanical and structural systems. Further, the systems are assumed to be linear and time-invariant.

5.1.1 Single-Degree-of-Freedom Systems

In general, SDOF systems are those which could be characterized by a single second-order differential equation. The equation of motion of a simple mechanical system with spring, mass and a viscous-damper is given by,

$$m\ddot{x}(t) + c\dot{x}(t) + kx(t) = 0 \quad (5.1)$$

where, the variables have their usual meaning (see Appendix A). Using the following notation,

$$\omega_r = \sqrt{\frac{k}{m}} \quad \zeta = \frac{c}{2\sqrt{km}} \quad (5.1a)$$

we have the following solution,

$$x(t) = X e^{-\zeta\omega_r t} e^{i\omega_r\sqrt{1-\zeta^2} t} \quad (5.2)$$

As can be seen, the solution has a real and imaginary component to it. The following features are worth noting

1. In the absence of any damping the system behaves like a harmonic oscillator, vibrating with a frequency ω_r , called the natural frequency. The total energy, the sum of potential and kinetic energy, is conserved. Hence, the system is called a *conservative* system.
2. Damping renders the system *non-conservative*, since energy is dissipated from the system through the damping element. Also, for the force-free situation, the system oscillates with the damped natural frequency ω_{rd} , given by

$$\omega_{rd} = \omega_r \sqrt{1 - \zeta^2} \quad (5.2a)$$

Next, the forced-response problem, assuming harmonic excitation and response could be stated as,

$$m\ddot{x}(t) + c\dot{x}(t) + kx(t) = fe^{i\omega t} \quad (5.3)$$

which has the following solution,

$$x(t) = \frac{f(t)}{(k - \omega^2 m) + i(c\omega)} \quad (5.4)$$

or, using the parameters ω_r and ζ and normalizing $f(t)$ with respect to k , the system stiffness, Eq. (5.4) is written as,

$$\frac{x(t)}{f(t)} = H(\omega) = \frac{1}{\left[1 - \left(\frac{\omega}{\omega_r}\right)^2\right] + i(2\zeta \frac{\omega}{\omega_r})} \quad (5.5)$$

the quantity $H(\omega)$ is called the frequency response function (FRF) or the receptance of the system. The most important property of the FRF is

- It depends only on the physical parameters of the system and frequency.

It is an inherent property of the system and therefore independent of the excitation (assuming a linear system). The above statement implies that any type of excitation could be used to charac-

terize the FRF of a system. The choice of a pure harmonic excitation used above is merely a mathematical convenience. In Eq. (5.5), the receptance or FRF is a complex quantity. The magnitude and phase of the above FRF could be written as,

$$|H(\omega)| = \frac{1}{\sqrt{\left[1 - \left(\frac{\omega}{\omega_r}\right)^2\right]^2 + \left[2\zeta\left(\frac{\omega}{\omega_r}\right)\right]^2}} \quad (5.5a)$$

$$\phi(\omega) = \tan^{-1} \left[\frac{2\zeta\left(\frac{\omega}{\omega_r}\right)}{1 - \left(\frac{\omega}{\omega_r}\right)^2} \right] \quad (5.5b)$$

In Eq. (5.5) the FRF has been described using the ratio of displacement to force. Alternatively, either velocity or acceleration could be used, instead of displacement. Thus, noting

$$v(t) = \dot{x}(t) = i\omega X e^{i\omega t} \quad (5.6)$$

$$a(t) = \ddot{x}(t) = -\omega^2 X e^{i\omega t} \quad (5.7)$$

the following representations of the FRF could also be made,

$$V(\omega) = \frac{v(t)}{f(t)} = i\omega H(\omega) \quad (5.8)$$

$$A(\omega) = \frac{a(t)}{f(t)} = -\omega^2 H(\omega) \quad (5.9)$$

The quantity $V(\omega)$ is called the mobility and $A(\omega)$ inertance or accelerance.

5.1.2 Multiple-Degree-of-Freedom Systems

The theory behind vibration of SDOF systems serves as a very good foundation in the study of MDOF system behavior. However, in retrospect, it will be observed that the SDOF situation is only a special case of MDOF systems. In general, MDOF systems are those which cannot be described by a single second-order differential equation. Since the description of MDOF systems results in two or more simultaneous differential equations, the use of matrix algebra is inevitable. Rather than outlining the most general aspects of MDOF systems, features will be outlined sequentially on a case-by-case basis, starting from the simplest model [55]¹⁷.

5.1.2.a Undamped multiple-degree-of-freedom systems

For an undamped system with N degrees of freedom, the governing equations of motion could be written as,

$$[M]\{\ddot{x}\} + [K]\{x\} = \{f\} \quad (5.10)$$

In order to establish the natural vibration properties of the system the force-free vibration problem is solved first. As with the SDOF problem, a solution of the following type,

$$\{x(t)\} = \{X\}e^{i\omega t} \quad (5.11)$$

where, $\{X\}$ is a vector of constants, is assumed. The implications of the solution of the type above are,

1. the entire system is capable of vibrating at the same frequency.

¹⁷ Most part of Section 5.1.2 is taken from Ref. [55]

2. Since $\{X\}$ is a vector of constant amplitudes, the ratio between any two amplitudes remain constant at all times. Such a motion is termed synchronous [60].

Using solution denoted by Eq. (5.11) in Eq. (5.10) results in,

$$([K] - \omega^2[M])\{X\}e^{i\omega t} = \{0\} \quad (5.12)$$

Seeking a non-trivial solution to the above equation results in the following algebraic eigenvalue problem,

$$[K]\{X\} = \lambda[M]\{X\} \quad (5.13)$$

where, $\lambda = \omega^2$. The solution to the above eigenvalue problem yields a set of N eigenvalues λ_r and the corresponding eigenvectors $\{X\}_r$, ($r = 1, 2, \dots, N$). Thus, we have

$$[K]\{X\}_r = \omega_r^2[M]\{X\}_r \quad r = 1, 2, \dots, N \quad (5.14)$$

The square root of the eigenvalues yield the system natural frequencies. The corresponding eigenvectors are called the mode shapes or natural modes of the system. Representation of the system in terms of its natural frequencies, damping ratios and mode vectors is called a modal representation or a modal model.

Some important properties of the modal model

1. The individual mode vectors are not unique in that $\{X\}_r$ and $\alpha\{X\}_r$, where α is an arbitrary constant, represent the same mode vector. Only the ratios between individual elements of a mode vector are unique. Further, if the mode vectors are normalized according to a specific rule then the resulting modes are called normal modes. In the above sense mass-normalized mode vectors are those which are weighted with respect to the system mass matrix. Thus, the mass-normalized mode vectors $\{\phi\}_r$, are obtained as below,

$$\{\phi\}_r = \frac{\{X\}_r}{\{X\}_r^T [M] \{X\}_r} \quad r = 1, 2, \dots, N \quad (5.16)$$

The mass-normalized mode vectors are related to the stiffness matrix as follows,

$$\{\phi\}_r^T [K] \{\phi\}_r = \omega_r^2 \quad r = 1, 2, \dots, N \quad (5.17)$$

2. A very important property of the mode vectors of an undamped system is that they are all orthogonal to each other, when weighted with respect to the mass or stiffness matrix, (ie)

$$\{X\}_r^T [M] \{X\}_s = 0 \quad r \neq s \quad r, s = 1, 2, \dots, N \quad (5.18)$$

$$\{X\}_r^T [K] \{X\}_s = 0 \quad r \neq s \quad r, s = 1, 2, \dots, N \quad (5.19)$$

Response of undamped MDOF systems

Assuming harmonic excitation and response, the equations of motion could be written as,

$$([K] - \omega^2 [M]) \{X\} e^{i\omega t} = \{f\} e^{i\omega t} \quad (5.20)$$

which could be re-arranged to yield the relation,

$$[H(\omega)] \{f\} = \{x\} \quad (5.21)$$

where, $[H(\omega)]$ is the FRF matrix. Using the following relation,

$$[H(\omega)]^{-1} = ([K] - \omega^2 [M]) \quad (5.22)$$

and using the orthogonality properties of the mode vectors, the following equation results,

$$[H(\omega)] = [\Phi] \left(\text{Diag}[\omega_r^2 - \omega^2] \right) [\Phi]^T \quad (5.23)$$

where, $[\Phi]$ is the mass-normalized modal matrix, which has as its columns the individual mass-normalized mode vectors. An important property to be noted here is that the FRF matrix is symmetric. In other words,

$$H_{jk}(\omega) = \frac{x_j}{f_k} = H_{kj}(\omega) = \frac{x_k}{f_j} \quad (5.24)$$

A general element in the FRF matrix is given by,

$$H_{jk}(\omega) = \sum_{r=1}^N \frac{\phi_{jr} \phi_{kr}}{\omega_r^2 - \omega^2} \quad (5.25)$$

$$H_{jk}(\omega) = \sum_{r=1}^N Z_{kr} \phi_{jr} \quad (5.26)$$

where,

$$Z_{kr} = \frac{\phi_{kr}}{\omega_r^2 - \omega^2} \quad (5.26a)$$

the quantity Z_{kr} is called the modal participation factor of the r th mode, due to a forcing at k . From modal identification standpoint, the following representation is more useful,

$$H_{jk}(\omega) = \sum_{r=1}^N \frac{A_{jk}^r}{\omega_r^2 - \omega^2} \quad (5.27)$$

In the above Eq. (5.27), the quantity A_{jk}^r is called the modal constant. Oftentimes A_{jk}^r is referred to as the residue and the corresponding natural frequency the pole.

5.1.2.b Damped multiple-degree-of-freedom systems

The actual mechanism of damping in structural systems is quite complicated. However, models developed, though simple, have been adequate in most practical situations. Arbitrarily damped MDOF systems are not amenable to simple mathematical models. This is due to the fact that such arbitrary damping couples the differential equations of motion. Apart from rendering the modal properties complex ¹⁸, they also destroy the simple orthogonality relationships that characterized undamped systems. Therefore, simple models which uncouple the equations of motion are used where adequate. The following Sections briefly review the simple and some of the more involved damping models [55].

PROPORTIONALLY DAMPED SYSTEMS

Hysteresis (material damping) and viscous damping are the most common damping mechanisms found in structural and mechanical systems. Typically, material damping mechanisms are found in parallel with stiffness of structural systems and frictional damping mechanisms (viscous or Coloumbic) are found in parallel with mass or inertial elements. Consistent with the above observation, the following model for damping seems viable,

$$[C] = \alpha[M] + \beta[K] \quad (5.28)$$

where, α and β are constants that need to be evaluated. A similar assumption is usually made for structural damping. The above mathematical simplification enables decoupling the equations of motion, rendering the modal damping matrix diagonal. Thus,

$$[\Phi]^T[C][\Phi] = \alpha[I] + \beta(Diag[\omega_r^2]) \quad (5.29)$$

Since the undamped system's modal matrix diagonalizes the damping matrix, the undamped modes are indeed the eigenvectors for the proportionally damped system. The natural frequencies,

¹⁸ complex-valued

damping ratios and the FRF equations for proportionally damped systems with viscous and structural damping assumptions are stated below.

Viscous damping

$$\omega_{rd} = \omega_r \sqrt{1 - \zeta_r^2} \quad \zeta_r = \frac{\beta \omega_r}{2} + \frac{\alpha}{2\omega_r} \quad (5.30)$$

$$H_{jk}(\omega) = \sum_{r=1}^N \frac{\phi_{jr} \phi_{kr}}{\omega_r^2 - \omega^2 + i(2\zeta_r \omega_r \omega)} \quad (5.31)$$

Structural damping

$$\omega_{rd} = \omega_r^2(1 + \gamma_r) \quad \gamma_r = \beta + \frac{\alpha}{\omega_r^2} \quad (5.32)$$

$$H_{jk}(\omega) = \sum_{r=1}^N \frac{\phi_{jr} \phi_{kr}}{\omega_r^2 - \omega^2 + i(\gamma_r \omega_r^2)} \quad (5.33)$$

GENERALLY DAMPED SYSTEMS

Structural damping assumption

The equations of motion of a typical MDOF system with structural damping assumption are represented as,

$$[M]\{\ddot{x}\} + ([K] + i[H])\{x\} = \{f\} \quad (5.34)$$

Assumption, as usual, of a homogeneous solution which is harmonic results in the following complex eigenvalue problem,

$$([K] + i[H])\{x\} = \lambda[M]\{x\} \quad (5.35)$$

The solution to the above eigenvalue problem is a set of N complex eigenvalues and eigenvectors given by,

$$\lambda_r = \omega_r^2(1 + i\gamma_r) \quad \{X\}_r \quad (r = 1, 2, \dots, N) \quad (5.36)$$

where, ω_r is the natural frequency and γ_r is the damping loss-factor for the r th mode. Further, the mode vectors possess orthogonal properties exhibited by undamped and proportionally damped systems. Mass-normalizing the mode vectors and defining the modal matrix to be $[\Psi]$, the orthogonality relations could be stated as,

$$[\Psi]^T[M][\Psi] = [I] \quad (5.37)$$

$$[\Psi]^T([K] + i[H])[\Psi] = \text{Diag}[\lambda_r^2] \quad (5.38)$$

The FRF is similar to the one given by Eq. (5.25). However, the mode vectors for the general damping case are complex.

Viscous damping assumption

The case of viscous damping is more involved. Using state-space methods, the set of N second-order differential equations is reduced to a set of $2N$ first-order equations by defining a new coordinate system, in which the coordinates are both displacements and velocities. Such a vector is called a state-vector. Thus the new solution is sought in the state-space. Using this approach the solution to the free-vibration problem is sought by defining the following set of first-order equations,

$$[A]\{\dot{y}\} + [B]\{y\} = \{0\} \quad (5.39)$$

where,

$$y = \begin{Bmatrix} \{x\} \\ \{\dot{x}\} \end{Bmatrix} \quad [A] = \begin{bmatrix} [C] & [M] \\ [M] & [0] \end{bmatrix} \quad [B] = \begin{bmatrix} [K] & [0] \\ [0] & -[M] \end{bmatrix} \quad (5.40)$$

The above problem could be restated as a standard eigenvalue problem as shown below,

$$[B]\{y\} = \lambda_r[A]\{y\} \quad (5.41)$$

Since the matrices $[A]$ and $[B]$ are not symmetric the resulting eigenvalues and eigenvectors are complex, in general. Further, since they are real, the resulting eigenvalues and eigenvectors occur as complex conjugates, and are written as,

$$(s_r, \{\psi\}_r) \quad (r = 1, 2, \dots, N) \quad (5.42a)$$

$$(s_r^*, \{\psi^*\}_r) \quad (r = 1, 2, \dots, N) \quad (5.42b)$$

Also, the following orthogonal properties hold,

$$[\Psi]^T[A][\Psi] = \text{Diag}[a_r] \quad (5.43)$$

$$[\Psi]^T[B][\Psi] = \text{Diag}[b_r] \quad (5.44)$$

A typical element in the FRF matrix is given by,

$$H_{jk}(\omega) = \sum_{r=1}^N \left[\frac{\psi_{jr} \psi_{kr}}{a_r(i\omega - s_r)} + \frac{\psi_{jr}^* \psi_{kr}^*}{a_r^*(i\omega - s_r^*)} \right] \quad (5.45a)$$

where,

$$s_r = \omega_r \left(-\zeta_r + i\sqrt{1 - \zeta_r^2} \right) \quad (5.46)$$

If the mode vectors are mass-normalized with respect to $[A]$, then Eq. (5.45a) could be written as,

$$H_{jk}(\omega) = \sum_{r=1}^N \left[\frac{\psi_{jr} \psi_{kr}}{(i\omega - s_r)} + \frac{\psi_{jr}^* \psi_{kr}^*}{(i\omega - s_r^*)} \right] \quad (5.45b)$$

5.1.3 Alternative Approaches to Derive the FRF

In all previous cases the FRF was derived from the equations of motion assuming harmonic excitation and response. It was also noted that the FRF is an inherent property of the system, and therefore is independent of excitation. It should be observed here, however, that the FRF does not have any time variable in it. More importantly, it should be recognized that the FRF is defined in the frequency domain. Thus, other non-harmonic excitations should be expressed in the frequency domain, in order to facilitate usage of the FRF derived from harmonic excitation/response.

In the following sections, a more general definition of the frequency response function is made using the impulse response function (IRF). Also derivation of FRF from random vibrations are outlined briefly.

5.1.3.a FRF from arbitrary excitation

The frequency response function $H(\omega)$ of a constant-parameter linear system is given by the Fourier transform of the unit impulse response function $h(t)$ of the system [9]¹⁹,

$$H(\omega) = \int_{-\infty}^{\infty} h(t)e^{-i\omega t} dt \quad (5.47)$$

For a physically realizable linear time-invariant system, the output to any arbitrary input is given by the following convolution integral,

¹⁹ Some of the material in this Section is taken from Ref. [9]

$$y(t) = \int_0^{\infty} h(\tau) x(t - \tau) d\tau \quad (5.48)$$

Taking the Fourier transform of both sides of Eq. (5.48), convolution in the time-domain reduces to simple algebraic multiplication in the frequency-domain. Thus, we have

$$Y(\omega) = H(\omega) X(\omega) \quad (5.49a)$$

where, $X(\omega)$ and $Y(\omega)$ are the Fourier transforms of the input and output respectively. From the expression in Eq. (5.49a), we can deduce the frequency response function to be the simple ratio of Fourier transform of the output to the Fourier transform of the input.

$$H(\omega) = \frac{Y(\omega)}{X(\omega)} \quad (5.49b)$$

In general, the FRF is a complex-valued function, with both magnitude and phase associated with it. If the excitation is periodic, the Fourier series approach could be used to compute the FRF at the discrete frequencies, using Eq. (5.49b). If the excitation is transient, then, again Eq. (5.49b) can be used to compute the FRF. This can be achieved by computing the Fourier transform of the transient input and the corresponding response. This is possible because the Fourier transform assumes that the functions transformed have an infinite period. In practice, however, the discrete Fourier transform (DFT), which assumes that these transient signals are periodic in the observed time window, is used.

5.1.3.a FRF from random excitation

If the excitation is a random process then the above approach cannot be used. This is due to the fact that a random process is not Fourier transformable, because it violates Dirichelet's conditions [9]. However, an alternative approach is afforded. Using concepts from random process theory,

the following functions could be defined. An auto-correlation function of a certain random process $f(t)$ is defined as follows [9],

$$R_{ff}(\tau) = E[f(t)f(t + \tau)] \quad (5.50)$$

where, E denotes the expectation operation. Unlike $f(t)$, the quantity $R_{ff}(\tau)$ is Fourier transformable. The resulting quantity is called the power spectral or autospectral density function and is given by,

$$S_{ff}(\omega) = \frac{1}{2\pi} \int_{-\infty}^{\infty} R_{ff}(\tau) e^{i\omega\tau} d\tau \quad (5.51)$$

Thus $R_{ff}(\tau)$ and $S_{ff}(\omega)$ constitute a Fourier transform pair. Extending the above approach to two different random processes $x(t)$ and $f(t)$, the cross-correlation function and cross-spectral density are defined as follows,

$$R_{xf}(\tau) = E[x(t)f(t + \tau)] \quad (5.52)$$

$$S_{xf}(\omega) = \frac{1}{2\pi} \int_{-\infty}^{\infty} R_{xf}(\tau) e^{i\omega\tau} d\tau \quad (5.53)$$

Unlike the power spectral density function, the cross spectral density function is complex-valued. Also, the following conjugate property is satisfied by the cross-spectral density function,

$$S_{xf}(\omega) = S_{fx}^*(\omega) \quad (5.54)$$

Using the definition of impulse response,

$$x(t) = \int_0^{\infty} h(\alpha) f(t - \alpha) d\alpha \quad (5.55)$$

and using the following relations [9],

$$f(t)f(t + \tau) = \int_0^{\infty} \int_0^{\infty} h(\alpha)h(\beta)x(t - \beta)x(t + \tau - \alpha)d\alpha d\beta \quad (5.56)$$

$$x(t)f(t + \tau) = \int_0^{\infty} h(\alpha)x(t)x(t + \tau - \alpha)d\alpha \quad (5.57)$$

Taking expected values on both sides of Eqs. (5.56 and 5.57), result in,

$$R_{ff}(\tau) = \int_0^{\infty} \int_0^{\infty} h(\alpha)h(\beta)R_{xx}(\tau + \beta - \alpha)d\alpha d\beta \quad (5.58)$$

$$R_{xf}(\tau) = \int_0^{\infty} h(\alpha)R_{xx}(\tau - \alpha)d\alpha \quad (5.59)$$

The equations resulting from Fourier transforming Eqs. (5.58 and 5.59) could be simplified to yield the following relations,

$$S_{ff}(\omega) = |H(\omega)|^2 S_{xx}(\omega) \quad (5.60)$$

$$S_{xf}(\omega) = H(\omega)S_{xx}(\omega) \quad (5.61)$$

In a similar fashion, the following relation could also be established [9],

$$S_{ff}(\omega) = H(\omega)S_{fx}(\omega) \quad (5.62)$$

5.2 The Sources and Nature of Errors in the EMA Process

In the preceding Sections the analytical approach to modal analysis was outlined. This was done by identifying the physical parameters of the system and writing the equations of motion, using the assumption of small motions about an equilibrium position. This resulted in a linear description of the system in terms of an eigenvalue problem. The solution to the problem yielded the modal properties of the system. Subsequently, the frequency response of the system was defined in terms of its modal properties. This is the standard analytical approach.

The experimental approach recognizes the fact that if the FRF be established experimentally, then, using an appropriate theoretical model (FRF equation) the modal properties could be extracted by curve-fitting the experimental data to the theoretical FRF equation. Indeed, this has been the standard experimental approach used most of the time [55].

A typical experimental modal test and analysis is begun by making what is called a modal survey. This is to establish the locations of measurements (force and response) which are most likely to yield the best modal description of the structure. In other words, to determine those locations on the structure which are necessary to completely identify all the modes in the desired frequency range. Usually a finite element analysis provides this information. Next, a method of exciting the structure is chosen (excitation type, single or multi-input/output, etc.). Then, the force and response measurements are processed suitably using digital signal-processing techniques. Then, using fast Fourier transform (FFT) techniques, the time-domain signals are transformed into frequency-domain data. These frequency-domain data are then used to compute the FRF using an appropriate estimator. This is followed by curve-fitting the FRF data using a suitable modal parameter estimation algorithm, to estimate the modal properties in the frequency range tested [55].

5.2.1 Transduction Methods and Test Configurations

The test configuration, in other words, the right physical supporting of the test structure is very important in a modal test. Transducers, shakers, etc., interact with the structure being tested and influence their behavior. For substructure analysis the structural components of the superstructure are tested with free-free boundary conditions simulated. In such situations the quality of the rigid-body modes are sensitive to the suspension system used, location of shakers, etc. If not planned out carefully, this could lead to significant errors in the final model [31].

Transducer calibration and validation is essential before using them. Transverse sensitivity of transducers is another important concern [17]. Proper alignment of transducers with respect to the direction of measurement will minimize such errors. Measurements from force transducers are typically contaminated with significant error in the regions of resonance [15]. Inertia-loading of the structure by transducer masses introduce several type of errors [13]. They shift natural frequencies, and render real modes of a structure complex [13]. Typically only rule-of-thumb approaches are used in evaluating the impact of the above-mentioned factors on the accuracy of the experimental model.

5.2.2 Signal Processing of Excitation and Response Measurements

Many aspects of signal processing techniques are inexact in nature. They involve a lot of assumptions and approximations, and deviations from these assumptions result in systematic errors. The sources and nature of such errors must be properly understood in order to quantify and reduce them [5].

The root of the problem lies in the fact that continuous signals have to be converted to digital signals in order to be processed. This results in discretization, both in the time-domain and the

frequency-domain. The resulting problems are quantization errors and aliasing errors in the frequency-domain. The state-of-the-art of present-day technology is capable of reducing these errors to a very low level. Quantization errors are reduced by using a very good dynamic range of the A/D²⁰ converter and aliasing errors are reduced by using high-quality anti-aliasing filters, and by using only those spectral data that is guaranteed to be "alias-free".

The crux of the signal processing problem is the limitation of the length of time record that can be sampled. For a given frequency range of analysis, this leads to two problems

- The resolution of spectral data in the frequency range of analysis, since the sample interval T limits the frequency spacing between spectral lines. Insufficient resolution of spectral data results in bias errors, and such errors could be significant at the lower end of the spectrum when performing a base-band analysis [9].
- The discrete Fourier transform (DFT) assumes that the time record is periodic in the time window in which the it is recorded. Violation of such an assumption leads to a phenomenon called leakage, in which the spectral representation of the corresponding time record reflects the frequency domain characteristics of the observed signal (assumed periodic), rather than the actual signal.

Typically, the solution to the resolution problem, if critical, is to use a band-selectable (zoom) analysis. Usually a trade-off is made between the resulting accuracy and additional time involved.

One solution to the leakage problem is to use sufficient time record lengths in which the excitation and response signals reduce to A/D converter noise-levels, as this would ensure that the signals are periodic in the time window. However, this would mean inordinate amount of time required, especially for lightly damped systems. Such an approach has been practically infeasible. Another solution to the leakage problem is to "window" the time record, ie., weighting certain time-

²⁰ Analog-to-Digital

functions, defined in the interval of the time record, to the time record, so as to enforce periodicity of the sample in the time window. Windowing does not eliminate the leakage problem but only alleviates it. The degree to which it reduces leakage error depends on both the time record and the window-function used [28].

5.2.2.a Implications of leakage and windowing on the quality of modal model

The most widely used window is the Hanning window or the cosine-squared window, which has a value of zero at the beginning and end of the time record. Other windows in use are the flat-top, uniform and exponential windows. The choice of a window-function is determined by the characteristics of the time record, from periodicity point of view, in the sample interval. The following implications are worth noting,

1. Windowing, though reducing leakage, still yields a biased estimate of the spectra. They shift and distort the spectra.
2. In situations where modes are closely spaced, the specific window function used on excitation and response measurements should be able to resolve the individual resonances in the FRF.
3. The modal property most vulnerable to ineffective leakage reduction is the system damping.

Finally, each window function has its characteristics which have to be properly understood before using them, e.g., the Hanning window has a smoothing effect in that it reduces amplitudes at resonances and increases them at anti-resonances. The exponential window adds artificial damping to the data [61].

5.2.3 FRF Estimation

In Section 5.1 the concept of FRF of linear time-invariant systems was outlined. Various methods of deriving FRFs were stated, using harmonic, periodic, transient and random excitations. The focus was on mechanical and structural systems. In practice, however, the ideal situation of measuring the “true” excitation and response signals does not exist. Furthermore, non-ideal behavior of systems (nonlinear as opposed linear), incomplete identification of the inputs and outputs of the system, when present in incommensurate amounts, give rise to what is collectively called noise. Hence, one can obtain only estimates of the FRF. The following section briefly reviews some of the more popular models (estimators) used in practice. These estimators were developed on the assumption that the excitation and response signals are random. However, these estimators are used with transient (deterministic) data as well, though the quantity coherence function, to be defined in the sequel, bears a different meaning when used with deterministic data [55].

5.2.3.a A General Input/Output Model of a Linear System

A general input/output model of a linear system with noise at both input and output measurements is shown schematically in Fig. 5.1. The quantities $f(t)$ and $x(t)$ are the true input and output of the system, $m(t)$ and $n(t)$ are the noise signals which do not pass through the system and are uncorrelated to each other and to the input and output signals. The quantities $\tilde{f}(t)$ and $\tilde{x}(t)$ are the measured input and output signals. Thus,

$$\tilde{f}(t) = f(t) + m(t) \quad (5.63)$$

$$\tilde{x}(t) = x(t) + n(t) \quad (5.64)$$

The quantities S_{xx} and S_{xf} in Eqs. (5.60 and 5.61) are called the two-sided auto- and cross-spectra respectively, of the time records $x(t)$ and $f(t)$. This is because they are the Fourier transforms of the

corresponding time records defined in the range $-\infty$ to $+\infty$. Since, in practice, we use time records starting at $t = 0$, the auto- and cross-spectra for records defined in the range 0 to $+\infty$ are called one-sided spectra. These one-sided spectra will be denoted here by G_{ff} and G_{xf} [9].

The H_1 Estimator

Using Eqs. (5.63 and 5.64), using the FRF derived for the case of random vibrations and Eqs. (5.60 and 5.61), the following relation for the FRF could be realized [9],

$$H_1(\omega) = \frac{G_{f\tilde{x}}}{G_{ff}} \quad (5.65)$$

$$H_1(\omega) = \frac{G_{fx}}{G_{ff} + G_{mm}} \quad (5.65a)$$

Thus, if noise in the input measurement is assumed to be zero ($G_{mm} = 0$)²¹, the H_1 estimator yields an unbiased estimate of the FRF.

The H_2 Estimator

Using Eq. (5.63) and Eqs. (5.64 and 5.62), the following relation for FRF derived from random vibration could be stated [34]

$$H_2(\omega) = \frac{G_{\tilde{x}\tilde{x}}}{G_{\tilde{x}f}} \quad (5.66)$$

$$H_2(\omega) = \frac{G_{\tilde{x}\tilde{x}} + G_{\tilde{n}\tilde{n}}}{G_{\tilde{x}\tilde{x}}} \quad (5.66a)$$

²¹ G_{mm} denotes the autospectra of the noise in the input measurement

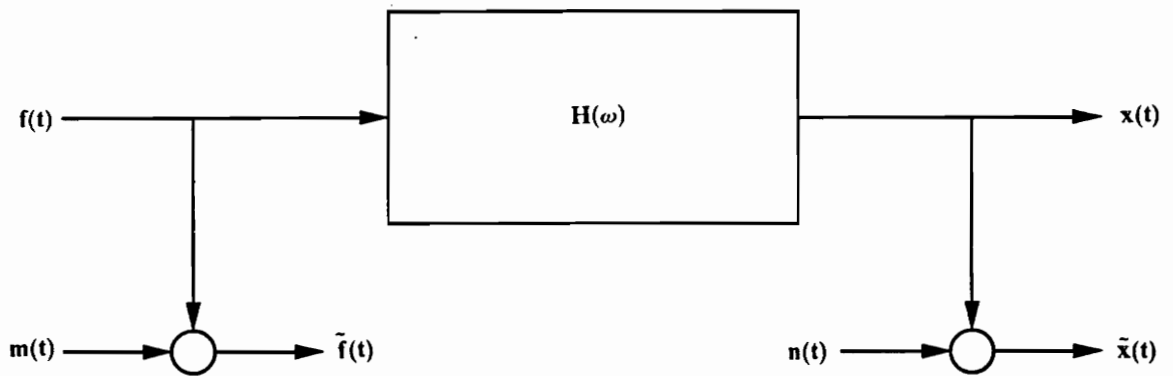


Figure 5.1. A general input/output model of a linear system

Thus, if noise in the output measurement is assumed to be zero ($G_{nn} = 0$), the H_2 estimator yields an unbiased estimate of the FRF.

The Coherence Function

Given two arbitrary signals $f(t)$ and $x(t)$, the coherence function provides a measure of linear relationship between $f(t)$ and $x(t)$. It is analogous to the correlation function coefficient and is defined in the frequency-domain. Per se it does not imply causality between $f(t)$ and $x(t)$. However, if an assumption of causality is made, then it gives a measure of the degree of causality between the signals $f(t)$ and $x(t)$. Recalling Eqs. (5.61 and 5.62), we could write (assuming noise-free measurements),

$$H_1(\omega) = \frac{G_{fx}}{G_{ff}} \quad (5.67)$$

$$H_2(\omega) = \frac{G_{xx}}{G_{xf}} \quad (5.68)$$

Dividing Eq. (5.67) by Eq. (5.68) yields the following equation,

$$\frac{H_1(\omega)}{H_2(\omega)} = \frac{G_{fx} G_{xf}}{G_{ff} G_{xx}} = \frac{|G_{fx}|^2}{G_{ff} G_{xx}} \quad (5.69a)$$

Ideally, in the absence of measurement noise, the quantities H_1 and H_2 are the same FRF. However, failing this, one is left with speculating possibilities as to why not. Generally speaking, violation of most assumptions made until now could lead to a non-unity condition of Eq. (5.69a). Some of the more obvious ones are:

- Nonlinear or time-invariant system.
- There are unidentified inputs to the system.

- The signals $f(t)$ and $x(t)$ are contaminated with noise.
- Leakage in estimating the spectra used in Eq. (5.69a)

Thus, Eq. (5.69a) could be used as a measure of linear causality between the signals $f(t)$ and $x(t)$. Thus, a new quantity $\gamma_{fx}^2(\omega)$ called the *coherence function* could be defined as [9],

$$\gamma_{fx}^2(\omega) = \frac{|G_{fx}|^2}{G_{ff} G_{xx}} \quad (5.69b)$$

If the autospectra G_{ff} and G_{xx} are non-zero and do not contain any delta functions, then the coherence function has values between 0 and 1, that is

$$0 \leq \gamma_{fx}^2(\omega) \leq 1 \quad (5.70)$$

The coherence function is the same for both H_1 and H_2 estimators. Since coherence function accounts for the effects of noise at both input and output, it yields a biased estimate.

THE H^c ESTIMATOR

This is a bivariate estimator which minimizes the error due to noise in both the input and the output signals. Here, an independent source signal $s(t)$ is used. The requirements on $s(t)$ are that it needs to be correlated to the input signal $f(t)$ but uncorrelated to both the noise sources $m(t)$ and $n(t)$. The H^c estimator [7,8] is given by,

$$H^c = \frac{G_{sx}}{G_{sf}} \quad (5.71)$$

This is an unbiased estimator, except that it has a bias error due to finite sample size. However, it cannot be used in the case of impact testing.

RANDOM AND BIAS ERRORS IN FRF ESTIMATION [9]

Random Errors

When using random signals to characterize a system's FRF, statistical reliability of the data need to be established. Two different situations exist here,

1. The case in which a deterministic signal is contaminated with noise.
2. Random signals which represent some random processes.

In the case of random signals, each record is supposed to contain statistically different information. Since only finite time records are sampled from such random signals, which are considered to be stationary and ergodic, the quantities of interest (autospectra, cross-spectra, etc.) can only be estimated. Thus, averaging is necessary for better estimates. However, only random errors could be reduced by such an averaging. In case of deterministic signals contaminated with noise, the noise portion of the signal is usually considered to be due experimental errors. Thus, averaging in this case helps reduce the magnitude of such errors.

Bias Errors

Bias errors in FRF estimation result, typically, due to the following factors,

1. Nonlinear/time-invariant systems
2. Bias errors in estimating autospectral and cross-spectral density functions. Typically, these are due to insufficient resolution in the spectra used. From Ref. [9], a simple relation between normalized bias error in the autospectral density function estimate, $\hat{G}_{xx}(\omega_r)$, system bandwidth, B_e , and resolution bandwidth, B_r , for a lightly damped SDOF system is given as,

$$\hat{G}_{xx}(\omega_r) \simeq -\frac{1}{3} \left(\frac{B_e}{B_r} \right)^2 \quad (5.72)$$

Also, use of window functions to reduce leakage introduces bias errors.

- Measurement noise at both the input and output lead to bias in the estimate if univariate FRF estimators like H_1 or H_2 are used. Using Eqs. (5.65 and 5.65a), the bias in the FRF estimate while using the H_1 estimator could be shown to be [9],

$$\varepsilon_b[\hat{H}_1(\omega)] = -\left[\frac{G_{mm}}{G_{xx} + G_{mm}}\right] \quad (5.73)$$

A similar result could be established for the H_2 estimator. Using unbiased (bivariate) estimators like the H^c estimator²² can eliminate this type of bias error.

- If other inputs that are correlated with the measured input are present, then the resulting estimate of the FRF will be biased. This can be corrected only by identifying such inputs and making use of the appropriate multiple-input/output model.
- Time-delay bias errors, which occur when the output lags the input in time.

5.2.4 Modal Parameter Estimation

Estimating the unknown coefficients of the appropriate FRF equation (theoretical model) by curve-fitting the experimentally obtained FRF data comprises the modal parameter estimation phase. This phase of the EMA process has grown tremendously over the years and the latest developments in numerical analysis procedures are employed, thereby increasing the accuracy, speed and robustness of the algorithms used. These advanced parameter estimation techniques are available both in time- and frequency-domain. While frequency-domain methods use the FRF, the time-domain methods use the impulse response function (IRF), obtained by performing an inverse Fourier transform of the FRF. Two important aspects have to be brought into perspective here. They are,

²² It was mentioned earlier about the bias error due to finite sample size when using the H^c estimator

1. Using the right theoretical model in a given situation. This implies using the appropriate FRF equation to represent the system behavior, and hence extracting the modal parameters. In this sense, even the best possible curve-fit may yield an inaccurate modal model, on account of having used an inappropriate theoretical model [55].
2. The second aspect to be considered is that curve-fitting removes noise present in the FRF data. However, the bias errors which could have arisen during previous stages of the EMA process are still present in the FRF data. If this situation exists, even the best possible curve-fit using the right theoretical model does not guarantee accurate modal parameters [55].

Generally, two types of modal analysis procedures are used. They are

- Single-degree-of-freedom (SDOF) analysis methods. Here, it is assumed that around the region of resonances the response is mostly dominated by the resonant mode in question. Thus, contributions due to other modes are assumed to be very small in that region, and are approximated by a constant. Such an assumption leads to a reasonably accurate representation for systems with well-separated modes [55].
- Multiple-degree-of-freedom (MDOF) analysis methods. Here, contributions to the total response due to other modes are also taken into account. Such a representation closely approximates the actual linear behavior of systems, and is indeed necessary for systems with closely spaced modes and/or systems which have heavily damped modes [55].

As might be anticipated, algorithms which use the SDOF assumption require less time than the ones using MDOF assumption, though the resulting model is less accurate.

Typically, modal tests are conducted in a specific frequency range (ω_a , ω_b). The FRF observed in this range is due to contribution of all the modes of the structure, including the ones present in the range (ω_a , ω_b). Thus, while extracting the modal properties from the FRF in the range (ω_a , ω_b),

the modes outside this range have to be accounted for. The following approximation is generally made [55],

$$H_{jk}(\omega) = -\frac{Y_{jk}}{\omega^2} + \sum_{r=m_1}^{m_2} \frac{A_{jk}^r}{\omega_r^2 - \omega^2 + i(\gamma_r \omega_r^2)} + Z_{jk} \quad (5.74)$$

where, Y_{jk} and Z_{jk} are the effect, in the range (ω_a, ω_b) , of modes below ω_a and above ω_b respectively. The quantity Y_{jk} is called the inertia restraint, and Z_{jk} residual flexibility. If the modal parameters are extracted using the above theoretical model, then the resulting model would substantially regenerate the experimentally observed FRF, in the range (ω_a, ω_b) .

5.2.4.a Single-degree-of-freedom analysis methods

In SDOF analysis methods each FRF of the structure is curve-fitted individually. The details of some of these techniques can be found in Ref. [47]. The shortcomings of SDOF techniques are,

- Closely spaced modes cannot be successfully extracted.
- Since modal contributions from other modes are assumed to be small, the modal parameters extracted are inaccurate.
- FRFs have to be analyzed individually. This could result in variation of modal properties from one FRF to another, resulting in an inconsistent model. In addition, some modes are tough, if not impossible, to identify.

The advantages are that SDOF analysis is simple to use and consumes very little time, factors which may sometimes offset potential benefits that MDOF methods provide.

5.2.4.b Multiple-degree-of-freedom analysis methods

MDOF techniques set out to improve on the limitations of SDOF methods. Two approaches exist,

1. In SDOF analysis, when analyzing a specific mode (say mode s), the contribution due to every other mode is assumed to be a constant. This restriction could be relaxed if a knowledge of modal properties of the remaining modes, which is usually available from a previous SDOF analysis, exists. The following equation illustrates the method [55],

$$E_{jk}(\omega) - \left[\sum_{r=m_1}^{m_2} \frac{A_{jk}^r}{\omega_r^2 - \omega^2 + i(\gamma_r \omega_r^2)} + Z_{jk} - \frac{Y_{jk}}{\omega^2} \right] = \frac{A_{jk}^s}{\omega_s^2 - \omega^2 + i(\gamma_s \omega_s^2)} \quad (5.75)$$

where, $E_{jk}(\omega)$ is the experimentally determined FRF. The quantities A_{jk}^s , ω_s and γ_s are estimated over a frequency range near the resonance of mode s , since the quantities on the left hand side of Eq. (5.75) are known. Thus, in effect, the right hand side quantity is curve-fitted with data which more precisely represents the response due to mode s .

2. The second approach is more general in nature and is the result of availability of sophisticated numerical analysis methods coupled with increased computational capabilities. Unlike the previous approach, all the modes in a given frequency range are addressed simultaneously. Again, defining $E_{jk}(\omega)$ to be the experimental FRF and $H_{jk}(\omega)$ the theoretical model, the error in fit, ε_i , for a given frequency is written as,

$$\varepsilon_i = E_{jk}(\omega_i) - H_{jk}(\omega_i) \quad (i = 1, 2, \dots, m) \quad (5.76)$$

the experimental data is known at m frequencies. Since ε_i is a complex quantity, the scalar is written as,

$$e_i = \sum_{i=1}^m \varepsilon_i \varepsilon_i^* = \sum_{i=1}^m |\varepsilon_i|^2 \quad (5.77)$$

Further, the quantity e_i could be weighted, if necessary. Thus, denoting E as the total squared and weighted error, we could write

$$E = \sum_{i=1}^m w_i e_i \quad (5.78)$$

The unknown quantities, which are the modal parameters, are estimated by minimizing them with respect to the quantity E . Thus,

$$\left(\frac{\partial E}{\partial \theta} \right) = 0 \quad \theta = \omega_1, \omega_2, \dots, \gamma_1, \gamma_2, \dots, A_{jk}^1, A_{jk}^2, \dots \quad (5.79)$$

The above procedure results in a set of equations which are linear in A_{jk} and nonlinear in ω , and γ . There are a host of methods which solve the above system, each differing in the type of solution methodology (linear least-squares as opposed to nonlinear estimation methods), complexity, numerical robustness, degree of user-participation, etc.

There are several factors which influence the choice of a parameter estimation technique. The following are some of them,

- Different regions of the FRF have different degrees of bias errors. Typically, the errors are high in the vicinity of resonances. Generally, these errors are due to using certain biased FRF estimators. Further, the resonance regions are more susceptible to leakage errors and deviations due to nonlinearities in the system. The linear least-squares algorithm is particularly attractive in that it is possible to weight the data as a function of frequency. The coherence function, then, could be used to determine the weighting. Reference [10] discusses one such procedure.

- The natural frequencies and damping ratios are global properties of a linear system. This fact is used in some, if not many, methods of solution. However, this is not strictly observed in reality. This could be due to inertia-loading of light-weight structures by transducer masses, measurement errors, nonlinearities, etc. In such cases, the algorithms used should be able to allow for small variations in global modal properties [47,49].
- Not all methods extract complex modes from FRF data. If the structure exhibits complex modes, using models with real mode assumptions can yield erroneous results.

In summary, the use of right parameter estimation procedure is very crucial to realizing an accurate model, however fine the quality of the experimentally acquired data be. Common to all the methods is the fact that they come with a set of basic assumptions in their formulation and solution methods. Using these methods without understanding the assumptions they are based on can result in an inaccurate or even erroneous model. As a result, different curve-fitting routines would generally yield different results. Also, the routines have to be used only on an ad hoc basis, so to speak, with a good idea of the data they are used on. Therefore, it is very important to quantify errors in the modal parameter estimation process. Only then could they be used with any confidence and the estimated parameters will have any meaningful quality.

5.3 Modal Tests Performed and Procedures Used

The goal of the tests conducted is to study and evaluate systematic errors which may appear due to reasons known *a priori*. Specifically, the contribution of the transduction process, viz., the effect of accelerometer inertias, shaker/force transducer-structure interaction, and modal parameter extraction process will be the focus of the tests and model-derivation process. A simple beam is

chosen as the test structure to be modeled. Three different modal tests are performed to assess the capability of experimental modal analysis techniques to produce an accurate modal model. The following sections detail each of these tests and the procedures used. For all the three tests the ZONIC²³ 6080 multi-channel FFT analyzer was used for acquiring data.

5.3.1 TEST 1

The test configuration used in TEST 1 is shown in Fig. 5.2. A uniform steel beam of rectangular cross-section with dimensions 1.39224 x 0.07696 x 0.00660 *meters* is used as the test structure. The beam is suspended by means of a thin bungee cord and a strand of thin nylon cords as shown in Fig. 5.2. The total length of the bungee cord and the strand of nylon cords is approximately equal to the length of the beam. An 18 *N* electrodynamic shaker is used for exciting the structure at the top of the beam as shown in Fig. 5.2. The shaker is suspended freely by the same method used to suspend the beam. A tabulation of details of the experimental set-up and test parameters is given in Table 5.1.

Force measurements are made with a piezo-electric transducer (22.5 mv/N) stud mounted to the beam. A thin stinger with wing-nuts served to connect the shaker to the transducer. All precautions were taken to minimize the effect of moment-restraint by the shaker-force transducer assembly. Response measurements are made at 23 equally spaced locations along the beam with an accelerometer capable of making simultaneous rotational and translational measurements. The accelerometer is affixed to the beam using a thin layer of bees wax. The validity of the transducer has been tested [62].

Burst random excitation is used through-out the test. Both force and response measurements are windowed using an exponential window [61]. The test is done in the range 0-1000 Hz. Low-pass

²³ Zonic Corporation, Milford, Ohio

anti-aliasing filters are used and only the first 400 lines of spectral data resulting from a 1024-point²⁴ FFT are used. The entire dynamic range of the A/D converter is used to reduce quantization errors.

Through-out the test the quality of the autospectra is monitored. Twenty averages are used to obtain the H^e type estimation for the FRFs. The quality of the FRFs were validated using the coherence function estimates. A total of 46 FRFs, 23 each for rotational and translational measurements were acquired.

5.3.2 TEST 2

The test configuration used in TEST 2 is shown in Fig. 5.3. Again, a uniform steel beam of rectangular cross-section with dimensions 1.5240 x 0.07615 x 0.00629 *meters* is used as the test structure. The beam is suspended by means of a thin bungee cord and a strand of thin nylon cords as shown in Fig. 5.3. The total length of the bungee cord and the strand of nylon cords is approximately equal to the length of the beam. This test differs from the previous test in that the beam is excited by means of an impact hammer and the response location is fixed at the bottom of the beam. A tabulation of details of the experimental set-up and test parameters is given in Table 5.2.

An impact hammer with a rubber tip is used to excite the beam. The tip is chosen on the basis of the quality of the force autospectra and the resulting FRF. Response measurement is made at the bottom-most location of the beam, while the forcing is made at 61 equally spaced locations along the beam.

The impulse force signal is windowed using a force window, while the response measurements are windowed using an exponential window. The impulse signal used for testing is conditioned in a

²⁴ A 1024-point FFT results in 512 lines of spectral data

manner so as to supply sufficient energy across the entire spectrum of interest. The autospectrum of the impulse signal was monitored carefully during the testing process. The test is done in the range 0-500 Hz. Low-pass anti-aliasing filters are used and only the first 400 lines of spectral data resulting from a 1024-point FFT are used. The entire dynamic range of the A/D converter is used to reduce quantization errors.

Through-out the test the quality of the autospectra is monitored. Ten averages are used to obtain the H_1 type estimation for the FRFs. The quality of the FRFs is validated using the coherence function estimates. A total of 61 FRFs from translational measurements are acquired.

5.3.3 TEST 3

This test was conceived from the standpoint of studying the influence of exciter location, when a shaker is used as an excitation device. The test configuration used in this test is shown in Fig. 5.4. The same uniform steel beam used in TEST 2 is used here (1.5240 x 0.07615 x 0.00629 *meters*). The beam is suspended by means of a thin strand of nylon cords that is connected to a thin bungee cord, as shown in Fig. 5.4. The test is performed twice, once with the shaker attached at the top of the beam and once with the shaker attached at the bottom. A tabulation of details of the experimental set-up and test parameters is given in Table 5.3.

Force measurements are made with a piezo-electric transducer (22.5 mv/N) stud mounted to the beam. A thin stinger with wing-nuts served to connect the shaker to the transducer. All precautions were taken to minimize the effect of moment-restraint by the shaker-force transducer assembly. Response measurements are made at 21 equally spaced locations along the beam with an accelerometer of minimal mass. The accelerometer is affixed to the beam using a thin layer of bees wax.

Burst random excitation is used through-out the test. Both force and response measurements are windowed using an exponential window [61]. The test is done in the range 0-125 Hz. Low-pass anti-aliasing filters are used and only the first 400 lines of spectral data resulting from a 1024-point FFT are used. The entire dynamic range of the A/D converter is used to reduce quantization errors.

The force autospectra are carefully monitored during the experiment. Ten averages are used in estimating the FRFs. The H_1 estimator is used in both the tests for FRF estimation.

5.3.4 Modal Parameter Estimation Procedures

Global frequency-domain parameter estimation methods are becoming very popular [49]. Particularly, techniques which fit orthogonal polynomials to FRF data using nonlinear estimation methods have gained currency in recent years [10,48]. Many such techniques in use typically have the following drawbacks,

1. They are numerically unstable, a problem inherent in nonlinear estimation procedures. As a result, extracting large number of modes has been a problem.
2. The FRFs derived through experimental methods have various degrees of bias and random error as a function of frequency. Hence, different regions of FRF data have different levels of statistical reliability. Many parameter estimation methods in current use do not weight data according to their quality, thus yielding less accurate models.
3. Some of the methods do not work very well with noisy FRF data, data with highly damped modes and data involving high modal densities.

The following Section briefly reviews a global frequency-domain parameter estimation algorithm which uses Forsythe orthogonal polynomials to fit FRF data [10]. The method [10] seeks to

overcome some of the drawbacks mentioned above with many algorithms. The key features of the method are listed below.

1. The weighting function is suitably chosen in the estimation process to avoid the numerical sensitivity of the nonlinear least-squares.
2. The use of Forsythe orthogonal polynomials enables the use of arbitrary weighting for each data point, in addition to allowing arbitrary spacing between data points. The implication of these features are:
 - Individual data points could be weighted according to their quality.
 - Since uniform data spacing is not required, data that are very poor at certain frequencies can be rejected. Also, base-band and zoom data can be combined effectively, thus allowing fitting of data in all frequency ranges simultaneously.
3. Many algorithms are over-refined in their capabilities in that they do not recognize the limitations in accuracy of the FRF data. This algorithm matches the variance of the data to the variance of the curve-fit at each frequency, so as to avoid over-modeling.

The algorithm [10] has many additional features generally found in most global frequency-domain methods. The fitting can be done in arbitrarily selected subranges. Out-of-band modes are accounted for by updating the data for each frequency range selected for fitting. Also, a large number of modes can be easily extracted. The capabilities of the algorithm have been demonstrated [10] on data with light damping, high modal densities and heavily damped data with complex modes.

Modal parameter estimation from data of TEST 1, TEST 2 and TEST 3

The curve-fitter described above [10] was used in the modal parameter estimation from the data of results from all the three tests. It is mentioned here in the passing that all the tests were performed in the base-band. The curve-fitting was done on individual FRFs for all the three tests. Therefore,

there were as many estimates of the global parameters (natural frequencies and damping ratios) as there were FRFs. This gave an idea as to the variability in estimating the modal parameters. This variability is assumed to be due to a combination of both measurement and curve-fitting errors. For the global parameters, the mean of all the individual estimates is used as the true value from EMA. Also, these true (mean) values are stated along with the associated variance. This allows the user to quantitatively interpret the statistical quality of the fit.

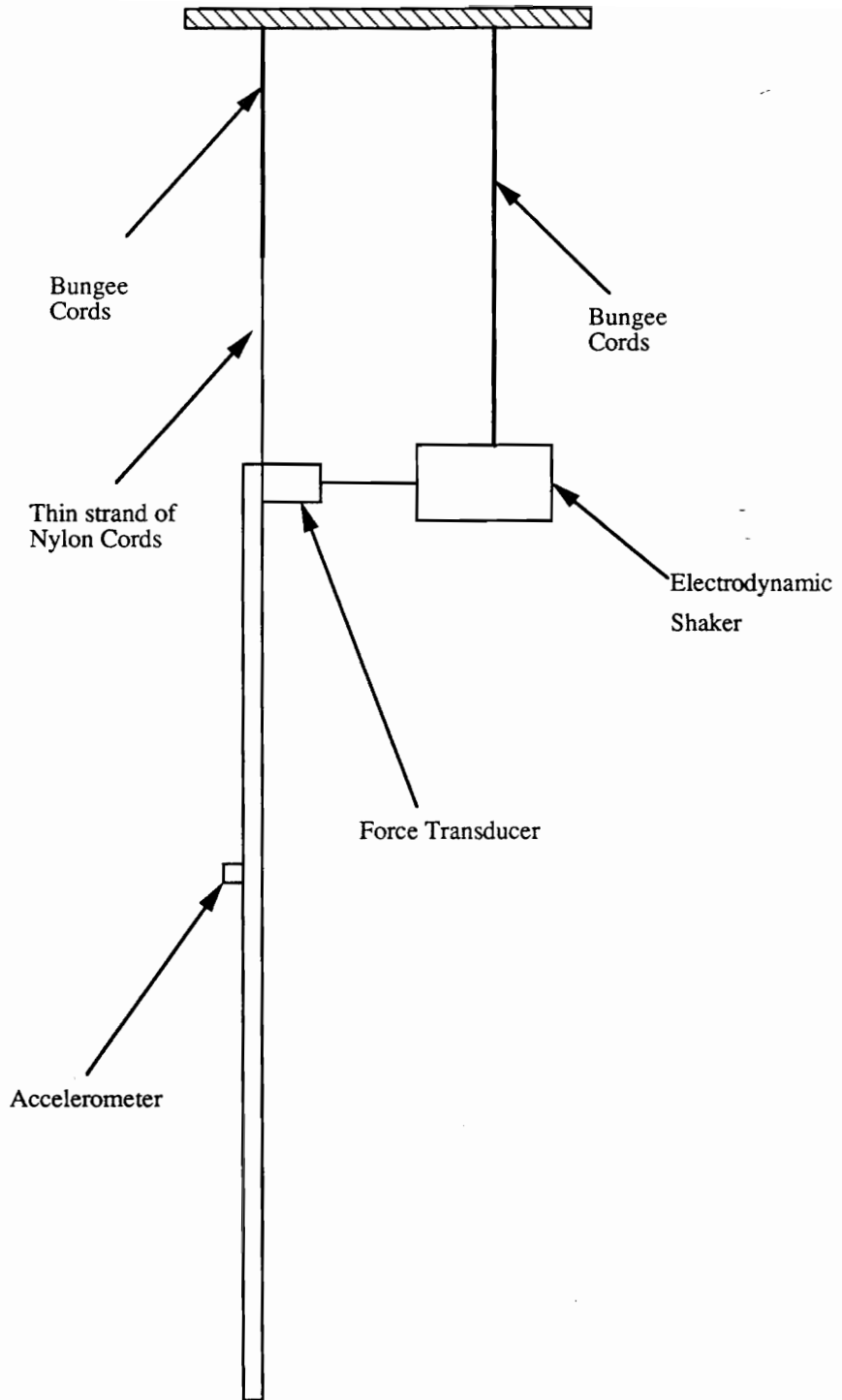


Figure 5.2. Test configuration used in TEST 1

Table 5.1. Tabulation of test parameters used in TEST 1

TEST PARAMETERS	REMARKS
Test Configuration	Vertically Hung (Shaker located at top)
Beam Dimensions	1.39224 x 0.07696 x 0.0066 m
Frequency Range	0 - 1000 Hz
Number of Locations / FRFs	23 equally spaced locations
Transducers	Force - 22.5 mv/N (0.025 kg mass) Response - Translational/Rotational (0.010 kg mass)
Excitation	Burst Random
Signal Processing	Excitation - Exponential window Response - Exponential window
FRF Estimation	H^c FRF Estimator Number of distinct averages = 20
Modal Parameter Extraction	Global frequency domain parameter estimation with variance weighting (FRFs fitted individually)

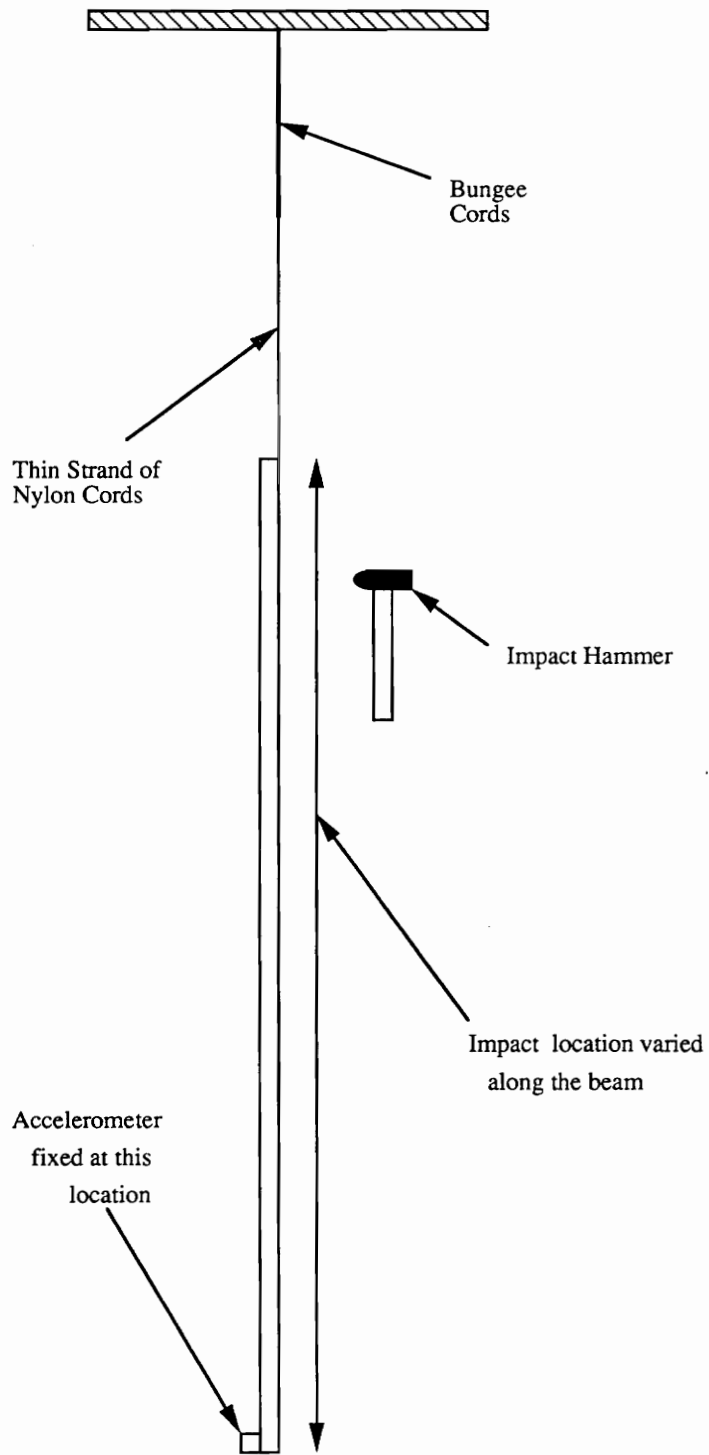


Figure 5.3. Test configuration used in TEST 2

Table 5.2. Tabulation of test parameters used in TEST 2

TEST PARAMETERS	REMARKS
Test Configuration	Vertically Hung (Accelerometer location fixed at the bottom of the beam)
Beam Dimensions	1.5240 x 0.07615 x 0.00629 m
Frequency Range	0 - 500 Hz
Number of Locations / FRFs	61 equally spaced locations
Transducers	Force - Impact Hammer Response - Translational/Rotational (0.010 kg mass)
Excitation	Impulse excitation using an impact hammer at 61 equally spaced locations
Signal Processing	Excitation - Force window Response - Exponential window
FRF Estimation	H ₁ FRF Estimator Number of distinct averages = 10
Modal Parameter Extraction	Global frequency domain parameter estimation with variance weighting (FRFs fitted individually)

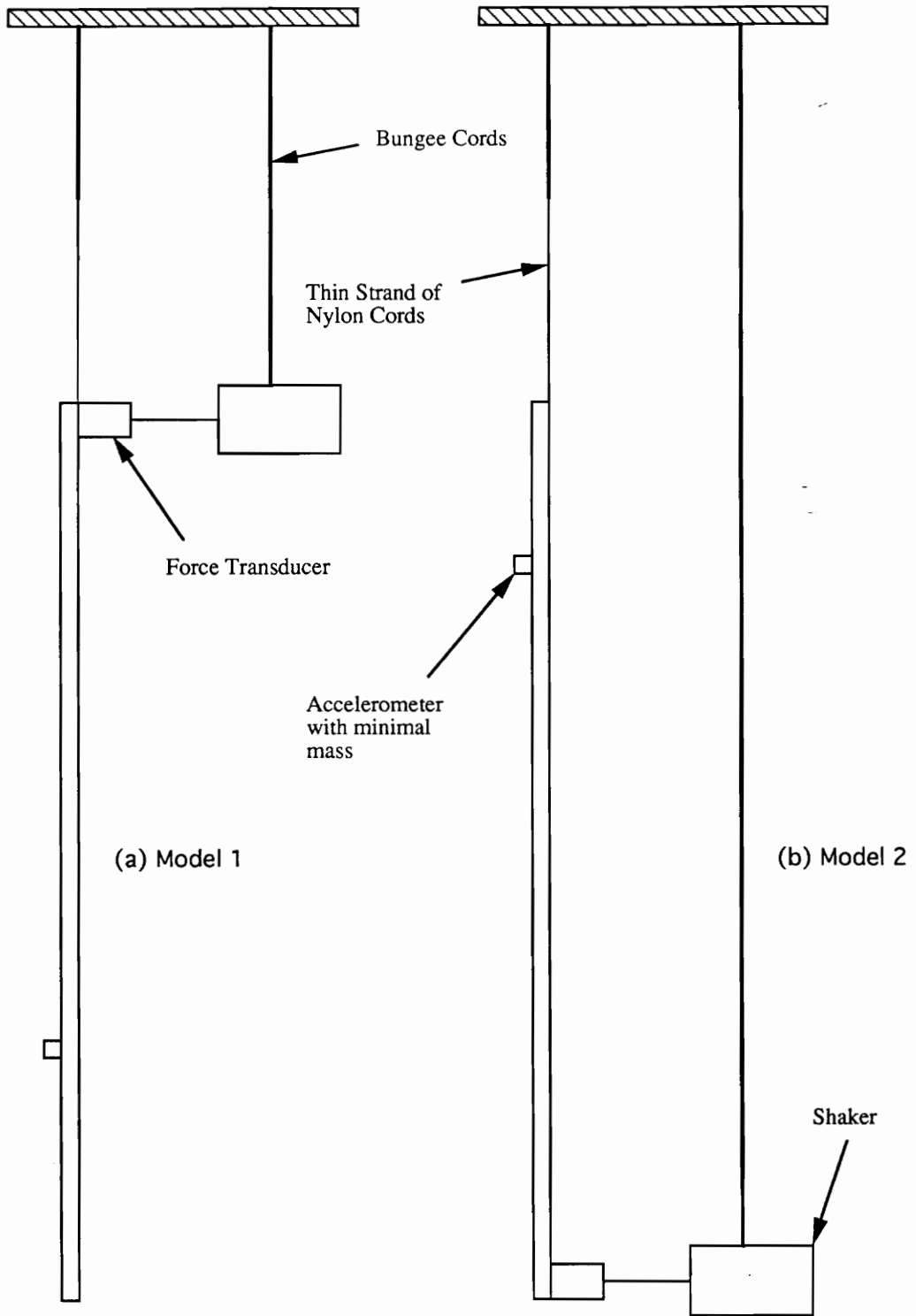


Figure 5.4. Test configuration used in TEST 3

Table 5.3. Tabulation of test parameters used in TEST 3

TEST PARAMETERS	REMARKS
Test Configuration	Vertically Hung Model 1 - Shaker located at top Model 2 - Shaker located at bottom
Beam Dimensions	1.5240 x 0.07615 x 0.00629 m
Frequency Range	0 - 125 Hz
Number of Locations / FRFs	21 equally spaced locations
Transducers	Force - 22.5 mv/N (0.025 kg mass) Response - Translational
Excitation	Burst Random
Signal Processing	Excitation - Exponential window Response - Exponential window
FRF Estimation	H ₁ FRF Estimator Number of distinct averages = 10
Modal Parameter Extraction	Global frequency domain parameter estimation with variance weighting (FRFs fitted individually)

Chapter 6

Results and Discussion

The results from experimental modal tests and analyses and their comparison with analytical (FEA) results from the standpoint of quantifying the errors in the experimental model will form the contents of this Chapter. The tests and procedures used in arriving at the final experimental modal models were outlined in detail in the previous Chapter. Also, the details of finite element modeling procedures have been dealt with in Chapter 3. As stated earlier, the contribution of the transduction and the modal parameter estimation process to the inaccuracy of the experimental modal model will be the focus and objective of the discussions to follow.

Comparisons between experimental and analytical (FEA) results are made for natural frequencies and mode vectors. Natural frequency comparisons are made with the aid of linear plots between experimental and FE natural frequencies. The accuracy of experimental natural frequencies is determined by using a linear regression model, using FE natural frequencies as the reference. The Modal Assurance Criterion (MAC), discussed in Chapter 3, will be used for comparing mode vectors. These are presented for each test conducted, followed by discussions on the accuracy of the modal parameters from EMA. For the experimental models resulting from TEST 1 and TEST 2, errors in estimating natural frequencies and modal displacements (imaginary component of the

residue estimate) are quantified. That is, errors are quantified for each spatial location. For the case of natural frequencies, percentage deviation from expected nominal values are stated, since the actual values are not known. In case of modal displacements, the results from the finite element model are assumed to be accurate, and therefore are used as the reference. Again, the errors are stated as a percentage deviation from reference values.

6.1 Results from Finite Element Analyses

In Chapter 3, the two most commonly used beam theories, the Euler-Bernoulli and the Timoshenko theory, were developed using a continuum mechanics approach. The Euler-Bernoulli theory, which results in a single differential equation of motion, ignores rotatory inertia and shear deformation effects in its development. The Timoshenko theory, which accounts for rotatory inertia and shear deformation, results in two simultaneous differential equations of motion. The Timoshenko theory, though more refined than Euler-Bernoulli theory, is used only when shear deformation/rotatory inertia effects are significant. The influence of shear deformation and rotatory inertia on the natural frequencies and mode shapes of uniform beams were stated in Chapter 3.

The development of the Ritz finite element model using the weak form of the governing equations of the above two beam theories was presented in Chapter 4. The Euler-Bernoulli beam element was developed using the Hermite cubic interpolation function, while the Timoshenko beam element was developed using the quadratic Lagrange interpolation (deflection and slope variables are interpolated separately) functions. Since the same interpolation function (quadratic) is used for both deflection and slope degrees of freedom, reduced integration is used on terms involving the shear modulus, to maintain consistency in interpolation. The mass matrices used are consistent.

The performance of the two element types was demonstrated in Chapter 4. It was shown that the convergence characteristics of the Euler-Bernoulli element was much better than the Timoshenko element. This is because of the cubic interpolation used, as opposed to the quadratic interpolation used in the Timoshenko beam element. The values of material and geometric properties used in FE analyses are shown in Table 6.1. The dimensions of the two beams used in the modal tests are shown in Table 6.2. Results from FE analyses, using free-free boundary conditions, are shown for the first ten flexible modes in Table 6.2. These are shown for both the Euler-Bernoulli element and the Timoshenko element, along with the exact solution from Euler-Bernoulli theory. Based on the results from Table 6.2, shear deformation and rotatory inertia effects are not very significant for the beams used in this work (for the frequency range considered in the modal tests). For example, referring to the tenth mode for BEAM 1 in Table 6.2, the difference is only around 0.5%. Therefore, for correlation and comparison purposes with the experimental results, only the results from Euler-Bernoulli element will be used.

Table 6.1. Material and geometric property values used in FE analyses

Property	Value
Young's Modulus (E)	2.034×10^{11} Pascals
Poisson's Ratio	0.29
Shear Correction Factor (K)	5/6
Mass Density	7832.3×10^3 kg/m ³
<u>Accelerometer Inertias</u>	
Translational	0.01 kg
Rotational	1.0835×10^{-6} kg.m ²
* <u>Force-Transducer Inertias</u>	
Translational	0.025 kg
Rotational	3.9725×10^{-6} kg.m ²
* <u>Fixture-Nut Inertias</u>	
Translational	0.0038 kg
Rotational	2.0566×10^{-7} kg.m ²

* Used in TEST 1 and TEST 3

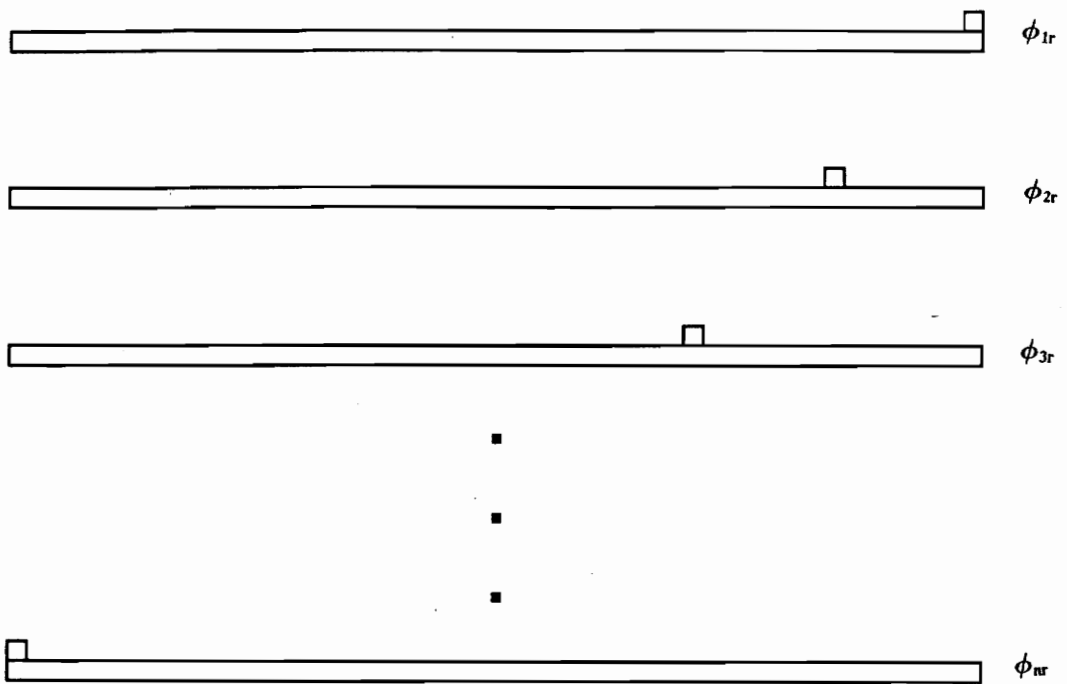
Table 6.2. FEA natural frequencies, of the first 10 flexible modes, for the two beams used in the modal tests

Mode Number	BEAM 1 (1.39224 x 0.07696 x 0.00660 m)			BEAM 2 (1.5240 x 0.07615 x 0.00629 m)		
	Euler - Bernoulli (Exact)	Euler - Bernoulli (91 Elem.)	Timoshenko (120 Quad. Elements)	Euler - Bernoulli (Exact)	Euler - Bernoulli (91 Elem.)	Timoshenko (120 Quad. Elements)
1	17.853	17.853	17.851	14.183	14.183	14.182
2	49.212	49.212	49.200	39.096	39.096	39.089
3	96.475	96.476	96.431	76.644	76.644	76.617
4	159.479	159.476	159.357	126.696	126.696	126.622
5	238.234	238.234	237.961	189.262	189.262	189.098
6	332.7399	332.741	332.208	264.342	264.342	264.021
7	442.997	442.999	442.005	351.934	351.934	351.366
8	569.005	569.009	567.452	452.040	452.040	451.104
9	710.764	710.772	708.345	564.695	564.696	563.202
10	868.274	868.288	864.670	689.791	689.796	687.621

6.1.1 Finite Element Models and Results - TEST 1

The test configuration used in TEST 1 and the testing procedures used were presented in detail in the previous Chapter (Fig. 5.2 and Table 5.1). The beam used in this test has dimensions of $1.39224 \times 0.07696 \times 0.00660$ metres. When including the transducer inertias in the FE model, both the force and response transducers are modeled, by including the translational and rotational inertias of each transducer. An important feature of TEST 1 is that the accelerometer, which is capable of making simultaneous rotational and translational measurements, is moved along the beam to facilitate response measurements. The force transducer, which is connected to the shaker through a thin stinger, is fixed at the top of the beam through-out the test. Response measurements are made at 23 locations along the beam. To simulate this in the FE model, an analysis is done for each response location, with the accelerometer mass modeled in the location in question. For each mode, the natural frequency and modal displacement, at the location of the transducer, is obtained. Therefore, the natural frequency and modal displacement from each location, for every mode, are essentially from a different system. The modeling procedure used to simulate the effect of the roving accelerometer is illustrated in Fig. 6.1.

The results from the analyses using 91 Euler-Bernoulli beam elements are shown in Table 6.3 and Table 6.4, for the first 10 flexible modes. They show the variation of natural frequency as the accelerometer mass is moved along the beam. Figure 6.2 shows the tenth mode plotted with reference to the corresponding mode obtained for a beam without any inertia-loading effect by the transducers. This is just to show the impact of inertia-loading on the mode which is affected the most.



n - response location number

r - mode number

ϕ - modal displacement vector

Figure 6.1. Figure illustrating the simulation of moving the accelerometer mass in the FE model

Table 6.3. Natural frequencies from FEA with inertia-loading effect from TEST 1 simulated (shown for modes 1 through 5 for all the 23 response locations)

Location	Mode Number				
	1	2	3	4	5
1	17.922	48.813	95.505	157.825	235.790
2	17.942	48.896	95.704	158.181	236.352
3	17.960	48.950	95.779	158.219	236.233
4	17.972	48.963	95.732	158.052	236.023
5	17.979	48.946	95.655	158.016	236.213
6	17.981	48.916	95.633	158.150	236.382
7	17.979	48.892	95.684	158.249	236.153
8	17.974	48.887	95.756	158.156	235.969
9	17.968	48.903	95.777	157.996	236.195
10	17.963	48.930	95.724	157.998	236.383
11	17.959	48.954	95.643	158.159	236.159
12	17.957	48.963	95.608	158.249	235.971
13	17.959	48.952	95.651	158.139	236.195
14	17.963	48.927	95.732	157.987	236.383
15	17.968	48.901	95.779	158.009	236.159
16	17.974	48.887	95.750	158.174	235.968
17	17.979	48.894	95.677	158.247	236.190
18	17.981	48.919	95.632	158.132	236.383
19	17.979	48.948	95.663	158.010	236.180
20	17.972	48.963	95.741	158.076	236.027
21	17.960	48.946	95.778	158.231	236.269
22	17.941	48.888	95.684	158.160	236.320
23	17.921	48.803	95.475	158.763	235.680

Table 6.4. Natural frequencies from FEA with inertia-loading effect from TEST 1 simulated (shown for modes 6 through 10 for all the 23 response locations)

Location	Mode number				
	6	7	8	9	10
1	329.403	438.673	563.603	704.192	860.440
2	330.174	439.632	564.700	705.355	861.583
3	329.816	439.025	563.958	704.715	861.336
4	329.778	439.400	564.751	705.531	861.515
5	330.172	439.521	564.099	704.399	861.061
6	329.901	438.896	564.170	705.538	861.719
7	329.618	439.423	564.714	704.605	860.889
8	330.043	439.485	563.833	705.168	861.876
9	330.093	438.897	564.619	705.080	860.750
10	329.641	439.470	564.312	704.680	861.989
11	329.846	439.439	563.989	705.497	860.660
12	330.182	438.899	564.784	704.412	862.049
13	329.790	439.513	563.908	705.567	860.629
14	329.673	439.391	564.435	704.553	862.052
15	330.131	438.908	564.515	705.242	860.657
16	329.990	439.552	564.867	705.003	861.996
17	329.608	439.339	564.766	704.746	860.743
18	329.959	438.919	564.056	705.448	861.886
19	330.151	439.580	564.217	704.418	860.873
20	329.741	439.322	564.692	705.584	861.719
21	329.871	439.072	563.956	704.626	861.149
22	330.152	439.639	564.756	705.478	861.784
23	329.231	438.423	564.257	703.736	859.857

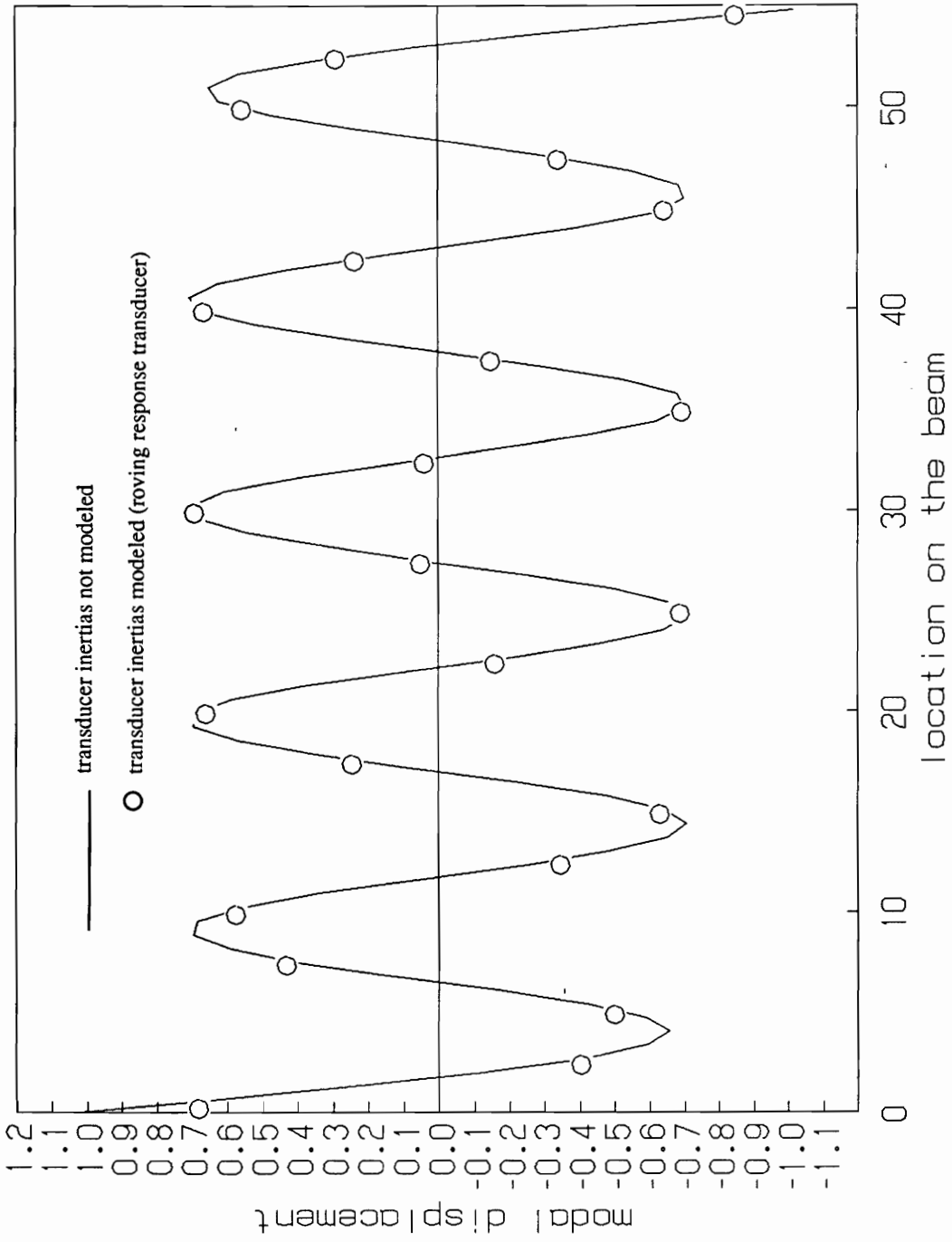


Figure 6.2 Tenth mode of BEAM 1 (TEST 1) showing the effect of inertia-loading by the roving accelerometer and fixed force transducer

6.1.2 Finite Element Models and Results - TEST 2

The details of this modal test are shown in Table 5.2 and Fig. 5.3. The test uses a beam different from the one used in TEST 1. The test is done using impulse excitation provided by an impact hammer. The response transducer (linear/angular accelerometer) is fixed at the bottom of the beam through-out the test. The beam is modeled using 62 Euler-Bernoulli beam elements. The natural frequency results from FE analyses for the various modeling conditions are shown in Table 6.5, for the first 8 flexible modes. Figure 6.3 shows the eighth mode (with transducer inertias modeled) with reference to the corresponding mode of a beam without any gravity and inertia effects modeled.

Table 6.5. Natural frequencies from FEA for various modeling conditions from TEST 2

Mode Number	Simple Model	Gravity Load Included	Accelerometer Inertias Included	Gravity and Accelerometer Inertias Included
1	14.183	14.533	14.136	14.486
2	39.096	39.340	38.972	39.216
3	76.644	76.836	76.409	76.602
4	126.629	126.860	126.322	126.486
5	189.262	189.409	188.723	188.869
6	264.343	264.476	263.614	263.748
7	351.938	352.062	350.999	351.123
8	452.049	452.167	450.880	450.998

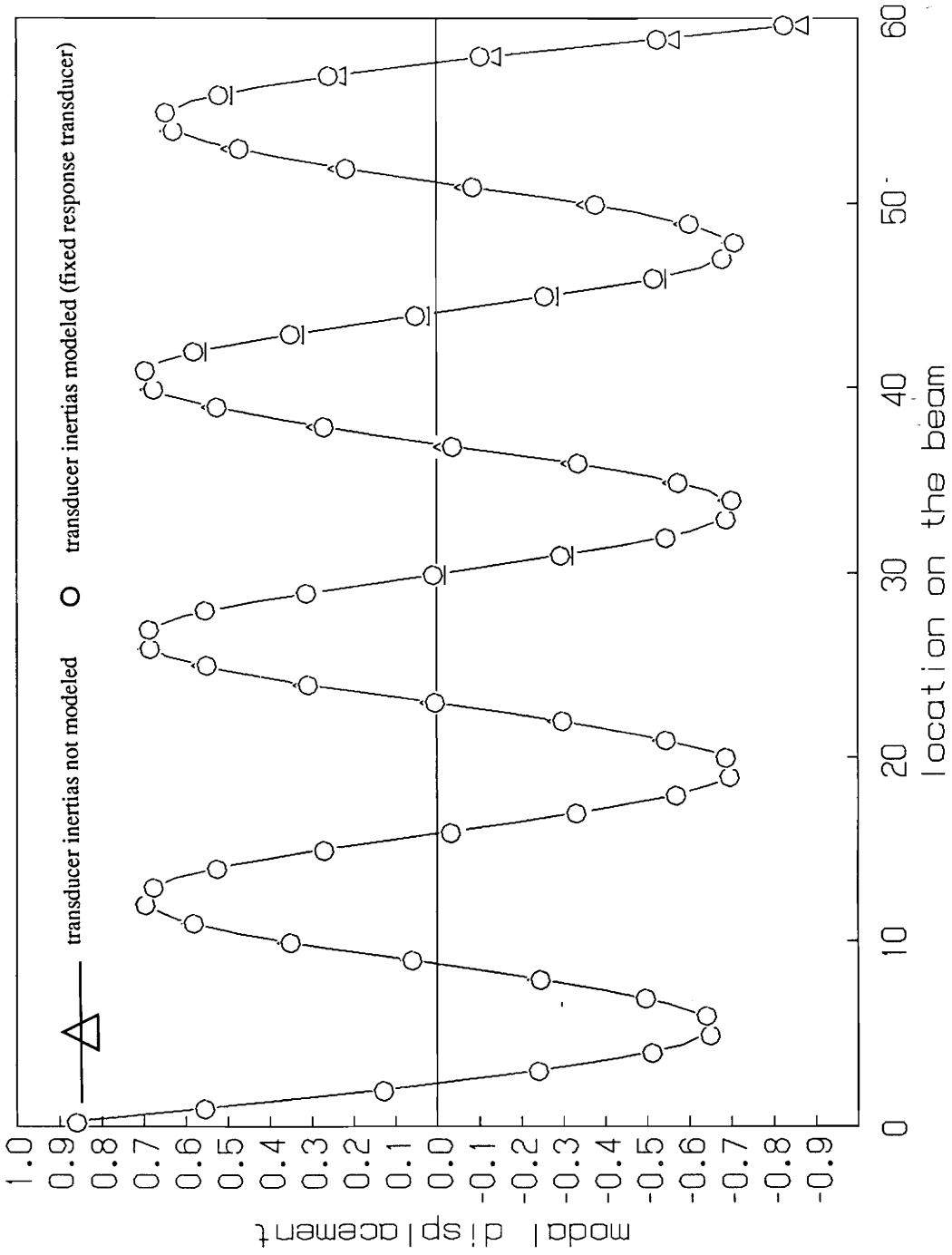


Figure 6.3 Eighth mode of BEAM 2 (TEST 2) showing the effect of inertia-loading by the fixed accelerometer

6.1.3 Finite Element Models and Results - TEST 3

TEST 3 uses the same beam used in TEST 2. The objective of this test was to assess the influence of the exciter (shaker/force transducer) location on the modal properties. As described earlier, the test has two models, **Model 1** and **Model 2**. **Model 1** tag is used for the case in which the driving-point is located at the top of the beam, while **Model 2** tag is used for the case in which the driving-point is located at the bottom. The transducer used in this test had minimal mass relative to the force transducer mass. Hence, it is not modeled in the FE model. The FE analyses done was based on 62 Euler-Bernoulli beam elements. The results are shown in Table 6.6.

Table 6.6. Natural frequencies from FEA for various modeling conditions from TEST 3 (Model 1)

Mode Number	Simple Model	Gravity Included	Transducer Inertias Included	Gravity and Transducer Inertias Included
1	14.183	14.533	14.051	14.394
2	39.096	39.340	38.749	38.986
3	76.644	76.836	75.993	76.179

6.2 Results from Experimental Modal Analyses

In this Section, results obtained from the 3 modal tests will be outlined. Only estimates of natural frequencies and damping ratios, along with FE natural frequencies, will be presented. The results for mode vectors will be presented in the next Section, where comparisons will be made with FE models, using the modal assurance criterion (MAC). Since the FRFs were curve-fitted individually, there are as many estimates of the global modal parameters as there are FRFs (measurement locations). Therefore, to show the variability in estimating these global parameters, they are stated as a mean with the associated standard deviation. Also, the mean value of these parameters are used as the true experimental values, for correlation with analytical models.

6.2.1 Results from TEST 1

This test was performed, using an electrodynamic shaker as the excitation source, in the frequency range 0 - 1000 Hz. FRF estimation was made with the H^c type estimator, using 20 distinct averages. The details of the test are given in Table 5.1. A total of 46 FRFs were curve-fitted, 23 each from translational and rotational response measurements. The FRFs were fitted individually. Ten beam bending modes were identified for both translational and rotational measurements. Table 6.7 shows the first ten beam bending natural frequencies, identified from both translational and rotational measurements, compared with those from the corresponding FE model. Since the accelerometer was moved along the structure to facilitate response measurements at the 23 locations, the identified natural frequencies varied slightly for each location. The tabulated results show the mean and standard deviation (in parentheses). The figures in the column for FEA natural frequencies denote the average value, obtained from the 23 FE analyses (see Tables 6.3 and 6.4), and the corresponding standard deviation.

Table 6.7. Comparison of FEA and EMA natural frequencies from TEST 1, along with damping ratio estimates from EMA

Mode	FEA (S.D.)	EMA			
		Translation		Rotation	
		Natural Freq. Mean (S.D.)	Damping Ratio	Natural Freq Mean (S.D.)	Damping Ratio
1	17.736 (0.017)	17.62 (0.06)	7.135 (1.007)	17.54 (0.25)	7.705 (1.459)
2	48.899 (0.044)	48.14 (0.19)	2.664 (0.588)	48.16 (0.12)	2.540 (0.116)
3	95.878 (0.083)	94.35 (0.33)	1.273 (0.107)	94.26 (0.16)	1.288 (0.110)
4	158.512 (0.133)	155.95 (0.59)	0.820 (0.188)	155.78 (0.23)	0.800 (0.226)
5	236.817 (0.195)	233.00 (0.28)	0.568 (0.118)	232.97 (0.20)	0.534 (0.031)
6	330.792 (0.267)	325.88 (0.24)	0.417 (0.022)	325.89 (0.25)	0.418 (0.047)
7	434.435 (0.350)	433.77 (0.33)	0.286 (0.013)	433.80 (0.37)	0.290 (0.014)
8	565.743 (0.442)	557.51 (0.40)	0.221 (0.048)	557.52 (0.41)	0.221 (0.050)
9	706.711 (0.542)	696.61 (0.51)	0.192 (0.008)	696.92 (0.51)	0.192 (0.010)
10	863.333 (0.648)	851.93 (0.64)	0.158 (0.006)	851.88 (0.60)	0.156 (0.008)

6.2.2 Results from TEST 2

This test was performed in the range 0-500 Hz. Impulse excitation using an impact hammer was the excitation source. FRFs were obtained using the H_1 estimator, using 10 distinct averages. The details of the test are outlined in Table 5.2. The same accelerometer used in TEST 1 is used here and the response location is fixed at the bottom of the beam. Impact excitation was made at 61 equally spaced locations along the beam. FRFs were acquired from only translational measurements. These FRFs were curve-fitted individually and 8 beam bending modes were identified. Table 6.8 shows the results for natural frequencies and damping ratios along with FE natural frequencies.

Table 6.8. Comparison of FEA and EMA natural frequencies from TEST 2, along with damping ratio estimates from EMA

Mode Number	FEA Natural Freq.	EMA	
		Natural Freq. Mean (S.D.)	Damping Ratio Mean (S.D.)
1	14.486	14.502 (0.152)	4.194 (1.953)
2	39.216	39.565 (0.084)	1.538 (0.260)
3	76.602	77.575 (0.117)	0.760 (0.169)
4	126.486	128.198 (0.346)	0.472 (0.044)
5	188.869	191.625 (0.035)	0.321 (0.005)
6	263.748	267.722 (0.149)	0.233 (0.051)
7	351.123	356.491 (0.042)	0.185 (0.012)
8	450.998	458.034 (0.182)	0.314 (0.072)

6.2.3 Results from TEST 3

This test was performed in the frequency range 0 - 125 Hz. Two tests, **Model 1** (shaker located at the top of the beam) and **Model 2** (shaker located at the bottom of the beam), were conducted. The main objective of the test was to study the influence of the location of shaker on the modal parameters. FRFs were acquired from translational measurements using the H_1 estimator, at 21 equally spaced locations along the beam. The response measurements were made using an accelerometer having minimal mass. The FRFs were curve-fitted individually and three beam bending modes were identified. The results for natural frequencies and damping ratios are shown in Table 6.9, for both models.

Table 6.9. Comparison of natural frequencies and damping ratios obtained from EMA for Model 1 and Model 2

Mode Number	Shaker attached at top of the beam		Shaker attached at bottom of the beam	
	Natural freq. Mean (S.D.)	Damping ratio Mean (S.D.)	Natural freq. Mean (S.D.)	Damping ratio Mean (S.D.)
1	14.389 (0.010)	1.137 (0.074)	14.427 (0.038)	1.154 (0.107)
2	39.595 (0.032)	0.469 (0.018)	39.588 (0.023)	0.405 (0.321)
3	77.602 (0.036)	0.281 (0.020)	77.404 (0.103)	0.250 (0.088)

6.3 Comparison and Discussion of Results

6.3.1 Correlation Between Test and Analysis Models - TEST 1

Natural Frequencies

Table 6.7 lists the natural frequencies obtained from FEA and EMA. Note that the frequencies from FEA are consistently higher than those from EMA. This, among other factors, could be attributed to uncertain values used for material properties. Furthermore, frequencies identified from rotational and translational measurements are not identical, as they are obtained by curve-fitting different FRFs. Moving the accelerometer along the structure to make response measurements changes the system (structure), hence the natural frequencies. This can be seen from the standard deviation of the natural frequencies obtained by EMA for each mode. The correlation between EMA and FEA natural frequencies is shown in Fig. 6.4. There is excellent correlation between EMA and FEA natural frequencies. The nature and degree of correlation obtained suggests that the observed small differences between EMA and FEA frequencies must be the result of using incorrect values for the material properties of the beam.

FE analyses were performed, with the force-transducer and accelerometer mass modeled, for each response location used in EMA. For each run (FE analysis), the natural frequency and the modal displacement of the location of the accelerometer, for all the 10 modes were recorded. Thus simulating the effect of moving the accelerometer in the testing. From the results obtained, correlations were made with the EMA results to see whether the variation of natural frequency with response location in EMA was due to the accelerometer mass. Figure 6.5 shows the correlation obtained, for rotations and translations, for the first 10 modes. As can be seen, lower modes show reduced correlation, whereas higher modes show correlation of above 95%. Since the spectral resolution used in the FRF estimation was 2.5 Hz, fluctuation in frequency for lower modes, being small,

tended to be more susceptible to noise. This clearly shows that the variation of natural frequency with response location, observed in EMA results, is due to the changing locations of the accelerometer. From Table 6.7, the standard deviation of the variation in natural frequencies from EMA compares very closely with those from FEA. Also, the variation is closer for higher modes than for lower modes (frequencies), which could be attributed to the frequency resolution used. Thus, the actual variation of frequencies due to the curve-fitting process is very small.

A Linear Regression Model for Correlating EMA and FEA Natural Frequencies

Using the data presented in Fig. 6.4 , a linear regression analysis is performed between FEA and EMA natural frequencies. The following linear regression model is used,

$$Y = A + BX \quad (6.1)$$

where, coefficients \hat{A} and \hat{B} are estimated based on data in Fig. 6.4. The estimates of A and B will be denoted by \hat{A} and \hat{B} respectively. Based on these estimators \hat{A} and \hat{B} , the linear regression model in Eq. (6.1) can be represented as,

$$Y = \hat{A} + \hat{B}X \quad (6.1a)$$

These estimators are unbiased estimators of the linear regression parameters ²⁵ A and B . That is,

$$E\{\hat{A}\} = A \quad (6.2)$$

$$E\{\hat{B}\} = B \quad (6.3)$$

The FEA natural frequencies are denoted by the independent variable X and the EMA frequencies by Y . Ideally (for perfect correlation in our case), the estimate \hat{A} should have a value of "0" and the estimate \hat{B} a value of unity. However, if random and/or bias errors are present, then the esti-

²⁵ See Draper, N.R. and Smith, H., *Applied Regression Analysis*, Wiley, New York, 1981, 2nd ed.

mates \hat{A} and \hat{B} deviate from their ideal values. The estimates \hat{A} and \hat{B} are estimated using the method of least-squares, and are obtained as

$$\hat{A} = -0.301069 \quad \hat{B} = 0.986411 \quad (6.4)$$

The standard deviation of the above two estimates is obtained as,

$$\sigma_{\hat{A}} = 0.177885 \quad \sigma_{\hat{B}} = 0.000402 \quad (6.5)$$

From the above standard deviation for the estimators \hat{A} and \hat{B} we note that there is higher variability in estimating \hat{A} than in estimating \hat{B} . Using the student's *t*-distribution, 95% confidence levels can be established for the parameters (estimates) \hat{A} and \hat{B} ²⁶. Based on 8 statistical degrees of freedom (a sample size of 10), they are

$$-0.621995 \leq A \leq 0.019857 \quad (6.6)$$

$$0.985484 \leq B \leq 0.9873338 \quad (6.7)$$

Since the confidence bounds for the parameter *A* includes the value "0" in its range, the possibility that 0 is the true value of *A* cannot be ruled out, at 95% confidence level. However, confidence bounds for the parameter *B* does not include the ideal value of "1" in its range. Therefore, the true value of *B* lies in the range specified by Eq. (6.7), at 95% confidence level. Indeed, this is to be expected, since the true values for the material properties used in the FE model are unknown. Furthermore, shear deformation and rotatory inertia effects are not accounted for in the FE model, because of using the Euler-Bernoulli beam element. All these factors contribute to the non-unity condition of the parameter *B*.

Quantifying Errors in Natural Frequency Estimation

²⁶ Lipson, C. and Sheth, N., *Statistical Design and Analysis of Engineering Experiments*, McGraw Hill, 1973

Although finite element models are used here as the reference, the true (accurate or actual) values of modal parameters are not known. For example, the true values of natural frequencies are unknown. However, experimentally obtained natural frequencies are in close agreement with analytically (FEA) established natural frequencies. This conclusion can be made based on the linear regression model presented above. It was shown that the experimental and analytical frequencies differed only by a scale factor, which was identified as being due to incorrect values of material properties used in the FE model. Based on these observations we can conclude that the experimentally identified frequencies are accurate (within the limits of capabilities of the processes used in EMA). Since the curve-fitting was done to each FRF individually, there are as many natural frequency estimates as there are FRFs. Ideally, each estimate of the natural frequency should be identical. In practice, the combined errors due to measurement (transduction, signal-processing and FRF estimation) and modal parameter estimation (curve-fitting) contribute to the scatter observed for these estimates. Therefore, the average (arithmetic mean) of these estimates is a good estimate of the true natural frequency. Of course, we make the assumption that the scatter is random. Furthermore, the scatter (variance) should provide a good indication of the error in the experimental determination of the natural frequencies.

The errors in estimating natural frequencies have already been quantified in various forms. Table 6.7 shows the standard deviation of natural frequency estimates and Fig. 6.5 shows the correlation observed for shifts in natural frequencies due to changing accelerometer locations. Figure 6.4 and the corresponding linear regression model give an idea of the degree of correlation that exists between experimental and analytical natural frequencies. Since the accelerometer location changed for each measurement, the natural frequencies of the system changed too, depending on the location. This explained the increased standard deviation observed in estimating higher modes (see Table 6.7).

The error in estimating the natural frequencies can also be quantified for each location (from measurement to measurement). This can be done by stating the percentage deviation, from nominal or mean value, of each estimate of a natural frequency. Since the natural frequencies change

for each measurement, nominal values can be only determined in an approximate fashion. Based on this error modeling, the following observation is made

- The errors are significant only at locations close to a nodal point of a mode. These errors are due to very poor signal-to-noise ratios and are all within 2% of the corresponding nominal values.

Mode Vectors

Mode shapes from EMA are correlated with those from FEA using the modal assurance criterion (MAC). Figures 6.6 and 6.7 show the MAC values for translational and rotational mode vectors respectively. Further, these Figures also show the improvement in correlation obtained by including the accelerometer and the force transducer inertias in the FE model. Though the increase in correlation is small, higher modes show larger increase in correlation as compared to lower modes. This can be seen in Figs. 6.6 and 6.7, corresponding to translational and rotational modes respectively, where modes 1 through 10 are shown. Thus, the amount and trend in which correlation increases indicates that the process of experimental modal analysis is sensitive enough to measure the effect of accelerometer and force transducer inertias on the structure's dynamics. The MAC values for rotations are very poor compared to translations. This was primarily due to the very poor quality of rotational measurements. The signal-to-noise ratios for rotational measurements was quite low. Both translational and rotational data exhibit relatively poor correlation for the first mode, compared to other lower modes. The only probable reason seems to be the spectral resolution used in FRF estimation.

Another observation that can be made from the correlation of translational mode vectors is that the MAC value progressively decreases for higher modes. Considering the nature and extent of improvement in correlation realized in including the transducer inertias in the FE model, and observing the closeness in standard deviation values obtained from EMA and FEA, for natural frequencies, it could be inferred that the cause of such a trend cannot be due to inertia-loading ef-

fects of the transducer inertias. The above observations lead to the suspicion of the boundary that exist in reality. The shaker attached to the beam adds inertia and moment restraint. These could be eliminated by performing a modal test using an impact hammer as the excitation source.

Quantifying Errors in Estimating Modal Displacements

Based on the degree of correlation (MAC) seen between experimental and analytical mode vectors, we conclude that the mode vectors from EMA must be very accurate. It should be pointed out here, as a reminder, that the FE results are based on the Euler-Bernoulli beam element, which does not account for rotatory inertia and shear deformation effects. These effects are assumed to be negligible for the case at hand, on account of the high degree of correlation observed for the mode vectors between EMA and FEA. Also, this was justified because results from Table 6.2 suggest that the influence of shear deformation and rotatory inertia effects for the frequency range considered here is indeed small. Therefore, based on these assumptions, the errors in estimating modal displacements are quantified using the FE model as the reference. The error in estimating the modal displacement (imaginary component of the residue) is stated as a percentage deviation from the corresponding displacement from the FE model. The following observations are made,

- The error in estimating the modal displacement are all within 5%, except for locations near the nodal points of a mode.
- At locations close to nodal points the error is very significant. These are as high as 100 to 200 percent. However, since these displacements are very small, about two orders of magnitude less than the maximum modal displacement, such large errors associated with these displacements do not alter the quality of the mode vectors significantly.

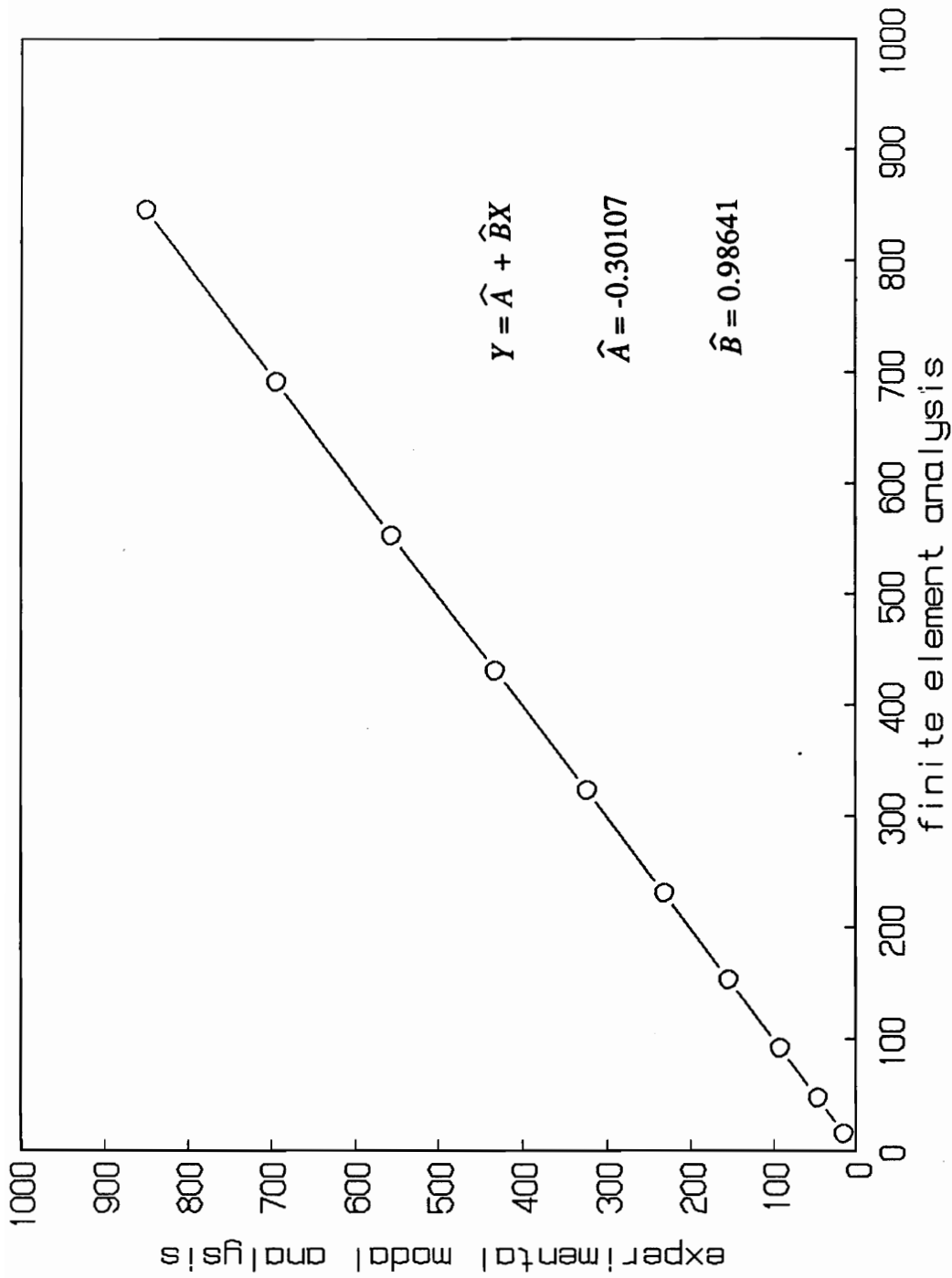


Figure 6.4 TEST 1 - Correlation between FEA and EMA natural frequencies from translational data

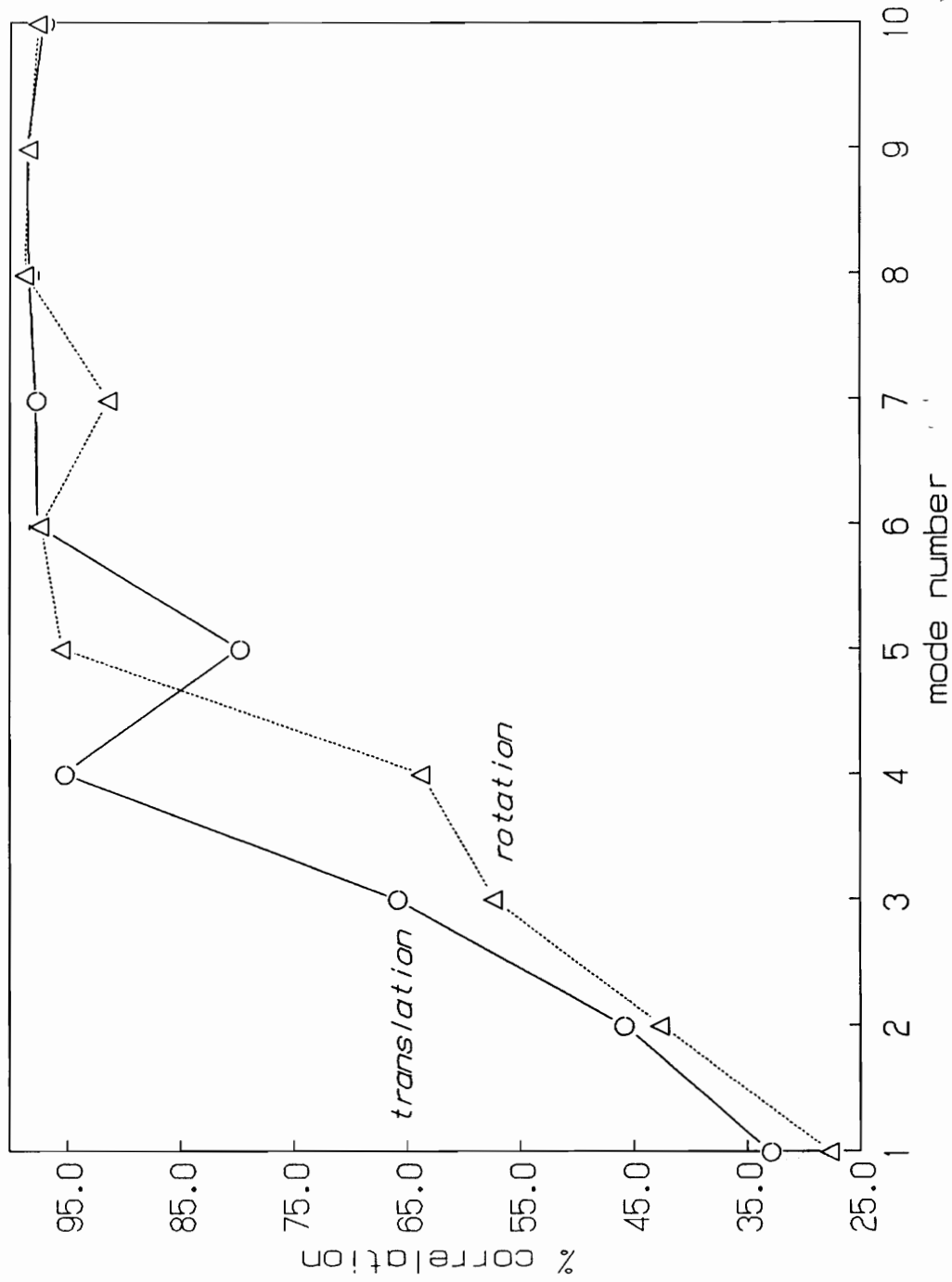


Figure 6.5 TEST 1 - Correlation, between FEA and EMA, of variation in natural frequencies due to changing accelerometer locations

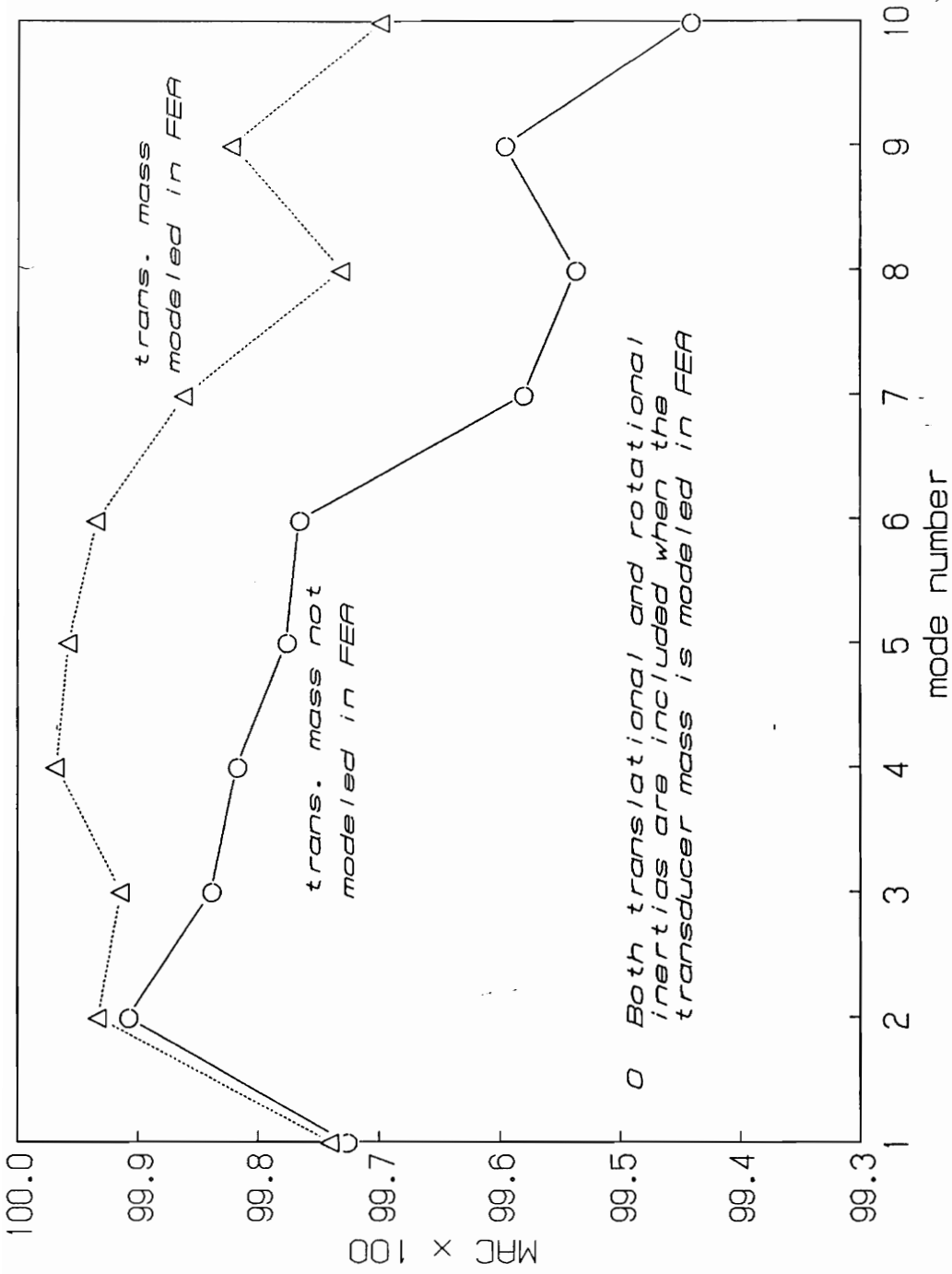


Figure 6.6 TEST 1 - Modal assurance criterion (MAC) between FEA and EMA mode vectors for translational data

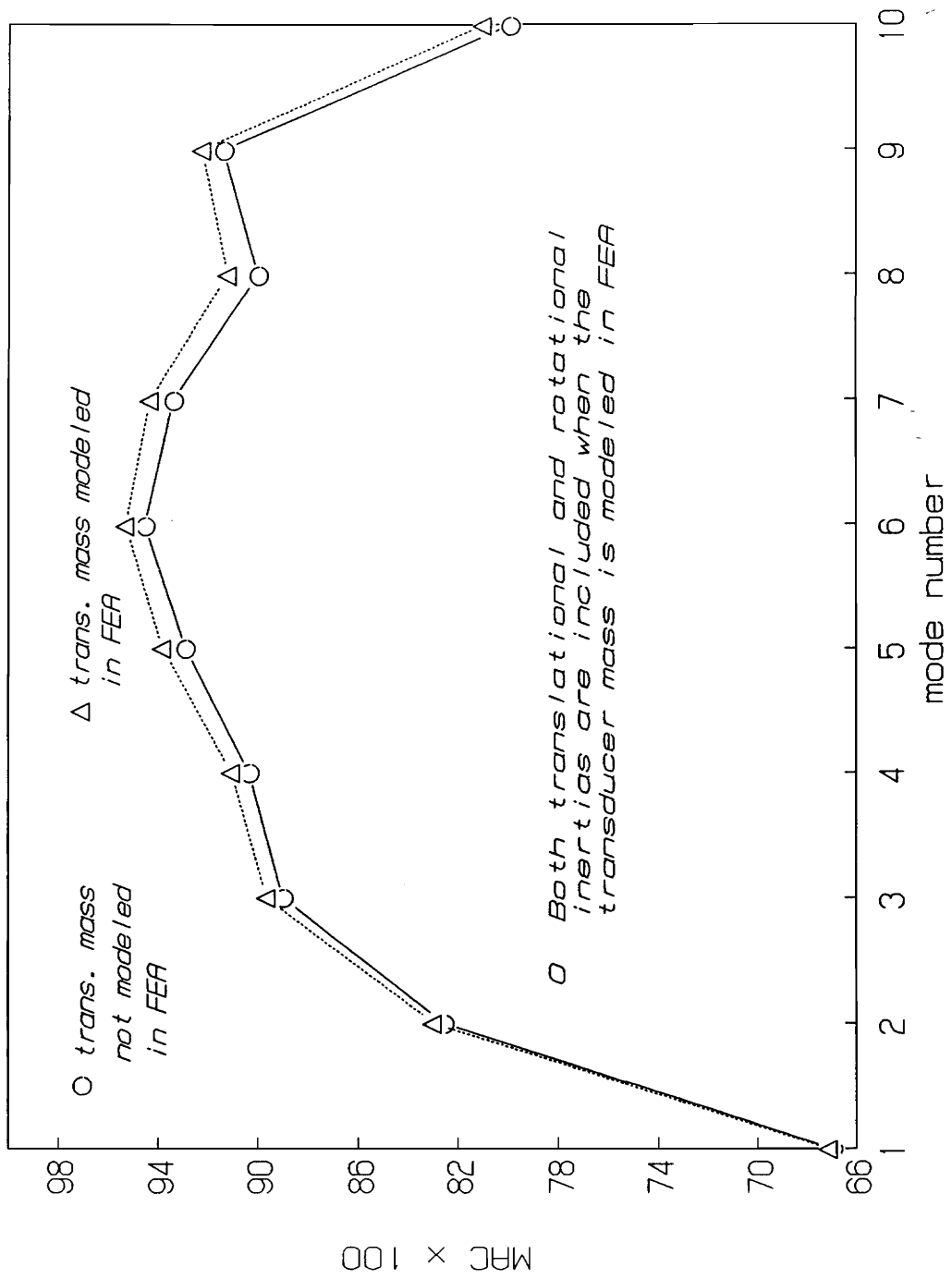


Figure 6.7 TEST 1 - Modal assurance criterion (MAC) between FEA and EMA mode vectors for rotational data

6.3.2 Correlation Between Test and Analysis Models - TEST 2

Based on the results from TEST 1, two main objectives of this test were:

1. To see the degree of variability in estimating the modal parameters, inherent to the modal test and identification procedure. This could not be directly ascertained from TEST 1, due to the effect of moving the accelerometer in the test.
2. To know whether the gravity force acting on the beam, suspended vertically, affects the structure's lower modes significantly. This was suspected because of the lower correlation observed for the first mode, compared to other lower modes in the previous test.

Natural Frequencies

Table 6.8 compares natural frequencies obtained from EMA and FEA. Also, damping ratios estimated from EMA are shown. As can be seen, the FEA frequencies are consistently lower than the EMA frequencies. Figure 6.8 shows the correlation between EMA and FEA natural frequencies. Again, as with TEST 1, excellent correlation is observed. Since the test is done with the accelerometer location fixed at the bottom of the beam through-out testing, natural frequencies obtained should be consistently same for all locations, within the limits of experimental error. Note the high degree of consistency in identifying natural frequencies and damping ratios. These errors are quantifiable and are inherent to the EMA process. Note that these errors are much lower than those seen in TEST 1. The larger standard deviations observed for TEST 1 are due to the effect of moving the accelerometer mass.

A Linear Regression Model for Correlating EMA and FEA Natural Frequencies

Again, as before, a linear regression model based on Eq. (6.1) can be used to assess the degree of correlation achieved between FEA and EMA natural frequencies. Using data from Fig. 6.8 (Table

6.8), the parameters A and B in Eq. (6.1a) can be estimated using the method of least-squares. The estimates \hat{A} and \hat{B} are obtained as

$$\hat{A} = -0.273519 \qquad \hat{B} = 1.016124 \qquad (6.8)$$

The standard deviation of the above two estimates is obtained as,

$$\sigma_{\hat{A}} = 0.021603 \qquad \sigma_{\hat{B}} = 0.000091 \qquad (6.9)$$

The standard deviation of both the estimates \hat{A} and \hat{B} are much lower than those seen for TEST 1. The standard deviation of the estimator \hat{B} , in particular, is very low. This could be identified as being due to the lower standard deviations seen in estimating the natural frequencies (Table 6.8). Using the student's t -distribution, 95% confidence levels can be established for the parameters (estimates) \hat{A} and \hat{B} . Based on 6 statistical degrees of freedom (a sample size of 8), they are

$$-0.315375 \leq A \leq -0.231663 \qquad (6.10)$$

$$1.015900 \leq B \leq 1.016347 \qquad (6.11)$$

Since the value 0 (for A) does not lie within the confidence bounds, we could say that the true value of A is not 0, at 95% confidence level. Therefore, there is a bias equal to a value specified by the range in Eq. (6.10). Since the mean value of this is around -0.274 Hz, the bias is quite negligible. Also, the true value of the parameter B lies in the range specified by Eq. (6.11), at 95% confidence level. Once again, the same argument used with TEST 1 data can be used here. Thus, non-inclusion of shear-deformation and rotatory inertia effects and incorrect material property values used in the FE model could account for the scaling difference.

Quantifying Errors in Natural Frequency Estimation

Compared to data from TEST 1 results (Table 6.7) the scatter in estimating natural frequencies is much lower for TEST 2 (Table 6.8). As a result, the parameters in the regression model had lesser standard deviation. Since the accelerometer location is fixed in this test, it is possible to use the

mean value of all the natural frequency estimates as the nominal value. Again, the errors in estimating natural frequencies can be stated as a percentage difference between the nominal (mean) value and the actual value. The following observation is made,

- Errors are significant only at locations near nodal points of a mode. These errors are less than 2% to 3% of the nominal value for each mode.

Mode Vectors

Mode shape correlations between EMA and FEA are shown in Figs. 6.9 and 6.10. As with TEST 1, excellent correlations are observed, except for the first mode which has a MAC value of 0.977. Modes 2 through 8 have a typical MAC value in excess of 0.998. Note the increased MAC values obtained by including the accelerometer inertias in the FE model. Figure 6.10 shows this for modes 2 through 8. The trend seen is qualitatively similar to the one observed for TEST 1. Correlations performed with the FE model that included the gravity force did not show any significant change compared to the correlations with FE model that did not account for gravity force.

Quantifying Errors in Estimating Modal Displacements

Using the modal displacements from FE model as the reference, the errors in estimating modal displacements are evaluated. The same procedure used for quantifying errors of mode vectors from TEST 1 is used here. The following is the observation made,

- Except at locations close to nodal points of modes, the errors are typically less than 5%. At locations close to nodal points, as with mode vectors from TEST 1, large errors of the order of up to 200% are noted. Since displacements at locations close to nodal points are so small, these large errors do not impact the quality of the mode vectors significantly.

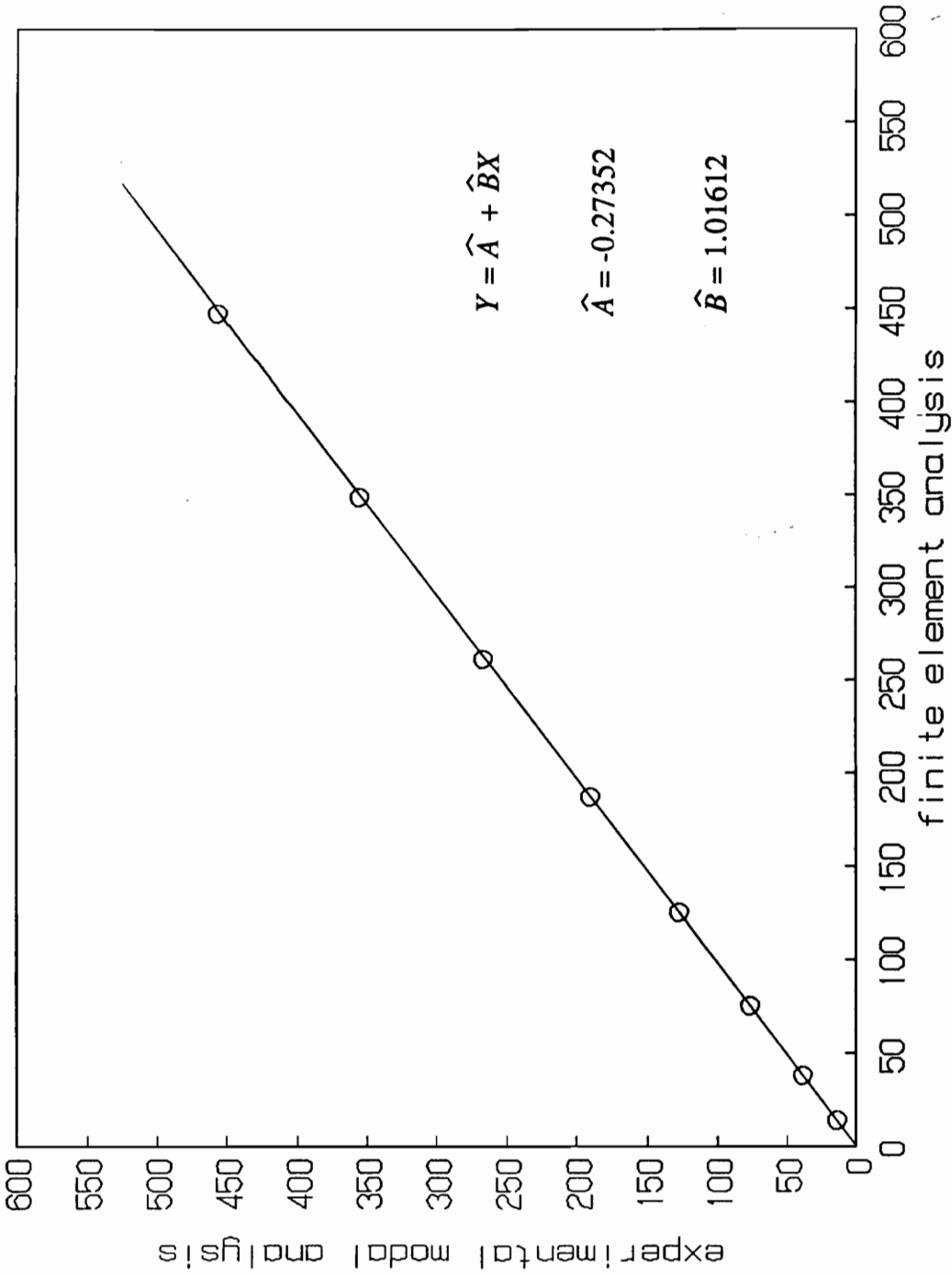


Figure 6.8 TEST 2 - Correlation between FEA and EMA natural frequencies from translational data

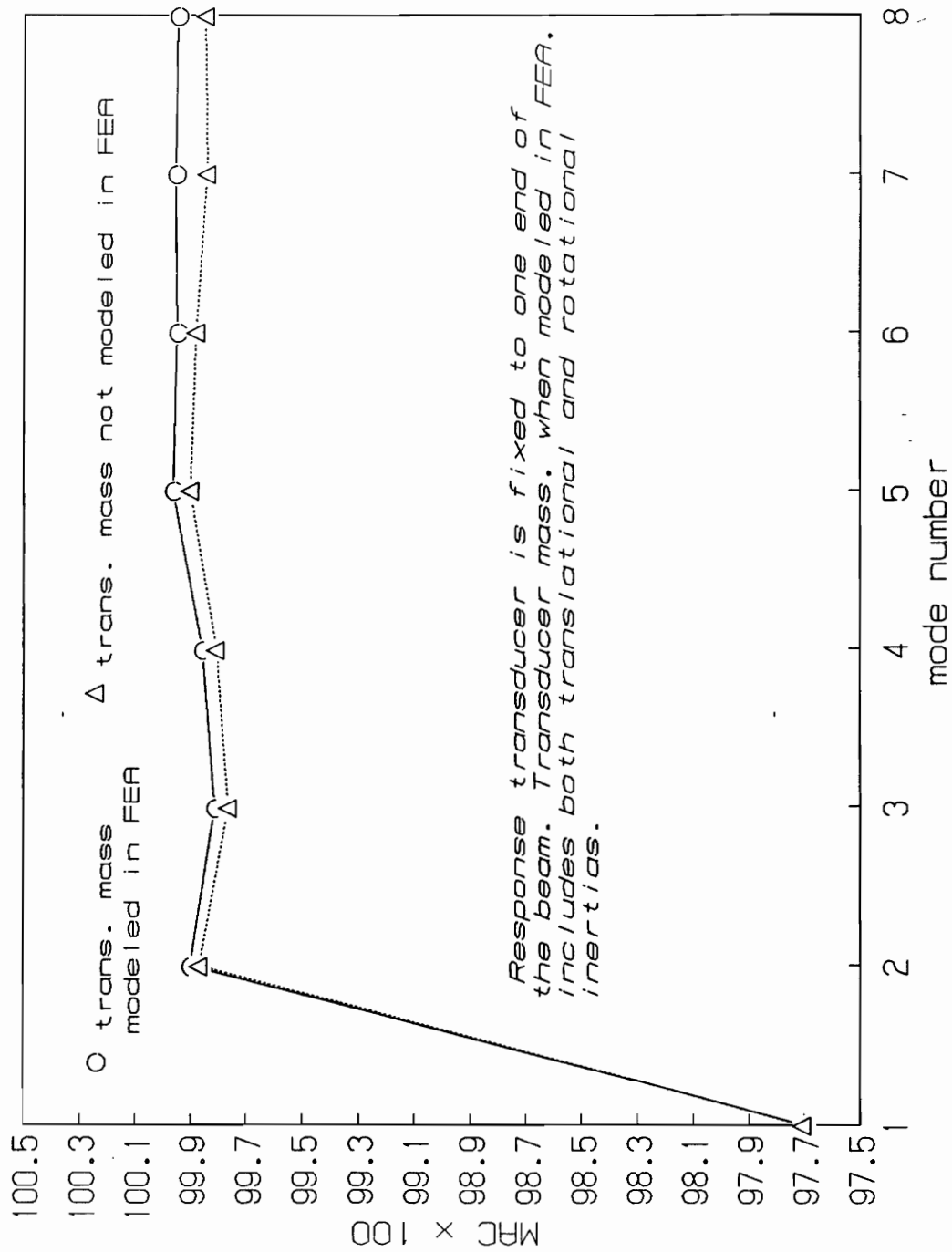


Figure 6.9 TEST 2 - Modal assurance criterion (MAC) between FEA and EMA mode vectors for translational data

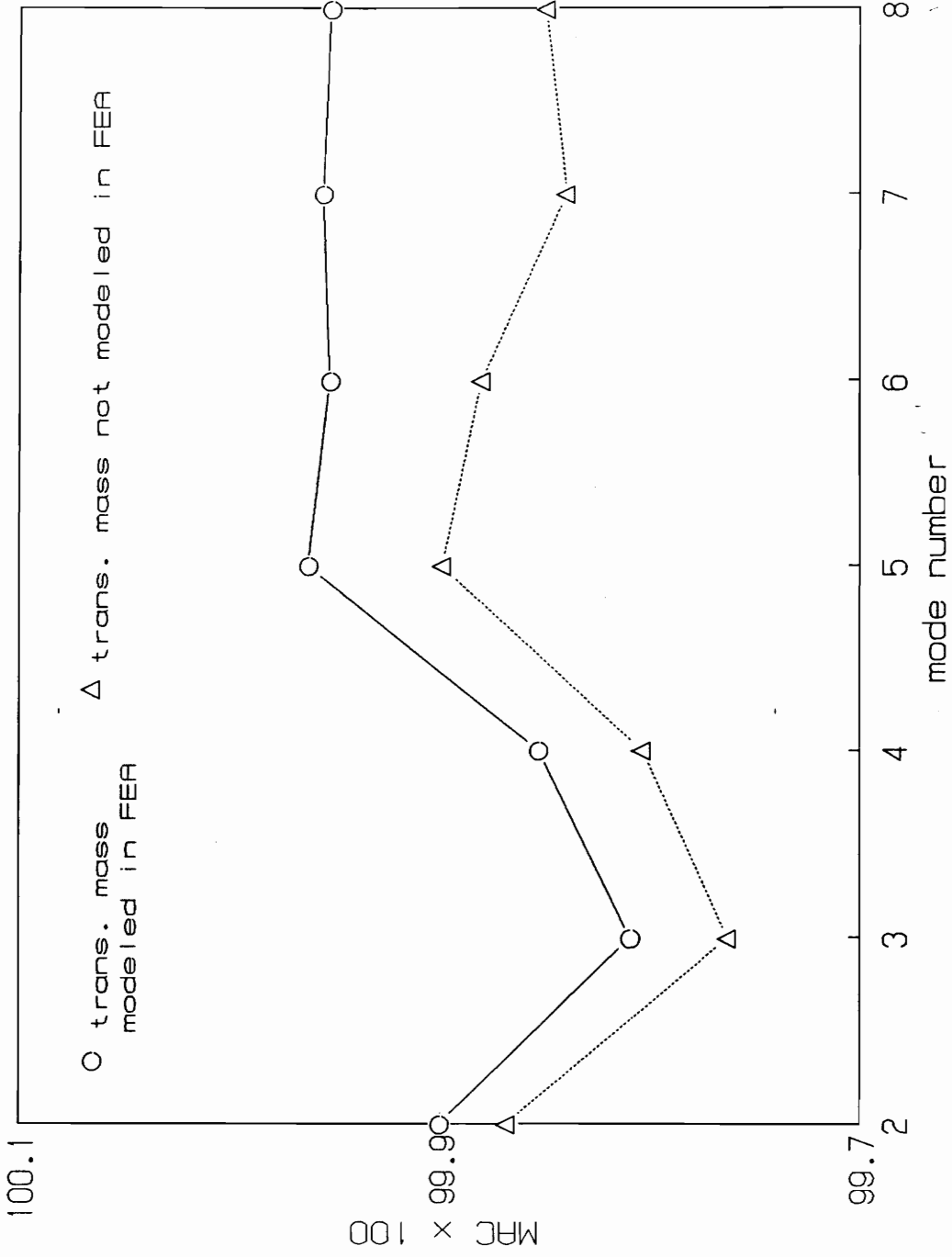


Figure 6.10 TEST 2 - Modal assurance criterion (MAC) between FEA and EMA mode vectors for translational data, shown for modes 2 through 8

6.3.3 Correlation Between Test and Analysis Models - TEST 3

The main objective of this test was to assess the influence of shaker location on the resulting modal model. Three modes were identified and the results for damping ratios and natural frequencies for the two models are given in Table 6.9.

Natural Frequencies and Damping Ratios

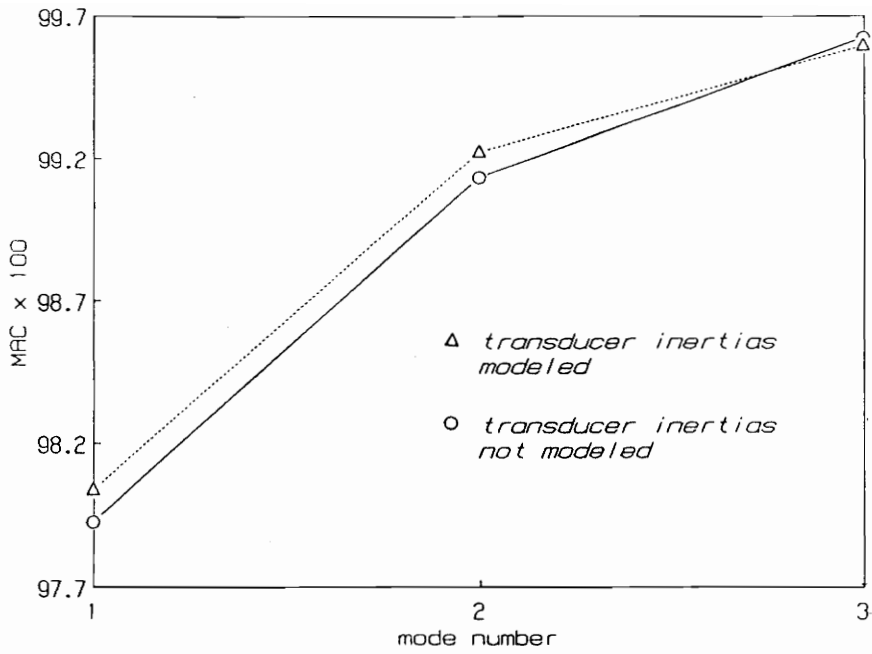
Since the test was done on the same beam used for TEST 2, comparisons can be made with results from TEST 2. In particular, the damping ratio estimates from this test differ widely from the estimates from TEST 2. The difference for the first, second and the third mode are approximately 350%, 300% and 300% respectively. The frequency resolution used in this test being 0.3125 Hz., the damping estimates are more accurate than the estimates from TEST 2. The standard deviation values seen for natural frequency and damping ratio estimates are much lesser than those observed in TEST 2.

Mode Vectors

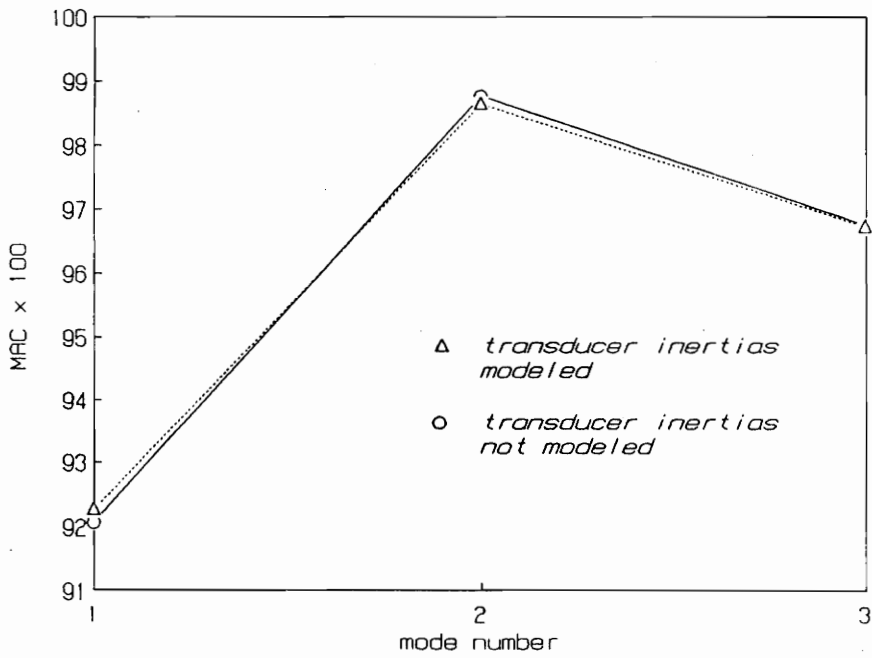
The results of correlation of mode vectors between the test and FEA are shown in Fig. 6.11. Mode vectors from **Model 1** seem to be as good as the ones from the previous tests (TEST 1 and TEST 2). However, the MAC values for **Model 2** suggest that the quality of the mode vectors are poor. The first mode, in particular, seems to have suffered the most, though the natural frequency of the first mode has not changed significantly. This implies that the data for the first mode is in serious error, and indeed, this is the case. The first mode from **Model 1** and **Model 2**, plotted against the corresponding FEA mode vectors are shown in Figs. 6.12 and 6.13 respectively. Compared to **Model 1**, **Model 2** results seem to be very poor, as is evident from the plots.

The driving-point FRFs (accelerance) for the two models are shown in Fig. 6.14. Observing the lower end of the frequency range, **Model 1** suggests a behavior typical of structures which are

dominated by mass effects whereas the corresponding region from the FRF of **Model 2** suggests a stiffness domination. This leads one to doubt the validity of the boundary conditions which the configuration in **Model 2** is supposed to simulate. An examination of all the FRFs from **Model 2** showed the same characteristics seen in the lower frequency range of the driving-point FRF (Fig. 6.14b). Further, examination of all the curve-fits on these FRFs showed a spurious mode below the first mode. The first mode was at approximately 14.5 Hz, whereas the spurious mode had natural frequencies ranging from 1 to 10 Hz (the median value being between 3 and 4 Hz), depending on the FRF. The parameter estimation algorithm had identified a structural mode in the frequency range 0 to 10 Hz, for all the FRFs. Since the algorithm is an MDOF curve-fitter that accounts for the contribution of out-of-band modes, it produced erroneous estimates for the first mode (note, however, the natural frequency estimates for the first mode were not affected). Though the natural frequencies are not substantially different between the two models, the mode vectors are. This shows that the importance of proper test configuration and exciter location cannot be under-emphasized. Another important observation which could be made from TEST 3 results is that the variance (standard deviation) of the natural frequency and damping ratio estimates are very low, compared to tests 1 and 2. In fact, comparison of the estimates from the first three modes from TEST 2 proves this point. Therefore, the quality of the modal parameter estimation is seen to be excellent.



(a)



(b)

Figure 6.11. TEST 3 - Modal assurance criterion (MAC), between EMA and FEA mode vectors for (a) Model 1 and (b) Model 2

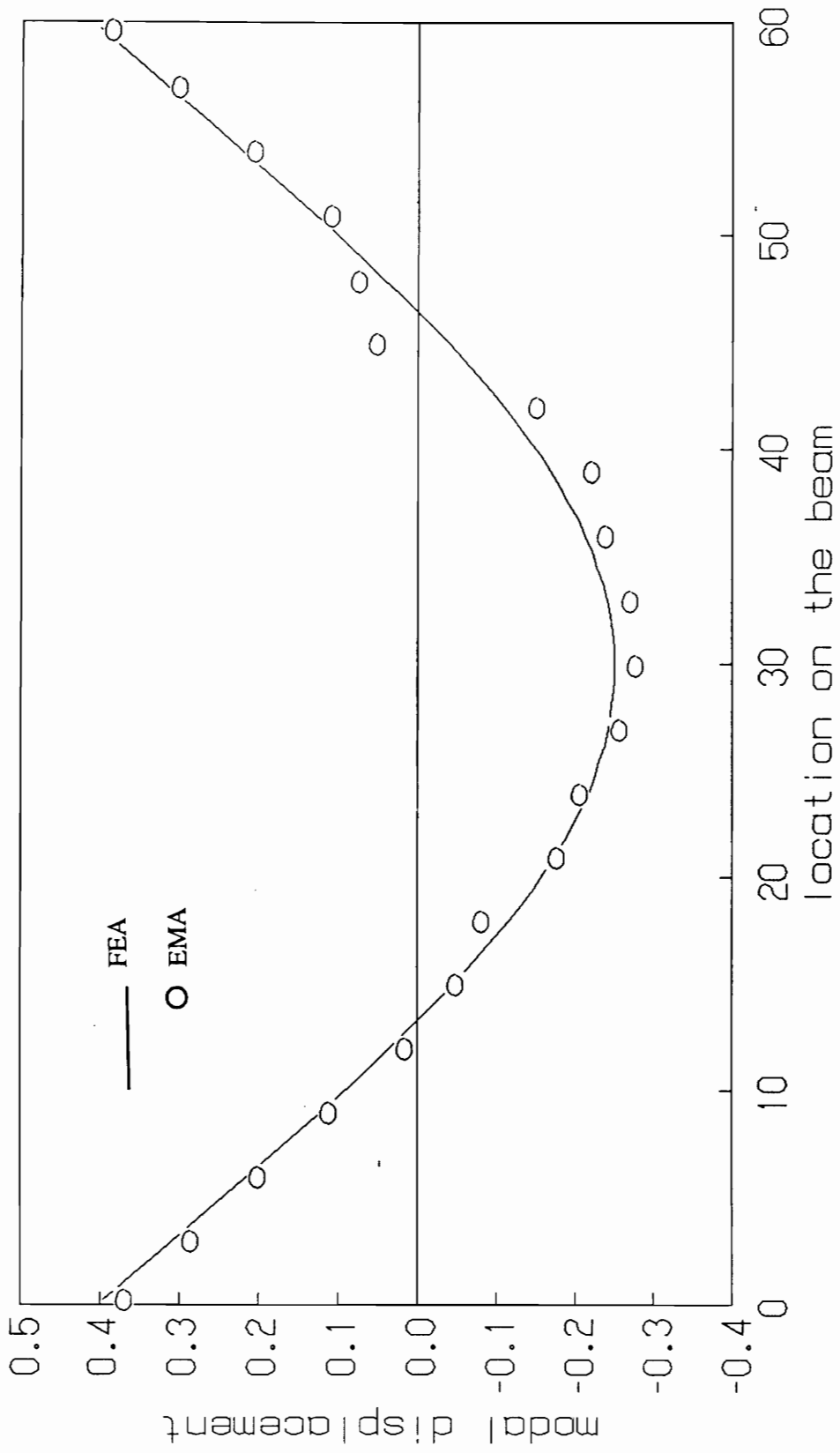


Figure 6.12 TEST 3 - Comparison of mode shape data from FEA and EMA for the first mode (Model 1 - shaker located at the top)

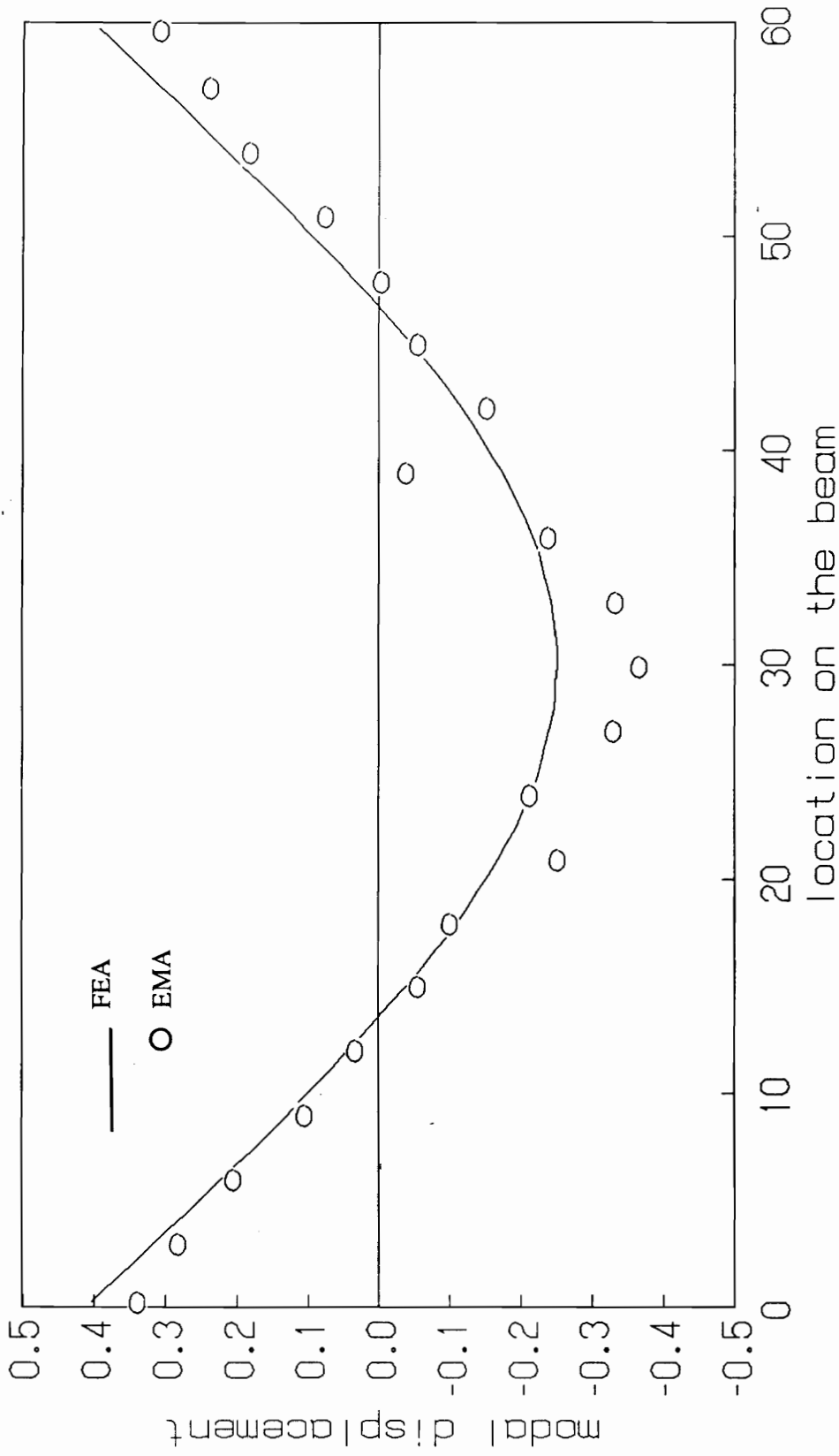


Figure 6.13 TEST 3 - Comparison of mode shape data from FEA and EMA for the first mode (Model 2 - shaker located at the bottom)

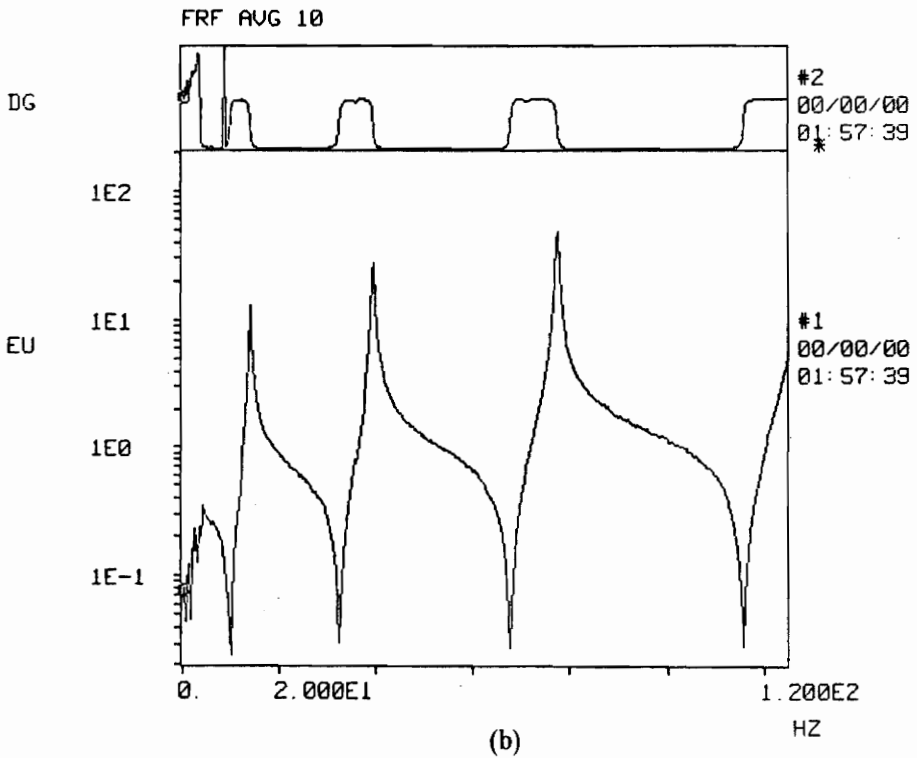
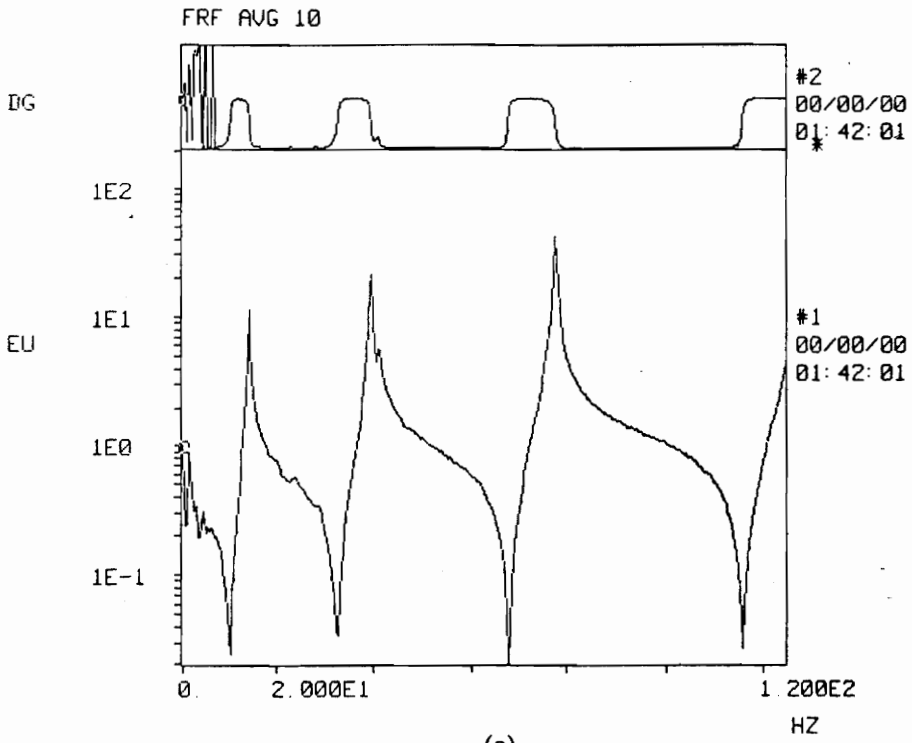


Figure 6.14. TEST 3 - Driving-point FRF (accelerance) from (a) Model 1, and (b) Model 2

6.4.4 Investigation/Reconciliation of Poor Correlation Observed for the First Mode

The first mode, in all the tests conducted seems to have a poor correlation with analytical predictions from FEA. Only the first mode seems to have suffered the most, while the higher modes have good correlation with FEA results. Therefore, speculations made to reconcile the observed lower correlation for the first mode are limited to those factors which typically yield poor results in the lower frequency range. The following are some of them:

1. The frequency resolution used in the spectral estimation is one plausible reason. The frequency resolution used in these tests are shown in Table 6.10. The frequency resolution used in TEST 1, as a percentage of the natural frequency of the first mode is approximately 14%. This could yield substantially biased results. Since the bias results due to frequency resolution, both the autospectra and cross-spectra are susceptible to this type of bias error.
2. In all the 3 tests, the beam was suspended vertically by means of an elastic cord. This introduces a uniformly varying gravity force on the beam which increases its stiffness and hence its potential energy. Since this increase in potential energy is very small, its impact on higher modes is negligible. From FE analyses done, the increase in natural frequency for the first mode is approximately 0.3 Hz. Compared to the frequency resolution used in the tests, this increase does not seem substantial enough to be detectable. Even so, the effect due to other factors are more sensible and could mask any changes in modal properties due to the presence of the gravity force.
3. The test configuration used for all the three tests was intended to simulate free-free boundary conditions. Ideally the test configuration in which the structure is supported at its center of gravity, is the best one to use [32]. It allows for the desired rigid-body motions in the coordinates used in the testing. However, a knowledge of the location of center of gravity is not

known for practical structures. Further, suspending a practical structure suitably at its center of gravity may not be practical.

The test configuration used in the tests conducted do not allow for zero-frequency rigid-body motions. Using the analytical model developed in Chapter 3, the following rigid-body properties could be realized for the configuration used in TEST 2.

For the data, $m = 7832.3 \text{ kg/m}^3$, $L_1 = 1.3208\text{m}$, $L_2 = 1.5240\text{m}$ and $g = 9.81\text{m/sec}^2$, we have the following modal parameters,

$$f_1 = 0.3375 \text{ Hz} \quad \{\phi\}_1 = \begin{Bmatrix} 0.8837 \\ 1.0 \end{Bmatrix} \quad (6.12a)$$

$$f_2 = 1.2719 \text{ Hz} \quad \{\phi\}_2 = \begin{Bmatrix} -0.6529 \\ 1.0 \end{Bmatrix} \quad (6.12b)$$

Equations (6.12a and 6.12b) represent the two rigid-body modes of the the two-degree-of-freedom analytical model given by Eq. (3.40) in Chapter 3. Since the rigid-body modes occur at very low frequencies, curve-fitting them with in the presence of a lot of noise in the data can be a formidable task. If one works on the hypothesis that the rigid-body response contributes to the total response at frequencies around the first resonance, then, such a trend should be observable in the resulting mode vector. Using such an assumption, the mode vectors from FEA (transducer inertias included in the model) are plotted against the mode vector obtained from EMA, as shown in Fig. 6.15. Removing 7 of the poorer data points from the data and fitting the difference in modal displacements between EMA and FEA to a straight line, the following result is obtained

$$Y = 0.06756 - 0.001515 X \quad (6.13)$$

where, Y is the difference in modal displacements between EMA and FEA and X is the coordinate along the length of the beam. As can be seen in Fig. 6.15, there is a very systematic difference between the experimental and analytical mode vector which suggests the linear trend seen above in Eq. (6.13). Further, using the mobility form of the FRF equation²⁷, we could write

$$V_{jk}(\omega) = \sum_{r=1}^N \frac{i\omega\phi_{jr}\phi_{kr}}{\omega_r^2 - \omega^2 + i(2\zeta_r\omega_r\omega)} \quad (6.14)$$

If the modal properties of the rigid-body modes are known, then an estimate of its contribution to the response at the first resonance can be made.

4. In the tests conducted, the response signals were weighted with an exponential window. With the exception of TEST 2, in which the impulse signal was used, burst random excitation was used in all tests, and an exponential window was used to process the data. Since excitation and response signals have zero-frequency (DC) components in them, application of an exponential window would result in significant amount of leakage at the lower end of the spectrum, while performing a base-band analysis. This might be a plausible reason for the poor quality of the first mode.
5. Finally, the boundary conditions which exist in reality in the actual structure, which are obviously different from the ideal free-free conditions, can change the response (modal) characteristics at low frequencies. Hence, the systematic difference between the EMA and FEA results, observed in Fig. 6.15 and described by Eq. (6.13), could be due to the real boundary conditions in the test structure, as opposed to the ideal free-free conditions assumed in analytical modeling

²⁷ The curve-fitter uses the mobility form of FRF to extract modal parameters

Table 6.10. Results for the first mode from TEST 1,TEST 2 and TEST 3

Parameters	Test 1	Test 2	Test 3	
			Model 1	Model 2
MAC	0.9974	0.977	0.979	0.926
Natural Frequency	17.62 (0.06)	14.502 (0.152)	14.389 (0.010)	14.427 (0.038)
Damping Ratio	7.135 (1.007)	4.194 (1.953)	1.137 (0.074)	1.154 (0.321)
Frequency Resolution (Hz)	2.5	1.25	0.3125	0.3125

6.5 Summary of Results

Three modal tests were performed with a goal of identifying the contribution of the transduction and modal identification process to the inaccuracy of experimentally derived modal models. This was done by comparing results from three experimental modal test and analyses with those from corresponding finite element models. Comparisons were made for natural frequencies and mode shapes. Correlation between experimental and analytical natural frequencies was made using linear regression models. The modal assurance criterion (MAC) was used to establish the accuracy of the

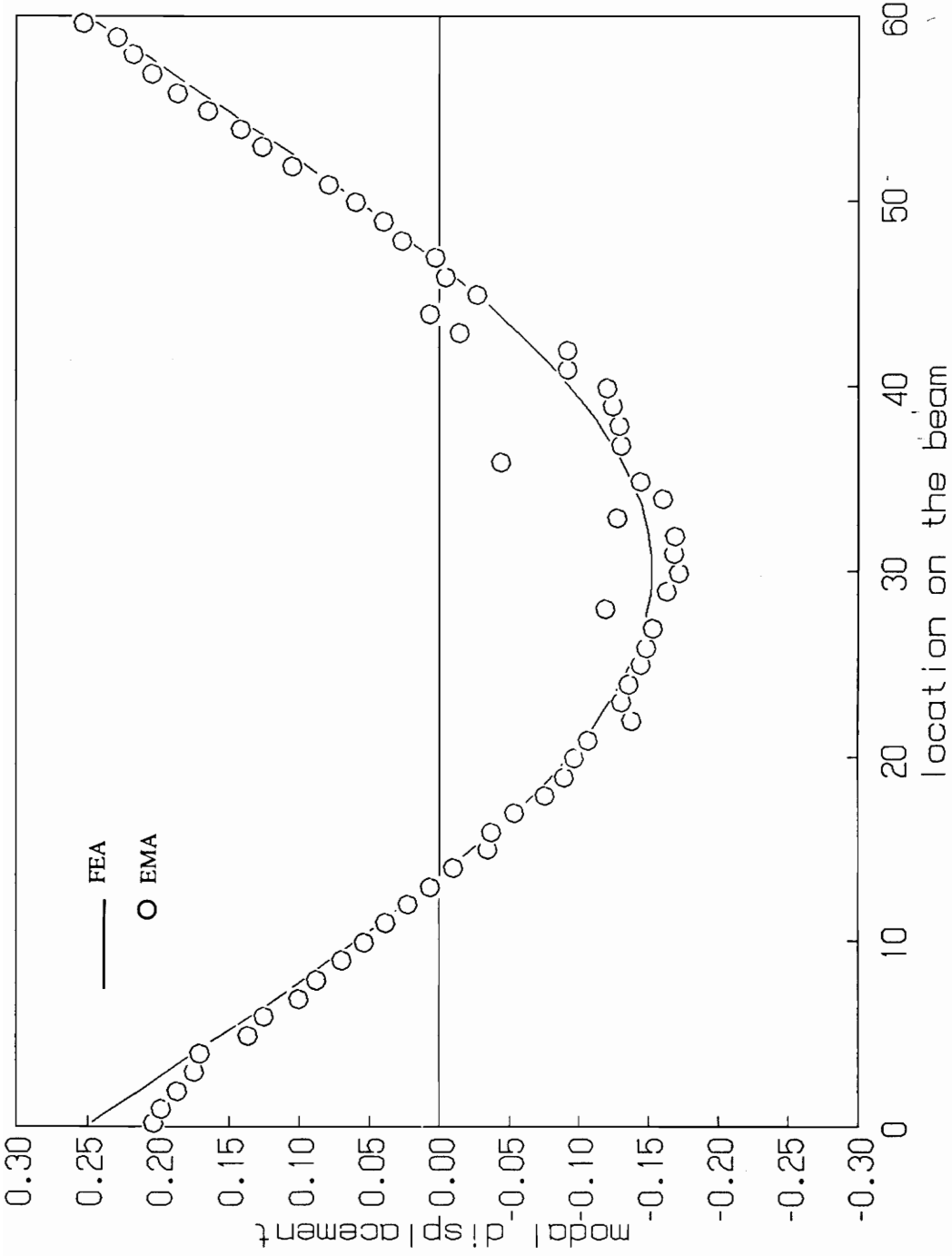


Figure 6.15 TEST 2 - Comparison of mode shape data from FEA and EMA for the first mode

mode vectors from EMA, with reference to those from FEA. The results obtained and the relevant discussions were presented in the earlier Sections. They are summarized below:

- Linear regression models were used to evaluate the degree of correlation between natural frequencies from EMA and FEA. This was done for both TEST 1 and TEST 2. The nature and extent of correlation obtained suggested that the EMA and FEA natural frequencies differed only by a scale factor. This was chiefly due to incorrect material property values used in the FE model.
- Inertia-loading of the structure due to roving accelerometer was a prominent feature of TEST 1. The variation of natural frequencies due to moving the accelerometer in the test was shown to have very good correlation with the variation predicted from FE analysis. With the exception of the first three modes, all modes showed correlation in excess of 95 %. Poor correlation observed for the lower modes was due to insufficient frequency resolution used in the FRF estimation. Further, the amount of variation in natural frequency for modes 5 through 10 were shown to be in good agreement with those predicted from the FE model, thereby explaining the high variances in estimating the natural frequencies. This claim was made based on the results from TEST 2, where the variances were much lower due to fixed (non-roving) transducer location.
- The errors in estimating natural frequencies were quantified, through various comparison methods, for both TEST 1 and TEST 2 results. Also, the errors were quantified on a location-by-location (spatial) basis. From this it was shown that the EMA natural frequencies were in substantial error only at locations near nodal points of modes. These errors were less than 2 to 3%.
- The quality of the mode vectors from the experimental modal models from TEST 1 and TEST 2 were excellent. This conclusion was made based on the MAC values obtained for EMA mode vectors, using the mode vectors from FEA as the reference. Typically, these were above

0.99 for both TEST 1 and TEST 2 results. These MAC values provided a quantitative statement of the overall error in the mode vectors from EMA. The EMA process was shown to be sensitive enough to detect changes in mode shapes due to the inertia-loading effect by transducers. This was demonstrated for mode vectors from both TEST 1 and TEST 2. The rotational mode vectors obtained from TEST 1, however, are poor. This was due to the poor quality of rotational measurements, as the coherence function estimates for rotational measurements demonstrate. The primary reason for poor coherence was low signal-to-noise ratios. In any case, the quality of the coherence function estimates, at the testing stage, did not suggest such poor rotational mode vectors. More importantly, this points to the deficiencies in qualifying the FRF data in a subjective manner, by qualitatively assessing the coherence function estimates.

- The first mode from the three tests, in particular from TEST 2 and TEST 3, had a relatively lower correlation, when compared to other lower modes of the structure. The reasons for very low MAC value seen for the first mode from Model 2 (TEST 3), were discussed earlier. Since the first mode occurred at a low frequency, it was affected by several factors which were cited and discussed elaborately. The effect of gravity on the first mode of the beam was studied in detail analytically, however, analytical predictions were not validated by experimental results. This was primarily due to the very small influence of the gravity force on the beam's first mode, in conjunction with insufficient frequency resolution used in the testing. Further, a host of other factors were identified, which collectively influenced the data obtained for the first mode, that could not be successfully delineated. The influence of the transducer inertias was one exception.
- As was done for natural frequencies, the error in estimating modal displacements were quantified spatially, i.e., on a location-by-location basis. This was done for mode vectors from both TEST 1 and TEST 2 results. The problem locations, again, were nodal points of modes. The errors were specified as a percentage difference between EMA modal displacements and the corresponding FEA modal displacements. These errors appeared to be random, and were

mostly within 5%, except at locations close to nodal points of modes. At locations close to nodes, the errors were substantially high, up to 200%. As was stated earlier, these errors were insignificant in that the modal displacements (at these locations) themselves were very very small.

- The impact of insufficient frequency resolution on the accuracy of the modal model was shown from the three tests. The modal properties of modes with low frequencies were the most vulnerable, as might be expected. The damping estimates in particular were highly susceptible to error due to insufficient frequency resolution. This was demonstrated through results from TEST 3, for the first three modes, by comparing them with TEST 2 results.
- It was shown, through results from TEST 3, that proper choice of test-configuration and exciter location is very vital to realizing an accurate modal model. Also, the influence of the test configuration and exciter location on the first mode was shown by plotting the results from EMA against those from FEA.
- The contribution of the parameter estimation procedure to the inaccuracy and inconsistency of the modal model was very negligible, compared to errors introduced into the experimental model by other processes used. This was clear from the statistical quality of the global modal parameters, in all the three tests. Furthermore, in cases where poor correlation was observed, for natural frequencies and mode vectors, and inaccurate damping estimates made, they were reconcilable as being due to factors other than parameter estimation.

Chapter 7

Conclusions

The goal of this thesis was to identify and quantify errors in modal models derived experimentally using FFT-based procedures. The interest was on errors incurred in estimating natural frequencies and mode shapes. Specifically, the contribution of the transduction (measurement) and modal identification process to the inaccuracy of the final modal model was the focus of the effort. Based on the results obtained, the following conclusions are drawn:

- The contribution of the transduction processes to the inaccuracy is very small. *Quality* transducers and *careful* measurements can hold this error to negligible levels.
- Given good quality FRF data - good signal-to-noise ratios, sufficient frequency resolution, etc., the errors that result from parameter estimation are statistically insignificant.
- Both natural frequency and residue estimates are very poor at locations close to nodal points of modes. All the four modal parameters are in substantial error at these locations. The natural frequency estimates were the poorest of all modal parameters, the error being around 2 to 3%.

- Poor signal-to-noise ratios and insufficient frequency resolution were the singular limiting factors, apparently, to the accuracy of experimentally derived modal models.
- The choice of test structure support has to be carefully made. An erroneous choice may imply wrong boundary conditions that may alter the final model substantially.
- Finally, in conclusion, a carefully planned and performed modal test that takes into account all the sources of error can yield very accurate models.

References

1. Cooley, J.W., and Tukey, J.W., "An Algorithm for Machine Calculation of Complex Fourier Series", *Mathematics of Computers*, 19(90), 1965, pp. 297-301.
2. Turner, M., Clough, R., Martin, H., and Topp, L., "Stiffness and Deflection Analysis of Complex Structures", *Journal of Aeronautical Sciences*, Vol. 23, 1956, pp. 805-823.
3. Argyris, J.H., and Kelsey, S., "*Energy Theorems and Structural Analysis*", Butterworth Scientific Publications, London, 1960.
4. Zienkiewicz, O. C. and Taylor, R.L., *The Finite Element Method*, McGraw Hill Book Company, 1989.
5. Ewins, D.J., and Griffin, J., "A State-of-the-Art Assessment of Mobility Measurement Techniques - Results for the Mid-Range Structures (30-3000Hz)", *Journal of Sound and Vibration*, 78(2), 1981, pp. 197-222.
6. Wicks, A.L., "The Quality of Modal Parameters from Measured Data", *Proceedings of Ninth IMAC*,²⁸ Florence, Italy, 1991, pp. 1623-1625.
7. Goyder, H.G.D., "Foolproof Methods for Frequency Response Measurements", *Proceedings of the Second International Conference on Recent Advances in Structural Dynamics*, Vol. 2, Eds. M. Petyt and H.F. Wolfe, held at Institute of Sound and Vibration Research, University of Southampton, Southampton, England, April 9-13, 1984, pp. 437-446.
8. Mitchell, L.D., Cobb, R.E., Deel, J.C., and Luk, Y.W., "An Unbiased Frequency Response Function Estimator", *Proceedings of Fifth IMAC, London, England*, 1987, pp. 364-373.
9. Bendat J. S., and Peirsol, A. G., *Random Data: Analysis and Measurement Procedures*, John Wiley and Sons, New York, 1986, 2 ed.
10. Han, M.C. and Wicks, A. L., "On the Application of Forsythe Orthogonal Polynomials for Global Modal Parameter Estimation", *Proceedings of Seventh IMAC*, Las Vegas, 1989, pp. 315-320.

²⁸ The acronym *IMAC* will be used in this References Section instead of *International Modal Analysis Conference*

11. Allemang, R.J., and Brown, D.L., "A Correlation Coefficient for Modal Vector Analysis", *Proceedings of the First IMAC*, Orlando, Florida, 1982, pp. 110-115.
12. Stein, P.K., "Experimental Error ? No Experimenter's Error ! A Measurement Engineer's View of Experimental Modal Analysis", *Proceedings of Third IMAC*, Orlando, Florida, 1985, pp. 824-830.
13. Hopton, G.W., and Deblauwe, F., "Relationship between Analysis Errors and Complex Mode Shapes", *Proceedings of Fifth IMAC*, London, England, 1987, pp. 381-388.
14. Dossing, O., "Prediction of Transducer Mass-Loading Effects and Identification of Dynamic Mass", *Proceedings of Ninth IMAC*, Florence, Italy, 1991, pp. 306-312.
15. McConnell, K.G., "Errors in using Force Transducers", *Proceedings of Eighth IMAC*, Kissimmee, Florida, 1990, pp. 884-890.
16. Walter, P.L., "Considerations in Accelerometer Application to Modal Analysis", *Proceedings of Eighth IMAC*, Kissimmee, Florida, 1990, pp. 900-904.
17. Han, S., and McConnell, K.G., "The Effects of Transducer Cross-Axis Sensitivity in Modal Analysis", *Proceedings of Seventh IMAC*, Las Vegas, Nevada, 1989, pp. 505-511.
18. McConnell, K.G., and Han, S.B., "A Theoretical Basis for Cross-Axis Corrections in Tri-Axial Accelerometers", *Proceedings of Seventh IMAC*, Las Vegas, 1989, pp. 171-175.
19. Brown, D.L., Carbon, G., Ramsey, K., "A Survey of Excitation Techniques Applicable to the Testing of Automotive Structures", *SAE Paper No. 770029*, 1977.
20. Olsen, N.L., "Burst Random Excitation", *Sound and Vibration*, November 1983, pp. 20-23.
21. Olsen, N.L., "Excitation Functions for Structural Frequency Response Measurements", *Proceedings of the Second IMAC*, Orlando, Florida, 1986 pp. 894-902.
22. Rao, D.K., "Electrodynamic Interaction between a Resonating Structure and an Exciter", *Proceedings of the Fifth IMAC*, London, England, 1987 pp. 1142-1150.
23. Olsen, N.L., "Using and Understanding Electrodynamic Shakers in Modal Applications", *Proceedings of Fourth IMAC*, Los Angeles, California, 1986, pp. 1160-1167.
24. Peterson, E.L., and Mouch, T.A., "Modal Excitation: Force Drop-Off at Resonances", *Proceedings of Eighth IMAC*, Kissimmee, Florida, 1990 pp. 1226-1231.
25. Peterson, E.L., "Modal Excitation: A Comparison of Three Different Methods", *Proceedings of Sixth IMAC*, Kissimmee, Florida, 1988, pp. 1397-1402.
26. Corelli, D., and Brown, D.L., "Impact Testing Considerations", *Proceedings of Second IMAC*, Orlando, Florida, 1984, pp. 735-742.
27. Sohaney, R.C., and Nieters, J.M., "Proper Use of Weighting Functions for Impact Testing of a Structure", *Proceedings of Third IMAC*, Orlando, Florida, 1984, pp. 160-165.
28. Harris, F.J., "On the Use of Windows for Harmonic Analysis with the Discrete Fourier Transform", *Proceedings of the IEEE*, Vol. 66, No. 1, 1978, pp. 51-83.
29. Soucy, Y., and Deering, D.W., "Effect of Data Acquisition Conditions on Modal Testing of a Simple Structure", *Proceedings of Sixth IMAC*, Kissimmee, Florida, 1988, pp. 8-13.
30. Wang, I.C., Wei, M.L., and Wei, J.C., "Comparisons of Finite Element Method and Experimental Modal Analysis of a T-Plate with Various Boundary Conditions", *Proceedings of Fourth IMAC*, Los Angeles, California, 1986, pp. 748-753.

31. Lamontia, M.A., "On the Determination and Use of Residual Flexibilities, Inertia Restraints, and Rigid-Body Modes", *Proceedings of the First IMAC*, Orlando, Florida, 1982, pp. 153-159.
32. Okubo, N., and Furukawa, T., "Measurement of Rigid Body Modes for Dynamic Design", *Proceedings of Second IMAC*, Orlando, Florida, 1984, pp. 545-549.
33. Mitchell, L.D., "An Improved Method for the Fast Fourier Transform (FFT) Calculation of the Frequency Response Function", *Proceedings of the First European Signal Processing Conference EUSIPCO-80 - Short Communication and Poster Digest*, Swiss Federal Institute of Technology, Lausanne, Switzerland, September 1980, pp. 159-160.
34. Mitchell, L.D., "Improved Methods for the Fast Fourier Transform (FFT) Calculation of the Frequency Response Function", *Transactions of the ASME, Journal of Mechanical Design, Vol. 104*, April 1982, pp. 277-279.
35. Cawley, P., "The Reduction Bias Error in Transfer Function Estimates using FFT-Based Analyzers", *The Ninth Biennial Conference on Mechanical Vibration and Noise of the Design and Production Engineering Technical Conferences*, Dearborn, Michigan, September 1983, pp. 45-53.
36. Rocklin, G.T., Crowley, J., Vold, H., "A Comparison of H_1 , H_2 and H , Frequency Response Functions", *Proceedings of the Third IMAC*, Orlando, Florida, 1985, pp.272-278.
37. Wicks, A.L., and Han, M.C., "The Influence of Frequency Response Function Estimation Method on Modal Parameter Estimators", *Proceedings of Seventh IMAC*, Las Vegas, Nevada, 1989, pp. 817-821.
38. Wicks, A.L., "Estimation of Frequency Response Function in the presence of uncorrelated content", *PhD Dissertation*, 1986, Michigan Technological University, Houghton, Michigan.
39. Wicks, A.L., and Vold, H., "The H , Frequency Response Function Estimator", *Proceedings of Fourth IMAC*, Los Angeles, California, 1986, pp. 897-899.
40. Smiley, R.G., Patrick, G.B., Sohaney, R.C., "Automated Methods of Frequency Response Function Quality Evaluation", *Proceedings of Fourth IMAC*, Los Angeles, California, 1986, pp. 107-112.
41. Cobb, R.E., "Confidence Bands, Measurement Noise, and Multiple Input-Multiple Output Measurements Using the Three-Channel Frequency Response Function Estimator", *PhD Dissertation*, 1988, Virginia Polytechnic Institute and State University, Blacksburg, Virginia.
42. Kirshenboim, J. and Ewins, D.J., "A Method for Recognizing Structural Nonlinearities in Steady-State Harmonic Testing", *The Ninth Biennial Conference on Mechanical Vibration and Noise of the Design and Production Engineering Technical Conferences*, Dearborn, Michigan, September 1983, pp. 39-43.
43. He, J., and Ewins, D.J., "A Simple Method of Interpretation for the Modal Analysis of Non-linear Systems", *Proceedings of Fifth IMAC*, London, England, 1987, pp. 626-634.
44. Zavodney, L.D., "Can the Modal Analyst Afford to be Ignorant of Nonlinear Vibration Phenomenon", *Proceedings of Fifth IMAC*, London, England, 1987, pp. 154-159.
45. Ibrahim, S.R., "Modal Identification Techniques Assessment and Comparison", *Proceedings of Eighth IMAC*, Kissimmee, Florida, 1990, pp. 831-839.
46. Richardson, M.H., Potter, R., "Identification of the Modal Properties of an Elastic Structure from Measured Transfer Function Data", *Instrument Society of America ASI 74250*, 1974, pp. 239-246.

47. Brown, D.L., Allemang, R.J., Zimmerman, R., and Mergeay, M., "Parameter Estimation Techniques for Modal Analysis", *SAE Paper No. 790221*, 1979.
48. Richardson, M.H., Formenti, D.L., "Parameter Estimation from Frequency Response Measurements using Rational Fraction Polynomials", *Proceedings of the First IMAC*, Orlando, Florida, 1982, pp. 167-181.
49. Richardson, M.H., Formenti, D.L., "Global Curve-Fitting of Frequency Response Measurements using the Rational Fraction Polynomial Method", *Proceedings of the First IMAC*, Orlando, Florida, 1982, pp. 390-397.
50. Turunen, R., "Statistical Performance of Modal Parameter Estimation Methods", *Proceedings of Fifth IMAC*, London, England, 1987, pp. 26-36.
51. Lee, M., and Richardson, M., "Determining the Accuracy of Modal Parameter Estimation Methods", *Proceedings of Tenth IMAC*, San Diego, California, 1992, pp. 159-166.
52. Leuridan, J., "Modal Analysis: A Perspective on Integration", *Proceedings of Ninth IMAC*, Florence, Italy, 1991, Keynote Address.
53. Reddy, J.N., "Class Notes/Home Work Assignments", *ESM 6734 - Finite Element Analysis*, Spring 1989, Virginia Polytechnic Institute and State University, Blacksburg, Virginia
54. Meirovitch L., *Analytical Methods in Vibration*, Macmillan Company, 1967.
55. Ewins, D. J., *Modal Testing: Theory and Practice*, Research Studies Press, Letchworth, Hertfordshire, England, 1986.
56. Pakstys, M.P., "Correlation of Experimental and Analytical Structural Dynamic Parameters, A 1982 Overview", *Proceedings of Eighth IMAC*, Kissimme, Florida, 1982, pp. 315-320.
57. Ibrahim, S. R., and Saafan A. A., "Correlation of Analysis and Test in Modeling of Structures, Assessment and Review", *Proceedings of Eighth IMAC*, London, England, 1987, pp. 1651-1660.
58. Guyan, R.J., "Reduction of Stiffness and Mass Matrices", *AIAA Journal*, Vol 3., No.2, 1965, pp. 380.
59. Reddy, J. N., *An Introduction to the Finite Element Method*, McGraw Hill Book Company, 1984.
60. Meirovitch L., *Elements of Vibration Analysis*, McGraw Hill Book Company, 1986, 2nd ed.
61. Taber, R. C., Vold, H., Brown, D. C., and Rocklin, G. T., "Exponential Window for Burst Random Excitation", *Proceedings of Third IMAC*, Kissimme, Florida, 1985, pp. 989-995.
62. Rorrer, R.A.L., Wicks, A.L., Williams, J., "Angular Acceleration Measurements of a Free-Free Beam", *Proceedings of the Seventh IMAC*, Las Vegas, Nevada, 1989, pp. 1300-1304.

Appendix A. Nomenclature

Latin Symbols

u_1, u_2, u_3	displacements in the coordinate directions x, y, z
$w(x, t)$	transverse displacement of the beam
$\frac{\partial w}{\partial x}$	slope due to bending deformation of the beam
E	Young's modulus
G	Shear modulus
L	length of the beam
r	radius of gyration of the transverse cross-section of the beam, about the neutral axis
I	moment of inertia about the neutral axis of the beam
A	transverse cross-sectional area of the beam
$P(x, t)$	distributed axial load acting on the beam
$V(x, t)$	net shear force at any transverse cross-section of the beam
$p(x, t)$	distributed axial load per unit length of the beam
$f(x, t)$	distributed transverse load acting on the beam
K	shear correction factor
L_e	length of a finite element

$v(x), v_1(x), v_2(x)$	test functions used in the variational statements of the governing equations of motion
$[K]$	stiffness matrix
$[M]$	mass matrix
$[C]$	damping matrix
det	determinant of a square matrix
<i>Diag</i>	diagonal matrix
$[I]$	unit matrix
m	mass element of a single-degree-of-freedom system
c	viscous-damping element of a single-degree-of-freedom system
k	stiffness element of a single-degree-of-freedom system
$h(t)$	impulse response function (IRF) of a single-degree-of-freedom system
f	cyclic frequency in Hertz (Hz)
$H(\omega)$	frequency response function (FRF) of a single-degree-of-freedom system
H_1, H_2	univariate FRF estimators
H_3, H_v, H_s, H^c	bivariate FRF estimators
$V(\omega)$	mobility form of frequency response function (FRF)
$A(\omega)$	accelerance or inertance form of frequency response function (FRF)
x_j	displacement at location j of a multiple-degree-of-freedom system
f_k	forcing at location k of a multiple-degree-of-freedom system
$H_{jk}(\omega)$	FRF of a multiple-degree-of-freedom system, for forcing at k and response at j
$[H(\omega)]$	FRF matrix for a multiple-degree-of-freedom system
A'_{jk}	residue or modal constant in the FRF expression
$E_{jk}(\omega_i)$	experimentally obtained FRF at discrete frequencies i , for forcing at k and response at j
Y_{jk}	Inertia restraint for forcing at k and response at j
Z_{jk}	Residual flexibility for forcing at k and response at j

$R_{ff}(\tau)$	auto-correlation function of the time record $f(t)$
$R_{xf}(\tau)$	cross-correlation function between the time records $x(t)$ and $f(t)$
$S_{ff}(\omega)$	two-sided autospectral (powerspectral) density function of the record $f(t)$
$G_{ff}(\omega)$	one-sided autospectral (powerspectral) density function of the record $f(t)$
$S_{xf}(\omega)$	two-sided cross-spectral density function between the records $x(t)$ and $f(t)$
$G_{xf}(\omega)$	one-sided cross-spectral density function between the records $x(t)$ and $f(t)$
$m(t)$	noise in the input measurement of a single input/single output linear system model
$n(t)$	noise in the output measurement of a single input/single output linear system model

Greek Symbols

$\theta(x,t)$	slope of a deformed beam in the Euler-Bernoulli theory
$\psi(x,t)$	true slope of a deformed beam in the Timoshenko beam theory
$\kappa(x,t)$	slope due to shearing deformation in the Timoshenko beam theory
ε_{ij}	Green's strain components
σ_{ij}	stress components
ρ	mass density of the material of the beam
ω	circular frequency in radians per second
ω_r	natural frequency of the r th mode in radians per second
ω_{rd}	damped natural frequency of the r th mode in radians per second
Δf	frequency resolution (spacing between discrete spectral lines)
ζ_r	damping ratio of the r th mode (viscous damping)
γ_r	damping ratio of the r th mode (structural damping)
Ω_e	domain of a finite element
ϕ_i, ϕ_j	interpolation functions (ϕ Hermite)

ψ_i, ψ_j	interpolation functions (Lagrange)
Λ_r	eigenvalue of the r th mode
$\{\phi\}_r$	eigenvector of the r th mode (complex in general)
$\{\phi\}_r^*$	complex conjugate of the eigenvector of the r th mode
$[\Phi]$	mass-normalized modal matrix for proportionally damped systems
$[\Psi]$	modal matrix for non-proportionally damped systems
$\gamma_{yx}^2(\omega)$	coherence function between the input $x(t)$ and output $f(t)$

Vita

Kannan Marudachalam was born in Coimbatore in the state of Tamilnadu, India, on January 26th 1963. He obtained his entire school education from Stanes high school, Coimbatore. He then enrolled at the Coimbatore Institute of Technology, University of Madras, and earned a bachelors degree in mechanical engineering in 1986. After graduation he worked for a period of one year as an assistant lecturer of mechanical engineering at the Tamilnadu College of Engineering, Bharathiar University, Coimbatore. Deciding to pursue advanced degrees, the author enrolled in the graduate program in mechanical engineering at Virginia Polytechnic Institute and State University in fall 1988.

A handwritten signature in black ink, appearing to read "Kannan", is written above a horizontal line.